High-resolution deformation measurement using Persistent Scatterer Interferometry

Núria Devanthéry Arasa

Advisor:

Dr. Michele Crosetto
Dep. de Teledetecció – Divisió de Geomàtica
Centre Tecnològic de Telecomunicacions de Catalunya (CTTC)

Tutor:

Prof. Josep Gili Ripoll
Dep. d'Enginyeria del Terreny
Universitat Politècnica de Catalunya

PhD. Dissertation
Title: High-resolution deformation measurement using Persistent Scatterer Interferometry
Author: Núria Devanthéry Arasa
Advisor: Dr. Michele Crosetto
Tutor: Prof. Josep Gili Ripoll
Centre: Centre Tecnològic de Telecomunicacions de Catalunya (CTTC)
PhD program: Aerospace Science and Technology - UPC
Castelldefels, 15th September 2014

Abstract

Persistent Scatterer Interferometry (PSI) is a group of advanced differential interferometric SAR techniques that are used to measure and monitor terrain deformation. Different PSI techniques have been proposed in the last two decades. In this thesis, the two PSI chains implemented and used at the Geomatics division of CTTC are described: the local area PSI and the PSIG chains.

The first part of the thesis is devoted to the local area PSI chain, used to analyse the deformations over small areas. The chain includes a linear deformation model to directly deal with interferometric wrapped phases. Moreover, it does not directly involve the estimation of the APS, thus simplifying the procedure and its computational cost. The chain has been tested using different types of SAR data. The availability of high resolution X-band SAR data has led to an improvement of the PSI results with respect to C-band data. The higher image resolution and phase quality implies an increase of the PS density, an improvement in the estimation precision of the residual topographic error and a higher sensibility to very small deformations, including the displacements caused by thermal dilation. An extension of the classical PSI linear deformation model has been proposed, to account for the thermal dilation effects. This allows obtaining a new PSI outcome, the thermal dilation parameter, which opens new interesting applications since it provides information on the physical properties of single objects, i.e. the coefficient of thermal expansion, and the static structures of the same objects.

The second part of the thesis describes the PSIG chain, whose aim was to extend the interferometric processing to wider areas. The ability to cover wide areas is essential to obtain a unique and consistent deformation monitoring for the available SAR image full scenes, i.e. typically 30 by 50 km for TerraSAR-X, 40 by 40 km for CosmoSkyMed and 100 by 100 km for ASAR-ENVISAT and ERS. This is particularly important for the forthcoming C-band Sentinel SAR data that will cover 250 by 250 km with a single image scene. The key steps of the PSIG procedure include a new selection of candidate PSs based on a phase similitude criteria and a 2+1D phase unwrapping algorithm. The procedure offers different tools to control the quality of the processing steps. It has been successfully tested over urban, rural and vegetated areas using X-band PSI data. The performance of the PSIG chain is illustrated and discussed in detail, analysing the procedure step by step.

Keywords: Persistent Scatterer Interferometry; phase unwrapping; deformation measurement; high-resolution SAR.

Resum

Persistent Scatterer Interferometry (PSI) és un grup de tècniques avançades d'interferometria diferencial SAR que s'utilitzen per mesurar i monitoritzar deformacions del terreny. Durant les últimes dues dècades s'han proposat diverses tècniques PSI. En aquesta tesi es descriuen les dues cadenes PSI implementades i utilitzades en la divisió de Geomàtica del CTTC: la cadena PSI d'àrea local i la cadena PSIG.

La primera part de la tesi està dedicada a la cadena PSI d'àrea local, que s'utilitza per analitzar deformacions en zones d'extensió limitada. La cadena inclou un model de deformació lineal per tractar directament amb les fases interferomètriques *wrapped*. En canvi, no estima directament la component atmosfèrica, cosa que simplifica el procediment i el seu cost computacional. La cadena s'ha provat sobre diferents tipus de dades SAR. La disponibilitat de dades SAR d'alta resolució en banda X ha donat lloc a una millora dels resultats del PSI respecte a les dades en banda C. La resolució més gran de la imatge i la qualitat de la fase impliquen un augment de la densitat de PS, una millora en la precisió de l'estimació de l'error topogràfic residual i una sensibilitat més alta a deformacions subtils, incloent-hi els desplaçaments causats per la dilatació tèrmica. Per tenir en compte els efectes de la dilatació tèrmica, s'ha proposat una extensió del model PSI clàssic que ens permet obtenir un nou producte PSI: el paràmetre de dilatació tèrmica. Aquest paràmetre obre noves aplicacions interessants: proporciona informació relacionada amb les propietats físiques dels objectes mesurats –com el coeficient d'expansió tèrmica– i amb la seva pròpia estructura estàtica.

La segona part de la tesi descriu la cadena PSIG, l'objectiu de la qual és estendre el processament interferomètric a àrees més extenses. La capacitat de cobrir àrees grans és fonamental per obtenir un únic mapa global de deformacions que sigui consistent i cobreixi l'extensió sencera de les imatges SAR disponibles, de 30 km per 50 km per TerraSAR-X, de 40 km per 40 km per CosmoSkyMed i de 100 km per 100 km per ASAR-ENVISAT i ERS. Això és particularment important tenint en compte la propera disponibilitat de les dades del satèl·lit Sentinel, que opera en banda C i cobrirà 250 km per 250 km amb una sola imatge. Els passos clau del procediment PSIG són una nova selecció de PS candidats en base a un criteri de similitud de fase i un algoritme de 2+1D *phase unwrapping*. El procediment ofereix diferents eines per controlar la qualitat dels diferents passos del processament. La cadena PSIG s'ha utilitzat amb èxit en àrees urbanes, rurals i amb vegetació utilitzant dades PSI en banda X. El funcionament de la cadena PSIG s'il·lustra i es descriu en detall, analitzant el procediment pas a pas.

Paraules clau: *Persistent Scatterer Interferometry*; *phase unwrapping*; mesura de deformacions; SAR d'alta resolució.

Acknowledgments

This thesis is the result of the work carried out during the last four years at the Active Remote Sensing Unit (TA) of the Institute of Geomatics, now Remote Sensing department of the Geomatics division of CTTC. During these years, many people has contributed, in different ways, to the development of this work.

First of all, I would like to thank my advisor, Dr. Michele Crosetto, for giving me the opportunity to carry out this work. The work presented in this thesis would have not been possible without his constant support and guidance. I am grateful to him for having introduced me to the field of Synthetic Aperture Radar. I have learned a lot working with him during these years.

I would also like to thank my colleagues of the Geomatics division of CTTC for all the professional support and the moments shared together. I would like to especially express my gratitude to the Remote Sensing team for the invaluable professional help and interesting discussions during these years. In particular, I would like to thank Dr. Oriol Monserrat for his fundamental contributions, research discussions and for being always available to answer all my questions, María Cuevas for her useful comments, reviews and valuable contributions, Dr. Guido Luzi for the valuable and interesting discussions and advices on radar and microwaves, and Marta Agudo for her comments and help. I am also grateful to Prof. Bruno Crippa for his help with different software tools and for his useful advices. I also would like to thank the tutor of my thesis, Prof. Josep Gili, for his help.

Finally, I am indebted to my family and friends for their unconditional support. In particular, I would like to thank my mother and my brother.

Content

Chapter 1

Introduction

Persistent Scatterer Interferometry (PSI) is a group of powerful techniques for deformation measurement and monitoring using interferometric Synthetic Aperture Radar (SAR) imagery. PSI represents an advanced type of Differential Interferometric SAR (DInSAR) techniques: it is based on large stacks of SAR images and suitable data modelling procedures that enable the estimation of different parameters. These parameters include the deformation time series, the average displacement rates and the so-called residual topographic error (RTE), which is the difference between the heights of the scattering phase centre of a given point with respect to the Digital Elevation Model (DEM) used in the PSI processing. This latter parameter plays an important role for both PSI modelling and geocoding.

This thesis has been carried out at the Active Remote Sensing Unit of the Institute of Geomatics (IG), now the Remote Sensing Department of the Geomatics Division of the CTTC. The starting point of this work was a complete Persistent Scatterer Interferometry chain that had been successfully tested with C-band and X-band SAR data (Crosetto et al., 2010). However, most of the results derived with this processing chain concerned urban areas and the chain was mainly used to perform deformation studies at local scale (Biescas et al. 2007, Crosetto et al. 2010).

The first part of my work has been devoted to the analysis of X-band data using the PSI chain available at the IG. The X-band PSI data, which are characterized by high phase quality and a shorter wavelength, are sensitive to the thermal expansion of the imaged objects (Crosetto et al. 2010). Therefore, an extension of the local PSI chain was performed, which allowed obtaining a new PSI product called the thermal dilation maps (Monserrat et al., 2011).

The second, and more important, part of my work was focused on developing an extension of the existing PSI interferometric chain able to process wide areas while maintaining PS density in urban areas and obtaining a sufficient density in rural areas. This extension yielded a new PSI chain named PSIG: the PSI chain of the Geomatics Division of CTTC. The PSIG chain has been recently described in Devanthéry et al. (2014). The ability to process wide areas is fundamental to obtain a unique and consistent deformation monitoring of the available full scene SAR images, i.e. typically 30 by 50 km for TerraSAR-X, 40 by 40 km for CosmoSkyMed and 100 by 100 km for ASAR-ENVISAT and ERS. This is particularly important for the forthcoming C-band Sentinel SAR data that will cover 250 by 250 km in a single image scene. An entire chapter of this work is devoted to the description of the PSIG chain. Its key steps are a selection of PS candidates based on a phase similitude criteria and a 2+1D phase unwrapping algorithm. In addition to the deformation velocity map and the PS Time Series (TSs), a quality index for each TS and other parameters related to the detection and correction of unwrapping errors are produced. The PSIG chain has been successfully tested over urban and rural areas using different TerraSAR-X and CosmoSkyMed datasets.

This dissertation is organized in four main chapters, plus the introduction (Chapter 1) and the conclusions (Chapter 6). Chapter 2 is devoted to the basic principles of SAR interferometry and

DInSAR. A review of the main PSI techniques related to this work is provided in this chapter. Chapter 3 describes the local PSI chain developed and used at the former IG, now the Geomatics Division of the CTTC. The key steps of the procedure are presented and some results of velocity of deformation and residual topographic error maps are discussed. The second part of the chapter is devoted to the thermal dilation effects detectable using high-resolution X-band data. Chapter 4 describes the entire PSIG chain, which consists of three main blocks. The first block is the selection of the so-called candidate Cousin Persistent Scatterers (CPSs) that have to be homogeneously distributed over the area of interest. In the second block, the atmospheric component is removed from the unwrapped interferograms using a set of spatial and temporal filters. In the third block, the final deformation measurements are estimated together with a set of quality parameters. In Chapter 5, the results of the PSIG analysis are thoroughly presented, exploring in particular a dataset of 28 StripMap TerraSAR-X images that cover the metropolitan area of Barcelona (Spain).

Chapter 2

Differential SAR interferometry and Persistent Scatterer Interferometry

Differential SAR interferometry is a remote sensing technique used to measure and monitor terrain deformations. It consists in the comparison of the interferometric phase of two SAR radar images acquired over the same area on different dates. This technique has been successfully used to monitor different types of deformation phenomena, e.g. see Gabriel et al. (1989). However, this technique exhibits important limitations caused by the atmospheric effects and the noise components caused by temporal and geometrical decorrelation. Many Persistent Scatterer Interferometry (PSI) techniques, mainly based on stacks of interferograms, have been proposed during the last fifteen years to overcome these limitations.

This chapter presents an overview of the main DInSAR measurement principles and characteristics and a review of the principal PSI techniques. Section 2.1 provides an outline of the main SAR image acquisition basics and characteristics with the purpose of recalling the fundamentals of SAR interferometry. Section 2.2 addresses the interferometric SAR principles, as well as the main characteristics of DInSAR. Section 2.3 is devoted to the fundamentals of PSI and contains an overview of the main existing PSI techniques.

2.1. SAR images

Synthetic Aperture Radar (SAR) is an active, side looking sensor, usually mounted on a satellite or plane, which emits pulses in the microwave portion of the electromagnetic spectrum and detects the reflections of these pulses from objects in its Line of Sight (LOS) (Hanssen, 2001). It has the capability to measure day and night and in all weather conditions due to the microwave property to penetrate clouds, rain, etc. SAR is a coherent system in that it retains both the phase and the amplitude of the backscattered signal (Curlander and McDonough, 1991). Thus, the information contained in the SAR images is twofold: the backscattered intensity provides information about the physical properties of the objects, and the phase contains information about the range of the objects.

2.1.1. SAR image acquisition

The SAR images are usually acquired on board an airplane or a satellite. Let's consider a spaceborne sensor that travels at the velocity of a satellite at constant altitude in a straight line, i.e. the azimuth direction, and emits the electromagnetic beam perpendicular to the azimuth direction, i.e. the range direction (see Figure 2.1). The illuminated area on the ground is the antenna footprint. Figure 2.1 illustrates the most common SAR imaging geometry, the StripMap mode, which is the acquisition mode of the SAR images used in this thesis. The StripMap mode scans the ground track with constant incident angle θ. The range resolution ΔRange depends on

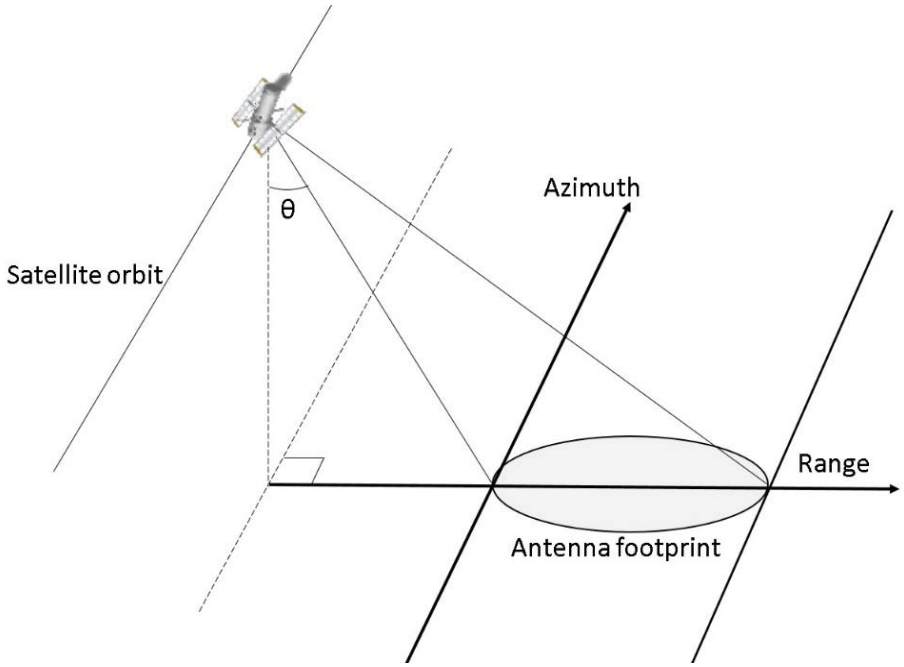

Figure 2.1. StripMap SAR imaging geometry.

the pulse duration τ, which must be short enough to allow a good resolution, but large enough to ensure a sufficient backscattered energy. The azimuth resolution ΔAzimuth is inversely proportional to the antenna dimension in the azimuth direction and to the operational wavelength: the shorter the wavelength and the larger the antenna dimension, L_a, the better the resolution. However, the antenna dimension has restrictions in terms of size. Therefore, a synthetic antenna is created exploiting the movement of the antenna: starting from a short physical antenna this allows obtaining a much larger synthetic antenna. In order to obtain the final SAR images, a post-processing of the raw data acquired by the SAR is required. This process is the SAR focusing. Numerous SAR focusing algorithms are described in the literature, e.g. see Ulaby et al. (1986). The final maximum range and azimuth resolutions are given by:

$$\Delta\text{Range}=\frac{c}{2B_P} \qquad (2.1)$$

$$\Delta\text{Azimuth}=\frac{L_a}{2}$$

where c is the velocity of the light, B_P is the pulse bandwidth and L_a is the synthetic antenna dimension.

2.1.2. Single Look Complex SAR image

The result of the SAR raw image focusing step is a two dimensional complex image, the single look complex (SLC) image, whose rows and columns are directly related to the azimuth and range positions of the scatterers. Each pixel contains the in-phase (I) and quadrature (Q) components of the radar signal, from which the amplitude (A) and the phase (ϕ) are derived:

$$A=\sqrt{I^2+Q^2} \qquad (2.2)$$

$$\phi=\arctan\left(\frac{Q}{I}\right)$$

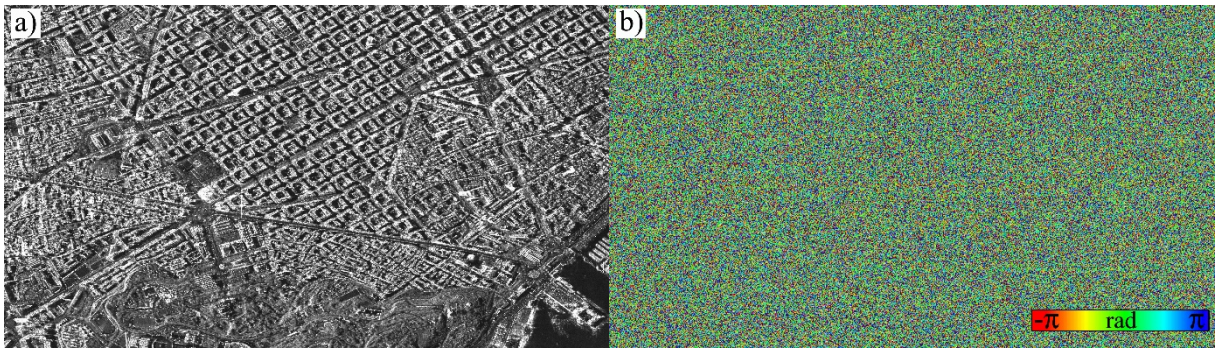

Figure 2.2. Mean amplitude image of 18 Single Look Complex (SLC) images over Barcelona (a). White pixels correspond to high reflectivity areas, for instance corners of buildings, whereas dark pixels correspond to low reflectivity points, as the sea (see the bottom right corner). Phase image of a SLC over the same area (b). The phase ranges from $-\pi$ to π.

The amplitude (Figure 2.2a) is the measure of the power backscattered from the illuminated targets and depends mainly on the roughness of the terrain. However, the backscattering characteristics also depend on other surface properties such as the dielectric constant and the local slope. A detailed analysis of the surface scattering models can be found in Elachi (1988). The wavelength of the sensor also influences the electromagnetic interaction with the terrain. Longer wavelengths penetrate deeper in the soil surface than shorter ones, but they provide a rougher resolution. By contrast, the phase (Figure 2.2b) mainly depends on the distance from the sensor to the ground. In fact, the phase is the measure of the travel distance (going and coming back, i.e. 2R) covered by the signal. The relation between phase and distance is:

$$\phi=\frac{2\pi}{\lambda}2R+\phi_0=\frac{4\pi}{\lambda}R+\phi_0 \qquad (2.3)$$

where ϕ_0 is the phase shift generated during the interaction between the microwaves and the measured object, and λ is the wavelength of the sensor.

It is important to note that the radar only measures fractions of the whole phase. This aspect, named phase ambiguity, is treated later in this chapter.

2.1.3. Geometric distortions of SAR images

Since the radar is a ranging system, terrain elevation results in geometric distortions in the SAR images (Hanssen, 2001). This affects the ground resolution cell, i.e. the SAR resolution cell projected on the ground. Figure 2.3 illustrates the three distortion effects that can be found in the SAR images: foreshortening, layover and shadow. Foreshortening appears in the slopes that are facing the radar sensor: the measured terrain is compressed, i.e. it appears shorter in the SAR image (see points A-B in Figure 2.3). On the other hand, the opposite effect occurs for the slopes that are bent away from the sensor: the terrain is expanded in the SAR image. Layover occurs in slopes that are higher than the incidence angle, i.e. the sensor firstly receives the signal reflected by the top and then the signal coming from the bottom of the slope (see points C-D in Figure 2.3). Finally, shadow occurs when an object of the ground prevents the radar signal to reach other ground scatterers (see points D-E in Figure 2.3). It occurs in steep slopes opposite to the sensor. No measurements are possible on those areas.

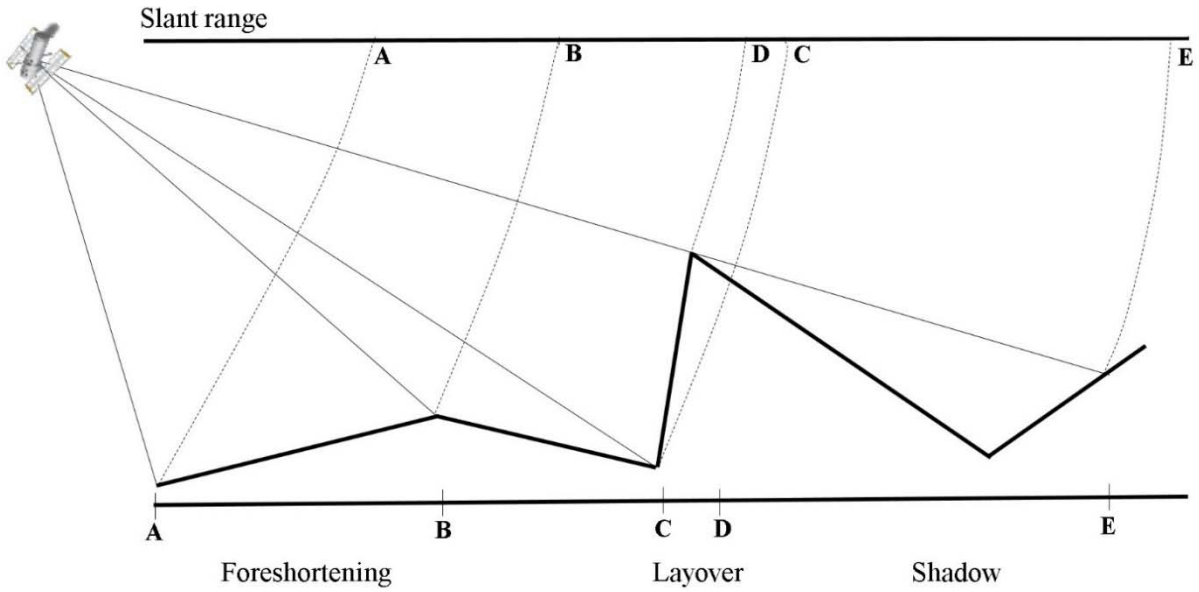

Figure 2.3. Foreshortening, layover and shadow effects. Scatterers between A-B suffer foreshortening effects, points C-D are reverted due to the layover, and scatterers between D-E are not illuminated by the radar due to the shadow effect.

2.1.4. Scatterers per resolution cell

Each pixel corresponds to just one signal, which is the vectorial sum of the multiple signals of the scatterers contained within the ground resolution cell. Figure 2.4 illustrates the scattering mechanism in a resolution cell, where the returned signal is the coherent sum of the backscattered signal from the scattering elements. If the backscattered signal of a single target is much stronger than the others, it will dominate almost completely the received radar phase signal. This is known as point scattering. By contrast, distributed scattering happens when a large number of similar scatterers contribute to the reflected signal. The scattering is classified as either coherent or incoherent, depending on how the targets behave in time. Coherent scattering occurs when the different targets behave similarly in time, while incoherent scattering occurs when they behave randomly in time.

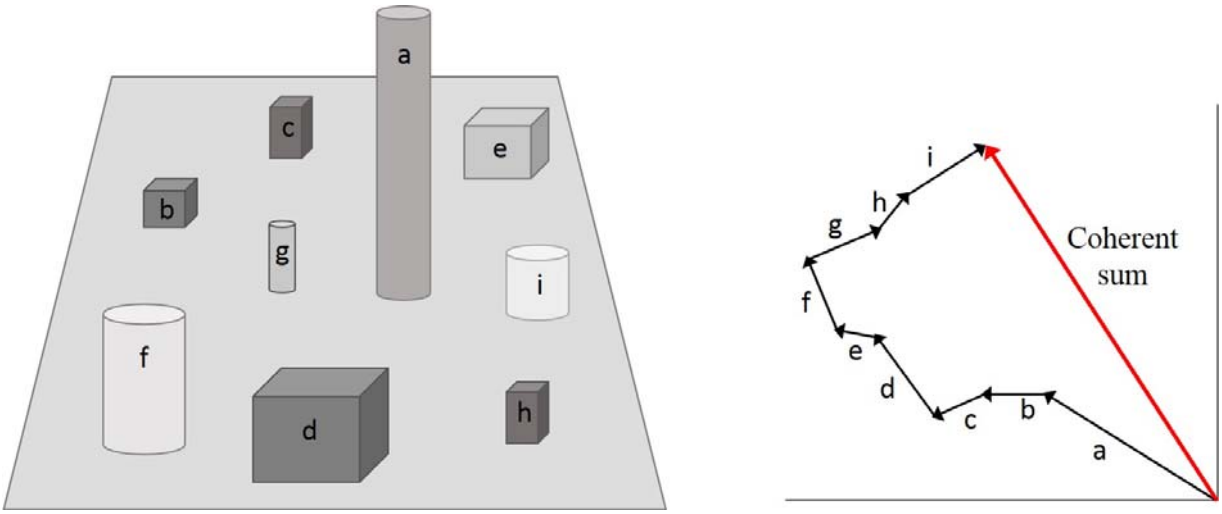

Figure 2.4. Each resolution cell is composed of many scatterer elements, each of them with different backscattering characteristics as represented in the figure on the left. The backscattered signal measured by the radar corresponds to the coherent sum (red arrow in the figure on the right) of all these individual vectors (black arrows).

2.2. SAR interferometry

SAR interferometry exploits the geometric properties of the SAR image phase to measure the elevation and deformation of the scatterers. This is accomplished by subtracting the phases of at least two different measures of the radar over the same target. The two measures need to be acquired from two nearby locations, from which the backscattered complex signal per resolution element is nearly the same except from a different propagation phase delay (Rosen et al., 2000). The two acquisitions can be taken simultaneously with two different sensors or by the same sensor in a revisit time. Figure 2.5 illustrates the repeat-pass interferometry acquisition geometry. The distance between the two satellite orbits is the interferometric baseline, and its projection perpendicular to the slant range is the perpendicular baseline ($B_\perp$). This parameter plays an important role in the topography measurement, as it is described later in this section. The complex interferogram is generated by multiplying the first SAR complex image, named master, with the complex conjugate of the second one, named slave. This operation cancels the phase shift contained in Equation 2.3, but leaves a phase term proportional to the differential path delay. This differential phase delay is the so-called interferometric phase, a geometric quantity directly related to the elevation angle of the resolution element and its movement (Rosen et al., 2000). The interferometric phase is also affected by the different phase delay propagation caused by the different atmospheric effects during both acquisitions, and by a term due to noise. The interferometric phase can be decomposed in these components:

$$\phi_{Int} = \phi_M - \phi_S = \phi_{Mov} + \phi_{Topo} + \phi_{APS} + \phi_{Noise} + 2k\pi \tag{2.4}$$

where ϕ_M and ϕ_S are the phases of the master and slave images, ϕ_{Mov} is the phase caused by the deformation, ϕ_{Topo} is the phase term due to the topography, ϕ_{APS} is the atmospheric contribution (APS stands for Atmospheric Phase Screen), ϕ_{Noise} is the noise term, and k is an integer number. The topographic phase can be expressed as a function of the perpendicular baseline $B_\perp$:

$$\phi_{Topo} = \frac{4\pi}{\lambda}\frac{B_\perp}{R_M \sin\theta} H \tag{2.5}$$

where H is the altitude of the scatterer, R_M is the range of the master, and θ is the off-nadir angle. Note that the sensitivity to topography increases with the perpendicular baseline $B_\perp$. A Digital Elevation Model (DEM) can be generated using small temporal baselines (to minimize the effects of terrain movements and decorrelation) and high spatial baselines.

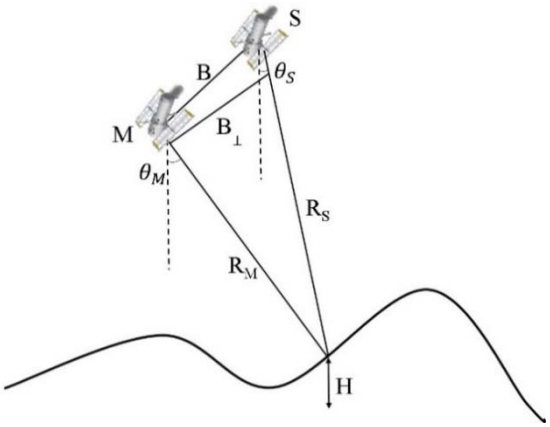

Figure 2.5. Geometry of acquisition of an interferometric SAR system, where M corresponds to the master satellite and S to the slave satellite. B is the interferometric baseline.

ϕ_{Topo} has to be removed from the interferometric phase to derive deformation measurements. This is achieved by simulating ϕ_{Topo}, using an available DEM, to obtain the so-called differential interferometric phase:

$$\phi_{DInt} = \phi_{Int} - \phi_{Topo\_simulated} = \phi_{Mov} + \phi_{RTE} + \phi_{APS} + \phi_{Noise} + 2k\pi \quad (2.6)$$

where ϕ_{RTE} is the residual topographic error (RTE) phase component, which is the difference between the true height of the scattering phase centre of a given point and the height given by the used DEM. For instance, such errors can be caused by buildings and other man-made structures if they are not included in the DEM used in the processing. The RTE plays an important role for modelling and geocoding purposes. ϕ_{Mov} is the phase related to the difference of path length travel caused by surface deformations:

$$\phi_{Mov} = \frac{4\pi}{\lambda} d \quad (2.7)$$

where d is the displacement in the LOS, λ is the wavelength, and 4π is related to the two-way path radar-target-radar. The phase components due to the APS and the noise are explained in the next sections.

2.2.1. Atmospheric effects

The interferograms from repeat-pass interferometry are affected by artefacts caused by variations in the atmosphere. These artefacts can be classified in ionospheric and tropospheric effects (Zebker, 1997). The ionospheric effects cause phase variations at large scales, although they are almost negligible in X-band (Hanssen, 2001), the data used in this work. The troposphere effects are attributable to changes in refractivity, mainly due to variations in water content, and can be divided into two groups (Hanssen, 2001):

- Vertical stratification effects caused by vertical profile variations. In differential interferometry, these effects only affect areas with pronounced topography and can only be removed if the variation in the vertical refractivity profiles is known.
- Turbulent mixing effects or 3D atmospheric variations. These effects originate differential phase variations at many different spatial scales and can only be removed if the horizontal refractivity variations in the study area during the image acquisitions is available, which is uncommon.

The APS spatial scale spans from hundreds of meters to 100-200 kilometres (Hanssen, 1998), depending on the phenomena originating the turbulence, the characteristics of a given area and the season of the year. This complicates distinguishing deformation, topography and APS effects using single interferograms.

2.2.2. Phase noise

The phase noise influences the quality of the interferometric phase. Most of the factors that contribute to the noise are related to the presence of more than one scatterer per resolution cell and to the different time and position of the sensor during the two acquisitions. The main sources of noise are geometric, temporal and Doppler centroid decorrelation (Zebker and Villasenor, 1992; Hanssen, 2001):

- Geometric decorrelation is caused by the different incidence angle of acquisition of the master and slave images, which originates a shift in the range spectra of the two SAR images. This spectral shift increases with the perpendicular baseline, reaching the critical baseline when the spectral shift is equal to the range bandwidth, i.e. when the interferometric phase is completely decorrelated.
- Temporal decorrelation is caused by changes in the characteristics of the scatterer over time. For instance, vegetated areas show very fast decorrelation over time due to the high variability of the physical properties of the scatterers. Seasonal and anthropogenic changes also produce temporal decorrelation in interferograms with large temporal baselines. By contrast, arid areas and man-made structures usually display high correlation over time.
- The Doppler centroid decorrelation is caused by differences in the Doppler centroid frequencies between two acquisitions. The Doppler centroid is zero when the antenna is ideally pointed perpendicular to the flight direction. However, if the antenna angle is squinted the Doppler centroid will be different to zero. This decorrelation increases linearly when the Doppler centroid frequency difference increases. This effect is the azimuth equivalent of the geometric decorrelation.

Other sources of noise are the thermal noise of the system and the errors associated with the data processing as those related to image co-registration. All the above mentioned terms contribute to the decorrelation of the interferometric data. A measure of the decorrelation, and hence of the quality of the interferometric phase, is the so-called coherence, described later in this chapter. Note that only pixels with a good phase quality can be used to retrieve the deformation measurements.

2.2.3. Phase unwrapping

The interferometric phase is only measured module 2π, in the range $[-\pi,\pi]$, i.e. it is wrapped: there is an ambiguity (number of phase cycles) associated with the interferometric phase. The resolution of this ambiguity, named phase unwrapping, is one of the major problems of SAR interferometry. It consists in reconstructing the unwrapped phase by means of adding the appropriate number of cycles:

$$\phi_{Int\_unwrapped} = \phi_{Int\_wrapped} + 2k\pi \tag{2.8}$$

where k is an integer number.

The phase unwrapping is an ill-posed problem and therefore some a priori assumptions need to be made. The most common assumption in phase unwrapping algorithms is the phase continuity between neighbouring pixels:

$$\left|\Delta\phi_{Int\_unwrapped}(i,j) - \Delta\phi_{Int\_unwrapped}(k,l)\right| < \pi \tag{2.9}$$

where (i,j) and (k,l) represent two neighbouring pixels. Note that, in X-band, this corresponds to a maximum relative displacement of about 7 mm. Higher relative displacement values lead to unwrapping errors, which are multiple of 2π and result in errors of the displacement measurements. These errors are particularly important in low coherence areas, where neighbouring pixels are sparse.

Many phase unwrapping algorithms have been proposed in the literature. The most direct algorithm consists in reconstructing the two dimensional unwrapped phases by integrating the phase gradients. However, this introduces a relevant source of error due to inconsistencies that depend on the integration path. One of the most used phase unwrapping algorithms to solve this

problem is the Branch-cut or Ghost-line algorithm. It consists in avoiding the paths that produce the inconsistencies by means of identifying and placing cuts between the discontinuities that cannot be crossed (Goldstein et al., 1988). Another type of unwrapping algorithm uses the least square (LS) method principle (Ghiglia and Romero, 1994), from which a method based on the Green function formulation was derived (Fornaro et al., 1996). The so-called minimum cost flow (Costantini, 1998; Costantini et al., 1999), which is formulated in terms of a global minimization problem with integer variables, is another proposed phase unwrapping algorithm. For an extensive review of the 2D unwrapping see Ghiglia and Pritt (1998).

Other phase unwrapping methods consisting in a spatial and a temporal phase unwrapping are explained later in the next section. The interferometric procedure proposed in this thesis includes a 2+1D phase unwrapping method, which is explained in detail in Chapter 4, that uses an implementation of the minimum cost flow method to perform the 2D phase unwrapping.

2.3. PSI techniques

The component ϕ_{mov} in Equation 2.6 needs to be isolated to derive deformation measurements. Different types of DInSAR techniques have been proposed in the last two decades. The classical DInSAR technique only works with pairs of SAR images and can be successfully used when the magnitude of the deformation is higher than the other contributions to the interferometric phase, which usually occurs in single deformation events reaching at least several centimetres of deformation. This technique has been widely used in seismology (Massonet et al., 1993; Peltzer and Rosen, 1995; Reilinger et al., 2000; Pedersen et al., 2001), volcanology (Massonet et al., 1995) or landslide monitoring (Nagler et al., 2002). On the other hand, it does not properly work with slow deformation events or when the presence of atmospheric artefacts is significant.

PSI is an advanced type of DInSAR based on large stacks of SAR images and suitable data modelling procedures that enable the estimation of different parameters. These parameters include the deformation time series, the average displacement rates and the so-called RTE. Different PSI techniques have been proposed in the last fifteen years. The first PSI approach, called Permanent Scatterer technique, was proposed by Ferretti et al. (2000 and 2001). These studies were then followed by a number of other contributions. The Small Baseline Subset (SBAS) technique is one of the most important and well documented PSI approaches (Berardino et al. 2002; Lanari et al., 2004; Pepe et al., 2005, 2007, 2011). A similar approach was proposed by Mora et al. (2003). Another PSI method suitable for geophysical applications is described in Hooper et al. (2004). A simplified approach based on stepwise linear functions for deformation and LS adjustment is proposed in Crosetto et al. (2005). The Stable Point Network (SPN) and the Interferometric Point Target Analysis (IPTA) are described in Crosetto et al. (2008) and Werner et al. (2003), respectively. Recently, a new algorithm called SqueeSAR, which can jointly process PSs and distributed scatterers (DS), was proposed by Ferretti et al. (2011). Further relevant contributions are: (i) adapting the LAMBDA method used in GPS to the PSI parameter estimation (Kampes and Hanssen, 2004); (ii) the use of adaptive deformation models in PSI (Van Leijen and Hanssen, 2007); (iii) a method to derive the main characteristics of PSs and classify them in main typologies of urban SAR targets (Perissin and Ferretti, 2007). Finally, it is worth mentioning the methods based on multidimensional SAR imaging, also known as SAR tomography (Lombardini, 2005; Fornaro et al., 2009).

The above mentioned PSI methods mainly differ in the method used to select the PSs and the type of model used in the PSI estimation. These aspects are discussed in the next two sections, while Section 2.3.3 addresses the problem of the PSI measurements over wide areas.

2.3.1. Candidate PS selection

PSI techniques require a pre-selection of the points to be used to derive the deformation measurements. The selected points, named candidate PSs, are points with good interferometric phase quality, i.e. with a low level of ϕ_{noise}. The PSI techniques are classified in three main categories depending on the method used to select the candidate PSs: (i) coherence, (ii) Dispersion of Amplitude (DA), and (iii) Signal-to-Clutter Ratio (SCR). These three selection methods are described below.

(i) Coherence-based selection. A measure of the phase quality is given by the so-called coherence. The complex coherence γ of a given interferogram is a statistical index that measures the degree of correlation between the pair of complex SAR images that constitute the interferogram:

$$\gamma = \frac{E[M \cdot S^*]}{\sqrt{E[|M|^2] \cdot E[|S|^2]}} \tag{2.10}$$

where M and S are the master and slave complex SAR images, E is the expected value and * is the complex conjugate. The coherence is usually calculated over windows of neighbouring pixels and, for this reason, the coherence has lower resolution with respect to the original full resolution SAR images. Further information on the coherence properties is provided in Bamler and Hartl (1998), Rosen et al. (2000) and Hanssen (2001).

The module of the coherence ranges from 0 to 1. The higher the coherence the better the phase quality, i.e. the smaller is the noise term. The relation between the standard deviation of the phase noise and the coherence for a different number of interferogram looks is described in Bamler and Hartl (1998), see Figure 2.6.

The selection of candidate PSs is performed using a coherence threshold over a stack of interferograms. The main disadvantage of this method is the low resolution of the coherence image. This method is usually employed to select DSs, e.g. see Berardino et al. (2002) and Mora et al. (2003). The methods described in these two references do not work at full SAR resolution.

(ii) DA selection. The DA criterion, proposed in Ferretti et al. (2001), is the most widely employed, e.g. see Werner et al. (2003), Kampes and Hanssen (2004), Kampes (2006), Hooper et al. (2004 and 2007), Crosetto et al. (2008) and Van Leijen (2014). It consists in a measure of the scatterer stability by means of the analysis of the amplitude along the stack of N images.

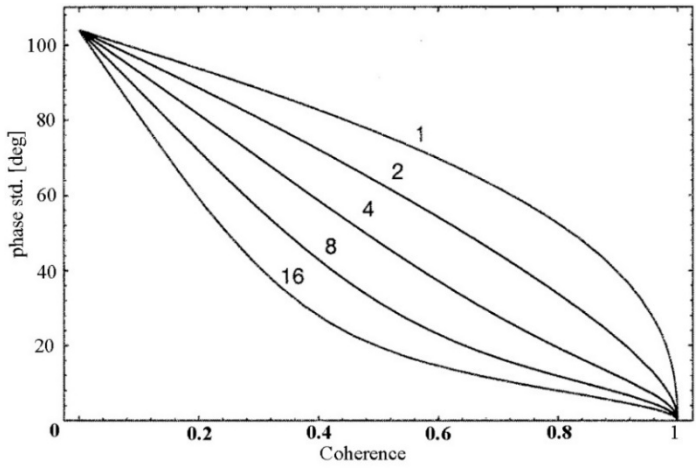

Figure 2.6. Standard deviation of the interferometric phase noise as a function of the coherence for a different number of interferogram looks, from Bamler and Hartl (1998).

The DA is estimated as the standard deviation of the amplitude (σ_A) divided by the mean amplitude (m_A):

$$DA=\frac{\sigma_A}{m_A} \tag{2.11}$$

Bamler and Hartl (1998) show that there is a linear relation between the DA and the standard deviation of the phase noise for small values of DA: low DA values indicate low phase dispersion during the period of study. The DA is a pixel-wise selection method that works at full resolution, enabling the selection of isolated points. The method is successfully used when large stacks of images, at least 25 according to Ferreti et al. (1999), are available; the criterion can be biased if the number of images is smaller.

(iii) SCR selection. Another method to select candidate PSs consists in selecting pixels above a determined threshold of SCR in a given set of images. The noise phase dispersion σ_ϕ is related to the SCR as follows:

$$\sigma_\phi=\sqrt{\frac{1}{2SCR}} \tag{2.12}$$

where the SCR is defined as the square of the amplitude of the dominant scatterer divided by the square of the amplitude of the clutter around the dominant scatterer. This method works very well in rural and sub-urban areas. However, it is complex to use in urban areas where there is a great number of interfering scatterers at short distances. This method works at full image resolution and there is no minimum number of images required. It is used in combination with the DA by Kampes and Hanssen (2004) and Kampes (2006).

2.3.2. Functional models

All the PSI methods need to unwrap the interferometric phases to estimate the deformation time series over the selected PSs. Several methods have been proposed with different models, interferogram configurations and methodologies to filter the APS.

The first PSI method, proposed in Ferretti et al. (2000 and 2001), uses a lineal model for the deformation. The phase is modelled as the sum of a RTE term and a deformation term:

$$\phi_{Dint}=\frac{4\pi}{\lambda}v\Delta t+\frac{4\pi}{\lambda}\frac{B_\perp}{R_M\sin\theta}RTE \tag{2.13}$$

where v is the linear velocity and Δt is the temporal baseline of a given interferogram. This model uses the periodogram method to avoid performing directly the phase unwrapping and it is the most widely used, e.g. see Adam et al. (2003) and Werner et al. (2003). All the available SLC images can be used if this model is implemented together with the DA, because the selected point scatterers are not affected by geometric and temporal decorrelation: this allows to use large baselines, larger than the critical baseline. Ferretti et al. (2001) propose a configuration of interferograms with a unique single master, which is exploited in most of the methods that use the DA criteria to select the candidate PSs.

Other methods, such as SBAS (Berardino et al., 2002), firstly perform the phase unwrapping spatially and then integrate the phases over time. No deformation model is applied, but the phase unwrapping is performed with the assumption of spatial smoothness of the deformation. SBAS only uses interferograms with small baselines to limit spatial decorrelation and topography errors. Only one time series per subset can be obtained when the available acquisitions are distributed in small baseline subsets, which are separated by large baselines (Lundgren et al., 2001; Usai, 2001). SBAS applies a Single Value Decomposition (SVD) method to link

independent SAR acquisitions subsets. As it uses multi-looked SAR images, this method is focused on the measurement of large-scale deformations. Lanari et al. (2004) extended the SBAS method by using a second dataset at full resolution. The residual between the low resolution result and the full resolution data is modelled using the lineal deformation model plus a non-linear term. The method proposed by Mora et al. (2003) is also based on small baseline subsets but it performs an adjustment of a linear deformation model followed by the SVD method. The non-linear component and the APS are separated by means of a spatial phase unwrapping and successive spatial and temporal filters.

STAMPS (Hooper et al., 2004 and 2007) assumes a spatially correlated deformation with no prior assumption about its temporal nature. The PSs are selected using a PS probability estimator based on the DA and a temporal measure of the phase noise coherence. This last term is estimated with an iterative algorithm that assumes that the phase components due to deformation, orbital errors and APS are spatially correlated. Hooper et al. (2004) estimate the correlated part of the interferometric phase by calculating the mean of the candidate PSs that fall into a given window. A better approach consisting in applying an adaptative band-pass filter is proposed in Hooper et al. (2007). A 3D phase unwrapping algorithm which is a combination of a temporal and a spatial phase unwrapping is applied in Hooper and Zebker (2007). A set of low and high pass filters is applied to filter the APS term after the phase unwrapping. This method operates on SLC images at full resolution, with the single master interferogram configuration. A method that exploits both the STAMPS and SBAS interferogram configurations is proposed in Hooper (2008). Note that other 3D phase unwrapping methods have been proposed in the literature (Costantini et al., 2002; Pepe and Lanari, 2006; Fornaro et al., 2011).

PSP (Costantini et al., 2008) is another method able to identify PSs in natural terrain that works at full resolution. The premise is that by working only with pairs of nearby points the problem of the APS and orbital contributions is overcome by exploiting their spatial correlation. PSP is an iterative method that uses the arc temporal coherences, exploiting a linear model of the deformation, to select the arcs and derive their linear velocity and RTE. The set of seed points can be chosen according to different criteria. One of them is to apply the arc test to all those points adjacent in the image grid. Once the PSs are selected, the linear velocity and RTE are reconstructed and the non-linear velocity is retrieved with a phase unwrapping and APS filtering steps.

Other methods, such as STUN (Kampes and Hanssen, 2004; Kampes, 2006), adapt the LAMBDA method exploiting a combination of a bootstrap estimator with an integer LS search to perform the temporal phase unwrapping before the spatial phase unwrapping (with a Minimum Cost Flow algorithm). Unlike most of the methods described here, it uses a stochastic model to describe the atmosphere term. DePSI (van Leijen, 2014) also makes use of the integer LS, bootstrap and ambiguity function to resolve the temporal ambiguity function, followed by a spatial phase unwrapping in a first order network of PSs, which is densified after the APS filtering (combination of high and low pass filters plus a stochastic model of the APS).

A new algorithm that can jointly process PSs and DSs is presented in SqueeSAR (Ferretti et al., 2011), with the aim to extend PS processing to non-urban areas. It is based on the premise that when the number of pixels sharing the same statistical behaviour is high enough, it is possible for a few of them to exceed the coherence threshold and become PSs. Two DSs are defined as statistically homogeneous points when their amplitude values of the data stack are drawn from the same probability distribution function. Then, by means of an adaptative space filter and a phase triangulation algorithm, the DSs are filtered to be processed jointly with the PSs using the traditional PSInSAR algorithm. A similar approach based on polarimetric data is proposed in Navarro-Sánchez and López-Sánchez (2014).

2.3.3. Wide area processing techniques

A new challenge for PSI is to process wide areas, i.e. full scenes or even sets of adjacent scenes, especially using high-resolution data. The availability of high-resolution data implied an increase of the PSI potentialities in terms of higher PS density and resolution. However, the processing of high-resolution SAR imagery involves a huge amount of data that implies an increase of the computational and memory requirements. Besides the computation-related problems, there are other technical problems such as those related to the inhomogeneous density of PSs in large areas. In fact, the density and quality of PSs in rural areas is considerably lower than in urban areas, which can lead to spatial error propagation, mostly caused by APS-related errors. In particular, the troposphere filtering is usually difficult in rural areas, where the PS density is low (Adam et al., 2011).

Some works addressing the wide area PSI processing have been recently proposed. Costantini et al. (2012) present two decomposition approaches to overcome the inherent computational problems related to wide area processing. The first one consists in dividing the data in blocks of smaller size. The difficulty of this approach consists in making consistent the individual blocks. Two different strategies are proposed: (1) to process the blocks sequentially, enforcing the solution from the overlapping subsets, and (2) to process the blocks independently and use a block adjusting technique to derive the composed result (this is accomplished by exploiting the 2π error nature of phase unwrapping). These strategies are prone to errors in low density areas. The second approach proposed in Costantini et al. (2012) is more robust and less prone to error propagation. It consists in the decomposition of the problem at different scales, obtained by subsampling or multi-looking the original data, according to a pyramidal scheme. In this approach, lower scales are solved and subsequently used to solve the higher scales in two possible ways: (1) as constraints in the higher scale solutions; or (2) to remove the low spatial frequencies.

Adam et al. (2011) describe the update of the DLR's operational PSI-GENESIS for wide area processing. The procedure is divided into overlapping blocks to reduce the computational load, speed up the procedure and keep errors local. The deformation is estimated over arcs with the LAMBDA estimator. The network is then inverted in a two-step procedure to estimate the velocity of deformation. First, a L1-norm inversion, consisting in a standard LS adjustment to detect and remove the outliers, is performed (Rodriguez-González et al., 2011). A second L2-norm inversion (Liebhart et al., 2010) is carried out over the outlier-free network. The L2-norm is a maximum likelihood estimator, which provides error measures with the aim of avoiding some error propagation. The APS is estimated with a troposphere effect mitigation processor that uses numerical weather prediction models (Adam et al., 2011). Finally, the blocks are merged using the common points in the overlapping areas by a LS adjustment in a single processing step. The block adjustment algorithm can be applied on adjacent full scenes using the overlapping areas. Liebhart et al. (2012) describe in detail the WAP processing algorithm and the quality controls and error propagation estimators performed over each processing step, especially in the block merging processing steps.

Chapter 3

PSI analysis over small areas

This chapter is devoted to the PSI analysis over small areas, where the APS component is generally negligible thus allowing the implementation of a simplified PSI procedure, which does not directly involve the estimation of the APS and considerably reduces the complexity and computational load of the procedure. The proposed procedure includes a linear deformation model to deal with wrapped interferometric phases avoiding the cumbersome step of phase unwrapping. However, the use of a linear model might imply a partial or total loose of PS density for those phenomena characterized by a non-linear deformation behaviour. In this regard, a model-free procedure is proposed in this work, and discussed in Chapter 4, to avoid the problems associated with the linear model assumption.

The precision of the main PSI products, i.e. the deformation velocity (v) and the RTE, mainly depends on the interferogram network available and the SAR sensor wavelength. The local area PSI chain has mainly been developed using C-band SAR data. With the availability of high-resolution X-band SAR data, and the consequent higher sensibility to subtle movements, the PSI procedure has been extended to account for the displacements caused by thermal dilation (Monserrat et al., 2011). This aspect is discussed in the second half of this chapter.

The main steps of the local PSI chain are listed in Figure 3.1 (Crosetto et al., 2011). The dashed lines represent the three main blocks of the procedure. The first block deals with the estimation of the deformation velocity and RTE using the linear deformation model. In this block, the first step is the PS candidate selection using the DA (Ferretti et al., 2001). In the second step, the differential v (Δv) and RTE (ΔRTE) values over the PSs, which are redundantly connected, are integrated to create a unique PS network. A quality index over each PS is then derived making use of the modelled phase values and the interferometric original phases. Only points with a quality index higher than a selected threshold are considered in the final maps. An optional densification is proposed in the second block, where the final PS density might be increased, if required. The steps of the first block are repeated with a new selection of PS candidates, less restrictive in terms of DA. The deformation time series for each PS are derived in the third block using a 2+1D phase unwrapping method, i.e. a spatial 2D phase unwrapping followed by a temporal 1D phase unwrapping, with the aim of deriving the N phase images temporally ordered and free of phase unwrapping errors, avoiding any model deformation assumptions (see Chapter 4). The results are finally geocoded and usually visualized using the web platform Google Earth.

This chapter is organized in three main sections. The first one describes the PS selection and the Δv and ΔRTE estimation over pairs of PSs. The second section discusses the integration of the Δv and ΔRTE values over the set of PSs to obtain the v and RTE maps, and the associated quality index. It also includes the densification block, which aims to derive dense PS maps. Note that the first and second sections only deal with the classical two-parameter model (v and RTE). The

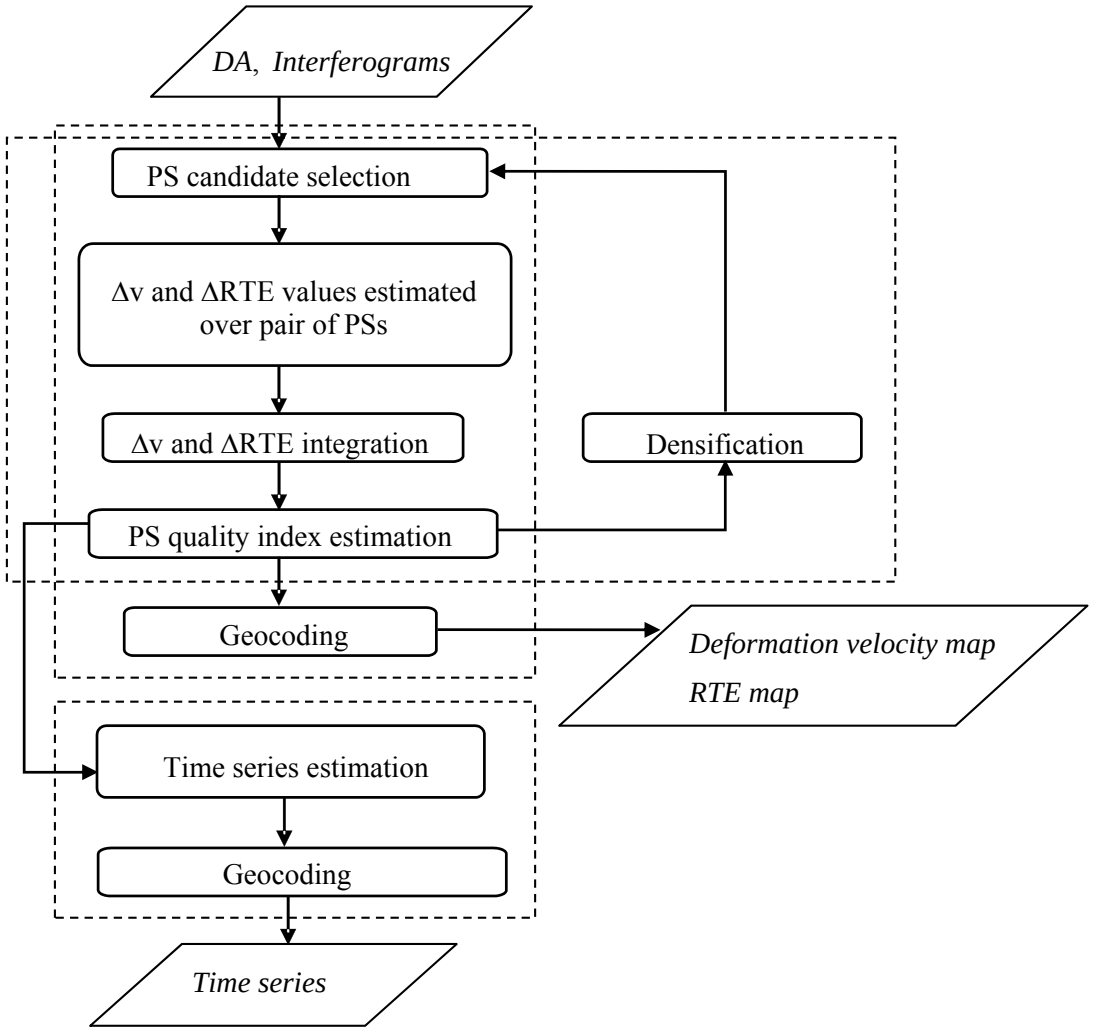

Figure 3.1. Flow chart of the local area PSI chain. The dashed lines correspond to the three main processing blocks: deformation velocity (v) and Residual Topographic Error (RTE) estimation, densification and time series estimation.

third section introduces the thermal component (Th). Therefore, the extended three-parameter model is explained in detail and the estimability of the three parameters is discussed. Finally, a comparison of the results obtained with the classical and extended models is presented in this section.

3.1. Differential deformation velocity and RTE estimation

This section concerns the two first steps of the flow chart (Figure 3.1): (i) PS candidate selection and (ii) Δv and ΔRTE estimation over pairs of PSs.

The aims of the selection of the candidate PSs are to ensure a good quality of the measured phases and to avoid errors in the estimations due to the noise. The DA criterion (Ferretti et al., 2001) is used to select points with low noise component (see Section 2.3.1). Typically, a DA threshold of 0.2 is selected in urban areas, where the density of PSs is high. In non-urban areas, such as rural and vegetated areas, the DA threshold is usually relaxed to reach the required density of candidate PSs. Consequently, a higher noise component is accepted.

The differential nature of the differential interferometric phase is exploited by considering pairs of candidate PSs (see Figure 3.2). Given an edge, e, of a pair of candidate PSs, the differential wrapped phase of an interferogram k, $\Delta\phi^k_{obs\_e}$, is computed. $\Delta\phi^k_{obs\_e}$ is modelled assuming a term related to the linear movement, $\Delta\phi^k_{linear\_mov\_e}$, a term related to the RTE, $\Delta\phi^k_{RTE\_e}$, and a residual error term, $\Delta\varepsilon^k_e$, related to the APS, noise and non-linear deformation effects:

$$\Delta\phi^k_{obs\_e} = \Delta\phi^k_{linear\_mov\_e} + \Delta\phi^k_{RTE\_e} + \Delta\varepsilon^k_e = \frac{4\pi}{\lambda}\Delta t^k \Delta v_e + \frac{4\pi}{\lambda}\frac{B^k_\perp}{R^k \mathrm{sen}\theta^k}\Delta RTE_e + \Delta\varepsilon^k_e \quad (3.1)$$

where Δv_e is the differential linear velocity of the edge e, ΔRTE_e is the differential residual topographic error, Δt^k and $B^k_\perp$ are the temporal and perpendicular baselines of the interferogram, R^k and $\theta^k$are the slant range and incidence angle of the interferogram k, and λ is the radar wavelength.

Given an edge e, Δv_e and ΔRTE_e are estimated using the method of the periodogram. The best fit between $\Delta\phi_{obs\_e}$ and the model proposed in Equation 3.1 is sought. This is equivalent to minimize the residuals $\Delta\varepsilon_e$, i.e. to maximize the function γ_e for the edge:

$$\gamma_e = \frac{1}{M}\sum_{k=1}^{M} \exp\left(j\cdot\Delta\varepsilon^k_e\right) \quad (3.2)$$

where M is the total number of interferograms and $\Delta\varepsilon^k_e$ is given by:

$$\Delta\varepsilon^k_e = \Delta\phi^k_{obs\_e} - \Delta\phi^k_{model\_e} = \Delta\phi^k_{obs\_e} - \Delta\phi^k_{linear\_mov\_e} - \Delta\phi^k_{RTE\_e} \quad (3.3)$$

The gamma function 3.2 takes values between 0 and 1, reaching its maximum when the residual errors are zero. The higher is the maximum γ_e, the better is the fit to the model of the wrapped phases. Note that the presence of non-linear motion during the period of study decreases the gamma value because a linear deformation is assumed. It is worth to mention that the interferogram network influences the shape of the gamma function. For instance, the peak of the function is thinner in the case of large $B_\perp$ distributions.

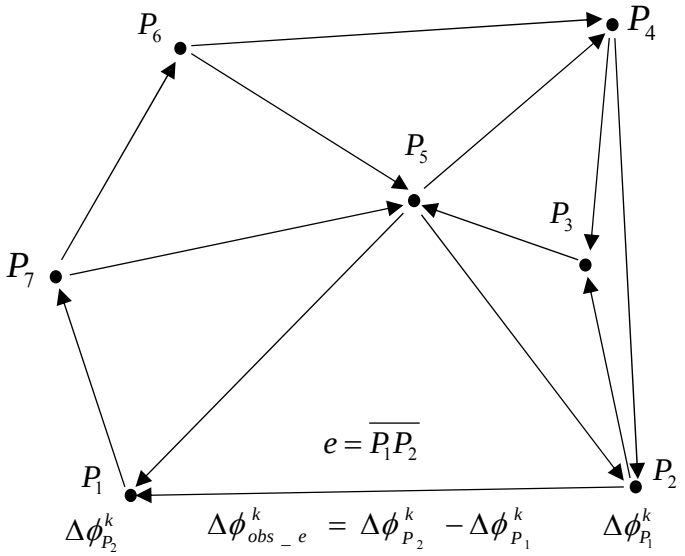

Figure 3.2. Network of connected Persistent Scatterers (PSs). For each edge the differential interferometric phase is calculated and the differential deformation velocity and Residual Topographic Error (RTE) are estimated. Figure adapted from Biescas et al. (2007).

Figure 3.3 illustrates the γ_e function for four different edges with maximum values of 0.25, 0.45, 0.65 and 0.85, respectively. It is easily noticeable that the maximum is better defined for higher values of γ_e. More than a maximum appear for $\gamma_e(max) = 0.25$, while higher values of $\gamma_e(max)$ progressively display a unique and better-defined maximum, as can be seen in the case of $\gamma_e(max) = 0.85$.

The maximization of Equation 3.2 is solved numerically: the function γ_e is calculated over a grid of intervals of Δv_e and ΔRTE_e. The solution is given by the pair of Δv_e and ΔRTE_e values that provide the maximum γ_e value. The resolution of the results depends on the number of intervals selected. The denser the grid, the better is the resolution. However, the computation time increases with the number of intervals tested. An approach to overcome this problem has been implemented, which exploits two different scale grids: the interval grid and the subinterval grid. A coarse estimation is performed over the interval grid to find an approximate solution, which is fast in terms of computation time. This is followed by a second estimation over the subinterval grid, where the search space around the first solution is divided in a finer search grid. The subinterval length drives the resolution of the solution. This process reduces the computation time by a factor $subintervals^n$, where n is the number of model components (in this case two: RTE and v).

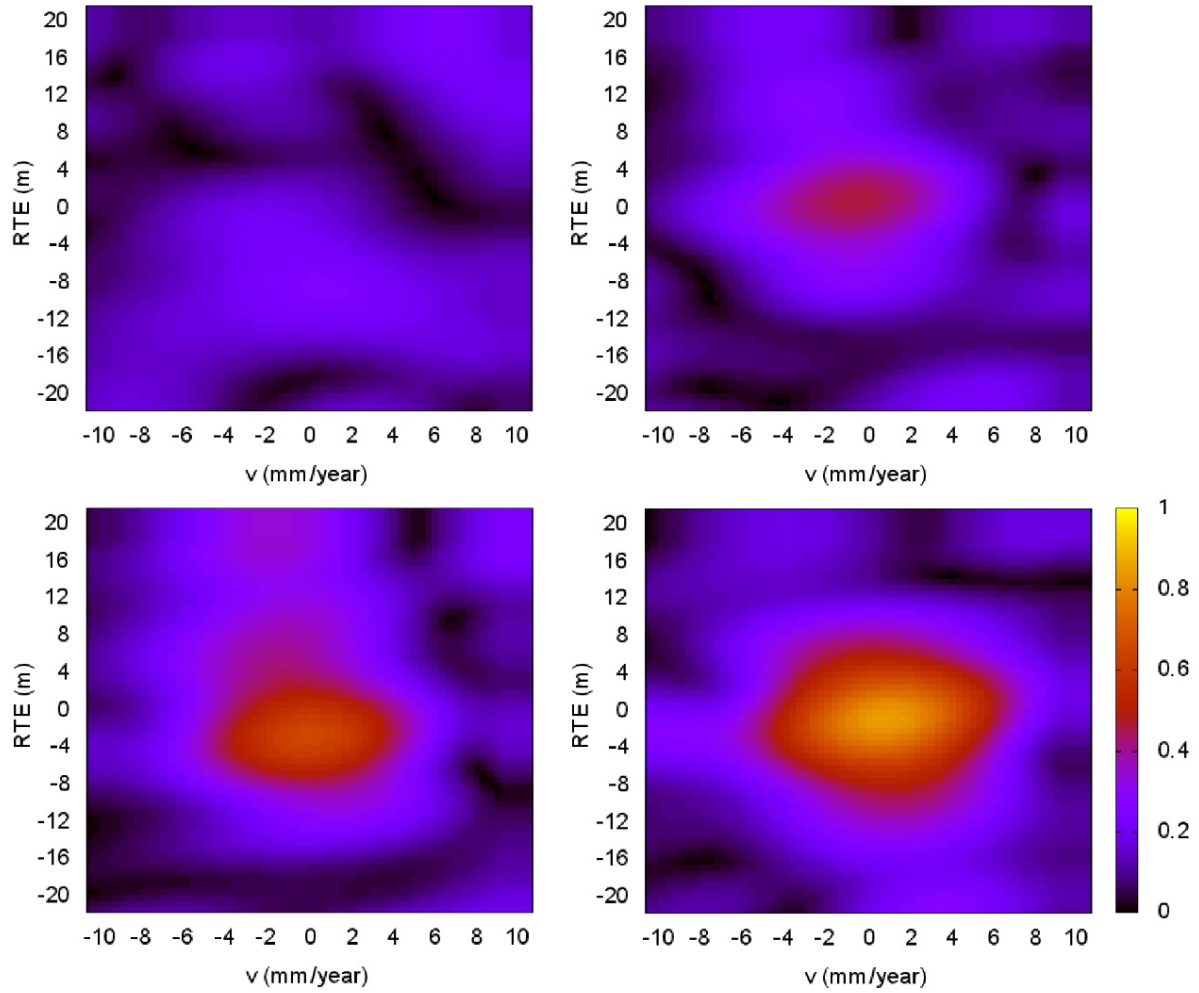

Figure 3.3. Gamma functions of four edges with a maximum value of 0.25 (upper left), 0.45 (upper right), 0.65 (bottom left) and 0.85 (bottom right), obtained from a stack of 51 TerraSAR-X interferograms over Barcelona.

The above process is repeated over a number of edges, which are selected with a maximum distance criterion taking into account that large distances are affected by atmospheric contributions. The number of tested edges needs to be large enough to enable the construction of a redundantly connected network. This is required to correctly estimate the v and RTE maps, as explained in next section. The candidate PSs that are redundantly connected with γ_e higher than a given threshold are selected (using X-band data the threshold usually ranges between 0.7 and 0.8). The threshold can be adjusted depending on the area of interest, e.g. by accepting lower gamma edges to connect PSs in difficult areas or areas with non-linear motion or, contrarily, increase the threshold to enhance the quality of the estimations. A redundantly connected network of PSs is obtained at the end of this step, with Δv and ΔRTE associated with each pair of PSs.

3.2. Deformation velocity and RTE maps

This step involves the reconstruction of the velocity and RTE using the network of edges and PSs selected in the previous step. This reconstruction is accomplished by means of a weighted LS method, where the weight is derived from the gamma of each edge. Considering the deformation velocity, the main observation equation is given by:

$$\Delta v_e = v_i - v_j \tag{3.4}$$

where v_i and v_j are the unknown velocities over the PSs i and j that are connected by the edge e. The estimation is performed relative to a reference point, i.e. a stable point is generally chosen. The above equation can be written as:

$$b = Av + E \tag{3.5}$$

where b is the transposed differential velocity vector, A is the design matrix, v is the vector of the unknowns and E is the transposed vector of residuals. The LS method consists in estimating the solution v that minimizes the sum of squares:

$$E(v) = (b - Av)^T W(b - Av) \tag{3.6}$$

where T indicates the transposed vector and W is a weight matrix related to the gamma value of each edge. The weights are modulated by γ_e . The solution $\hat{v}$ is given by:

$$\hat{v} = -\left(A^T \cdot W \cdot A\right)^{-1} \cdot A^T \cdot W \cdot b \tag{3.7}$$

The same procedure is implemented for RTE. A redundantly connected network of PSs is usually employed, which can be a limitation in non-urban areas where the density of PS can be very low.

3.2.1. Example of deformation velocity and RTE maps

In this section, two examples of PSI results obtained using the local PSI analysis are presented. The examples are a deformation velocity and an RTE maps derived from a set of StripMap TerraSAR-X images acquired over the metropolitan area of Barcelona during the period spanning from December 2007 to November 2009.

Figure 3.4 displays the RTE of the twin skyscrapers of the Barcelona Olympic Port. This RTE map was derived from a stack of 13 images with perpendicular baselines up to 491 m. The dense network of PSs over the two towers illustrates the high spatial resolution of the analysed data. The maximum height of the RTE map is 150 m, which almost matches the maximum height of the towers that is 154 m. The good quality of the estimated heights, which can also be appreciated by the quality of the PSs geocoding, is mainly due to the short wavelength of X-band data and their high spatial resolution.

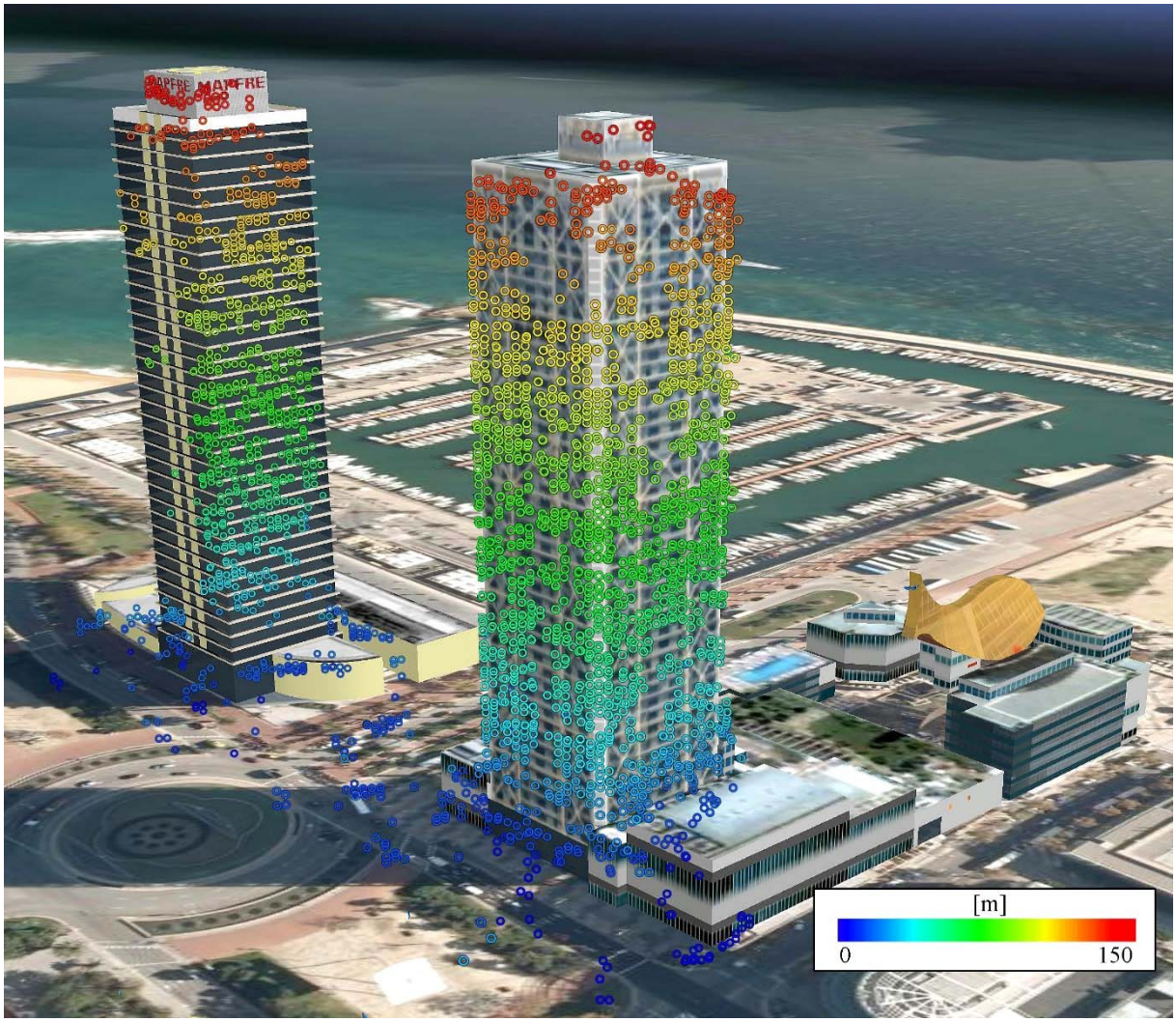

Figure 3.4. Residual Topographic Error (RTE) estimated over the twin skyscrapers of Barcelona Olympic Port. The 3D view is based on Google Earth. Figure from Crosetto et al. (2010).

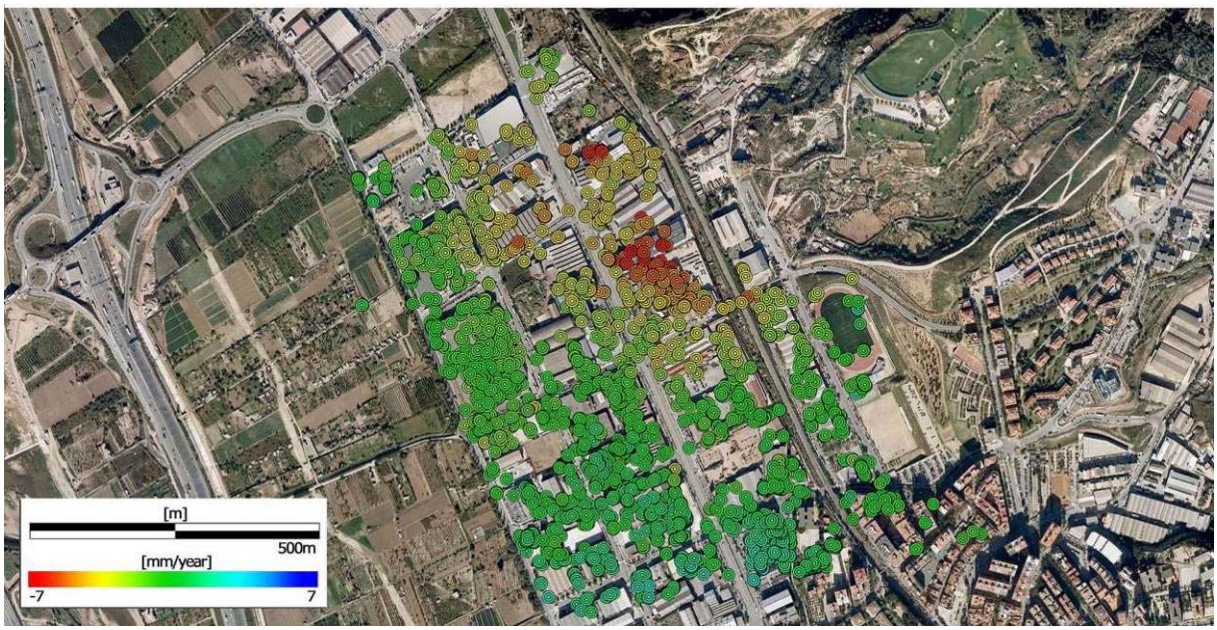

Figure 3.5. Geocoded deformation velocity map superimposed over a Google Earth image. The area displayed is an industrial area of the municipality of Molins de Rei, located near Barcelona.

The deformation velocity map of an industrial area of the municipality of Molins de Rei is shown in Figure 3.5. The deformation velocity was derived from a stack of 28 images using the linear deformation model. The figure shows the geocoded map superimposed over a Google Earth image, where a portion of the area suffers subsidence, with deformation rates up to 7 mm/yr. As explained in Crosetto et al. (2011), this phenomenon was previously observed using ERS and ASAR-Envisat imagery, starting in 1992 and covering almost 18 years.

3.2.2. PS quality index

A quality index of the estimations, γ_{PS}, is calculated PS wise to measure the quality of the PSI results. This index is based on the phase residual (res) between the original and the modelled interferometric phases of a given PS:

$$res_k = \Delta\phi^k_{obs} - \Delta\phi^k_{model} \tag{3.8}$$

The quality index is given by:

$$\gamma_{PS} = \frac{1}{M}\sum_{k=1}^{M} \exp(j \cdot res_k) \tag{3.9}$$

where M is the number of interferograms. The index takes values between 0 and 1. The PS estimations that perfectly fit the model have $\gamma_{PS}=1$. PSs with γ_{PS} lower than a given threshold are usually removed from the results. This index is defined with respect to a selected reference point and its values typically decrease as the distance from the reference increases. Note that the index measures the degree of fit to the linear deformation model, i.e. how the observations fit the linear deformation model. Consequently, the same low value of γ_{PS} can be either due to a non-linear motion or the presence of noise in the observations. This fact has to be carefully considered when judging the quality of the PSs in deformation areas.

An example of non-linear deformation is illustrated in Figure 3.6. The area is affected by non-linear deformation caused by underground works in Plaça de Maragall (Barcelona). The velocity map was derived from 28 TerraSAR-X images acquired during the period 2007-2009. Figure 3.6a illustrates the velocity of deformation without γ_{PS} filtering, i.e. accepting all the PSs. Only those PSs with $\gamma_{PS} > 0.6$ are displayed in Figure 3.6b; most of the PSs affected by motion do not pass the threshold.

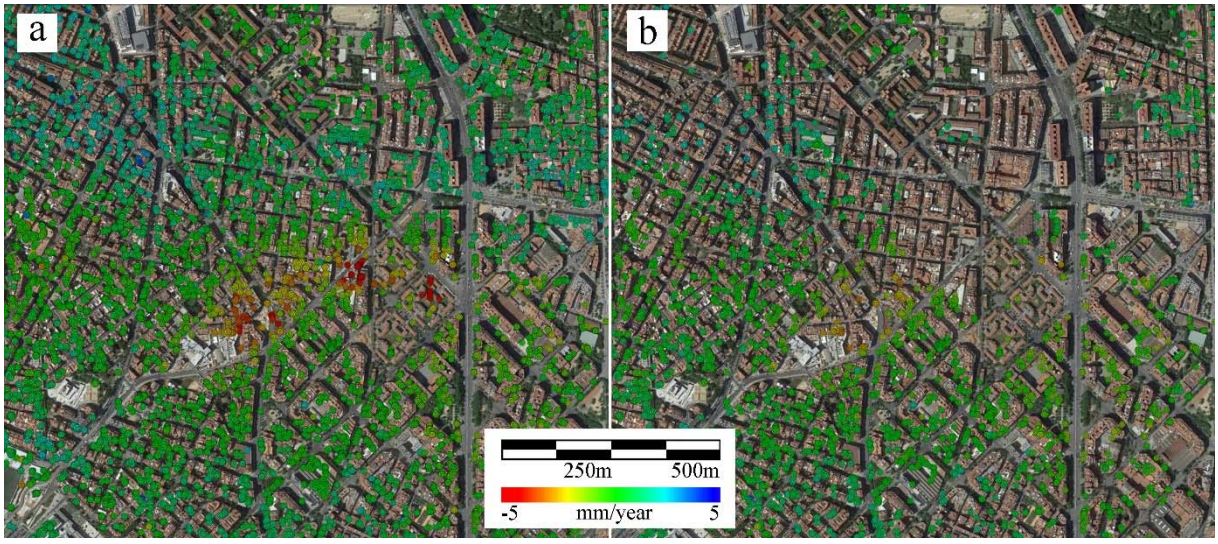

Figure 3.6. Deformation velocity map of the area of Plaça de Maragall (Barcelona), superimposed on a Google Earth image, without γ_{PS} filtering (a) and using a filter of $\gamma_{PS}>0.6$ (b). This area is undergoing non-linear deformation due to underground works.

3.2.3. Densification of the PS maps

If the PS density achieved in the first analysis is not enough, a densification of the first order PS network can be performed. The densification step involves a second iteration of the following steps (see Figure 3.1): (i) a new selection of candidate PSs, (ii) Δv and ΔRTE estimation over pairs of first and second order PSs, (iii) v and RTE integration over the dense net of PSs, and (iv) quality index computation.

The second order set of candidate PSs is selected by relaxing the DA threshold used to select the first order PSs. The accepted noise in the candidate PS phases is consequently higher. However, the second order edges are selected to connect the second order candidate PSs with the first order PSs, which are points with high quality phase. The number of estimated edges per PS is a trade-off between the computation time, which increases with the number of edges, and the need to achieve a dense network of PSs redundantly connected. Figure 3.7 shows a scheme of the second order PS network, which includes the new candidate PSs, blue points, which connect to the first order network, black points. Note that this procedure may be repeated in order to achieve the required density of points to study a given deformation area.

The PSI processing in non-urban areas, where the PS density is generally low, often requires the densification step. Figure 3.8 shows the densification over the area of Montjuïc (Barcelona). Some points in the first order velocity map (Fig. 3.8a) display mean deformation velocity of up to -4 mm/year in the LOS (orange points) and up to -5 mm/year for a single point (in red). However, a correct interpretation of the deformation phenomenon is only achieved through a densification of the PS network. Figure 3.8b displays the second order (densified) velocity map, which clearly shows the spatial extend of two main deformation phenomena. The phenomenon located in the upper part of the image shows the stronger deformation values, with LOS velocities of up to -6 mm/year. The second phenomenon displays LOS velocities up to -5 mm/year.

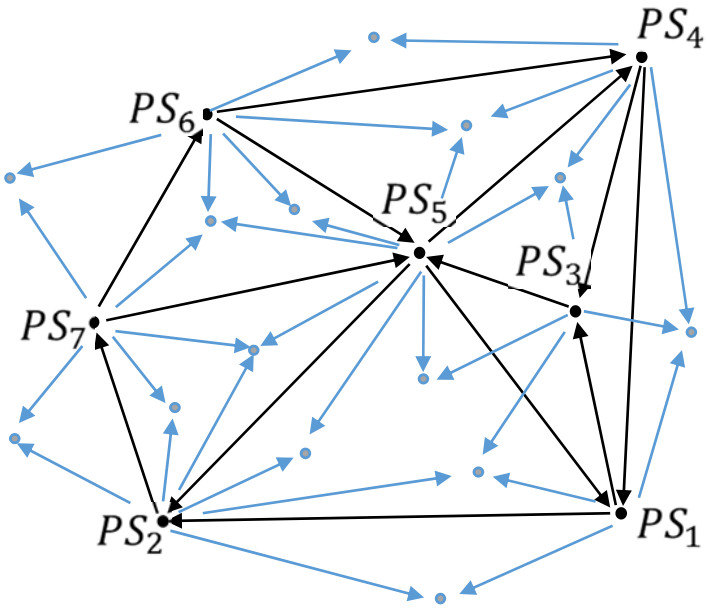

Figure 3.7. Illustration of the Persistent Scatterer (PS) densification. The second order network (blue points) are connected to the first order PSs (black points), PS_1 to PS_7. The blue arrows represent the new edges and black ones are the first order network.

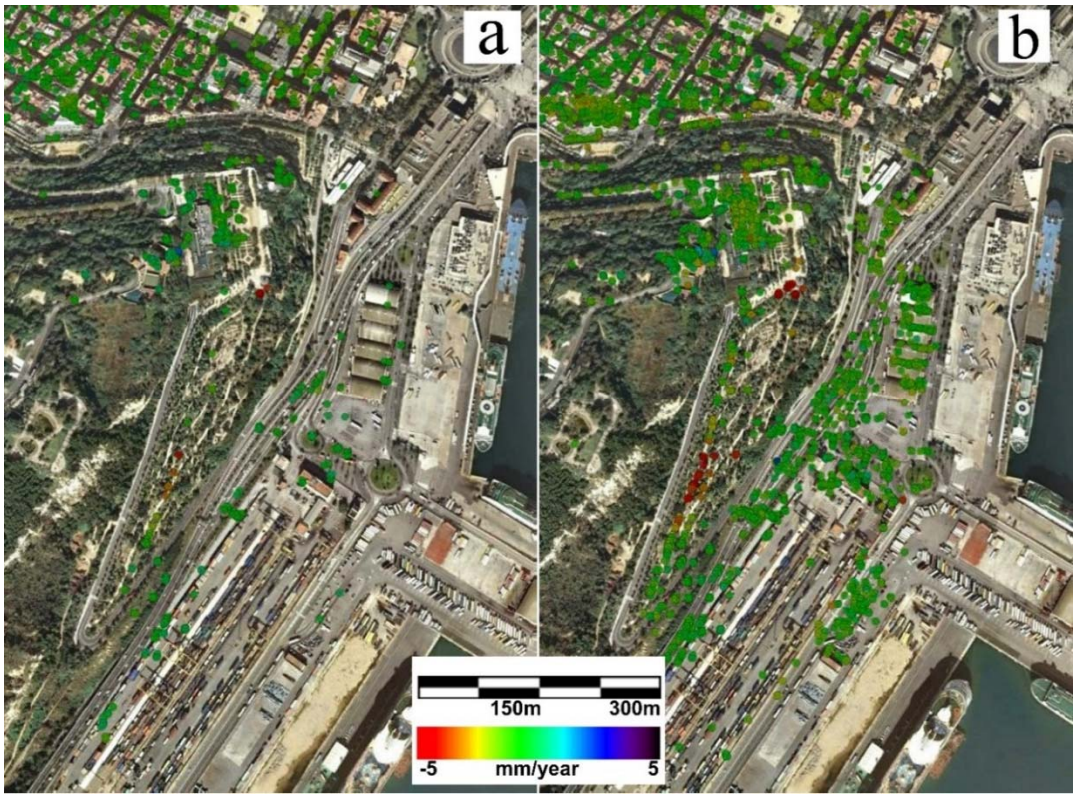

Figure 3.8. First order deformation velocity map of Montjuïc (Barcelona) (a); second order (densified) map of the same area (b). Both maps are geocoded and superimposed on a Google Earth image.

3.3. Thermal dilation estimation: extension of the model

The availability of high resolution X-band SAR data, such as TerraSAR-X and CosmoSkyMed, resulted in an improvement of the PSI results due to the higher image resolution and phase quality. The high resolution increases the PS density with respect to C-band data, and the higher phase quality results in an improvement of the precision of the RTE estimation and an increased sensibility to subtle movements (Crosetto et al., 2010). This sensibility allows measuring a new parameter, the thermal dilation, i.e. the displacements caused by temperature changes. Although the thermal dilation effects have been observed in several works with C-band, e.g. see Ferretti et al. (2005), Perissin et al. (2006), and Crosetto et al. (2008), the role of thermal dilation is much more important in high resolution X-band data. For this reason, the thermal dilation component needs to be precisely estimated in order to avoid mixing up the signal caused by terrain deformation with the signal attributable to thermal dilation. This can be achieved by extending the two-parameter model (RTE and v), see Equation 3.1, to a three-parameter model that includes a thermal dilation parameter (Th), see Monserrat et al. (2011) and Cuevas et al. (2011):

$$\Delta\phi^k_{obs} = \Delta\phi^k_{linear\_mov} + \Delta\phi^k_{RTE} + \Delta\phi^k_{thermal} + \Delta\varepsilon^k \tag{3.10}$$

where $\Delta\phi^k_{thermal}$ is the thermal dilation phase component. This component is related to the difference of temperature at the time of acquisition of the images that form the interferogram k (Monserrat et al., 2011):

$$\Delta\phi^k_{thermal} = \frac{4\pi}{\lambda}\Delta Temp^k \cdot \Delta Th \tag{3.11}$$

where $\Delta Temp^k$ is the difference of temperatures between the two acquisitions of interferogram k, and ΔTh is the differential thermal dilation parameter. This new component is added to the

two-parameter model, modelling the differential wrapped interferometric phase, for a given edge and interferogram, as follows:

$$\Delta\phi^{k}_{obs\_e} = \frac{4\pi}{\lambda}\Delta t^{k}\Delta v_e + \frac{4\pi}{\lambda}\frac{B^{k}_{\perp}}{R^{k}sen\theta^{k}}\Delta RTE_e + \frac{4\pi}{\lambda}\Delta Temp^{k}\cdot\Delta Th_e + \Delta\varepsilon^{k}_{e} \quad (3.12)$$

Note that the extended model is more accurate than the two-parameter model. The estimability of Δv_e, ΔRTE_e and ΔTh_e depends on the available network of SAR images and the distribution of the vectors Δt, $B_{\perp}$and $\Delta Temp$ of the interferogram network. In particular, as stated in Monserrat et al., (2011): (i) the number of SAR images needs to be larger than in the standard model, (ii) the observed period has to be as large as possible, and (iii) the correlation between the distribution of the above-mentioned vectors of parameters needs to be minimized in the selection of the interferogram network.

The maximization of γ_e (see Equation 3.3) for each edge becomes computationally heavier due to the third additional term. The γ_e dependence on Δv_e, ΔRTE_e and ΔTh_e is plotted in Figure 3.9 for two different edges with maximum values of 0.85 and 0.35, respectively. The first row of the figure plots γ_e as a function of ΔRTE_e and Δv_e. The middle row shows γ_e as a function of ΔTh_e and Δv_e, and the bottom row shows the plots for γ_e as a function of ΔRTE_e and ΔTh_e. Note that in the three plots the $\gamma_e(max)= 0.85$ has a unique and well-determined maximum, while $\gamma_e(max)= 0.35$ has multiple relative maxima of approximately the same value. As in the two-parameter model, higher values of γ_e imply a better fit to the linear model: only edges with γ_e higher than a determined threshold are considered in the PS network (see Section 3.1). Considering the example from Figure 3.9, the 0.85 edge would be included in the PS network, while the 0.35 edge would not.

The optimal selection of the interval and subinterval grids to find the Δv_e, ΔRTE_e and ΔTh_e values that maximizes the gamma function highly depends on the network of available interferograms. The grids are selected by studying the γ_e dependence on the three mentioned variables, e.g. using similar plots like those shown in Figure 3.9. The optimum interval is the maximum that allows locating the absolute maximum with no ambiguity. The subinterval length is selected according to the resolution needed in the results. Note that, as mentioned in Section 3.1, the subdivision of the grid reduces the computation time in subintervals^n, where n is the number of components of the model (in this case 3). The use of subintervals is particularly needed in the extended (three-parameter) model because the computation time can be extremely slow due to the third additional component.

The extended model allows deriving the v map, the RTE map and the thermal map. The three differential parameters are estimated over a number of edges and are then integrated over a connected redundant network of PSs relative to a selected reference point (see Sections 3.1 and 3.2). The selected reference point is usually required to be stable (no movement due to either ground deformation or thermal dilation effects) and be on the ground (no RTE). Note that the reference point can be different for each of the three maps.

It is important to mention that other approaches to handle the thermal dilation effects in PSI data have been proposed in the literature during the last years. For instance, Gernhardt et al. (2010) and Duro et al. (2010) use a sine function to model the seasonal deformation changes. The model proposed in this thesis is more accurate than the sine model because it explicitly makes use of the temperatures at the time of acquisition of the SAR images, thus capturing the portion of the thermal dilation that linearly varies with temperature. Finally, Fornaro et al. (2013) and Reale et al. (2013) extend the multi-dimensional imaging approach by introducing the thermal dilation parameter.

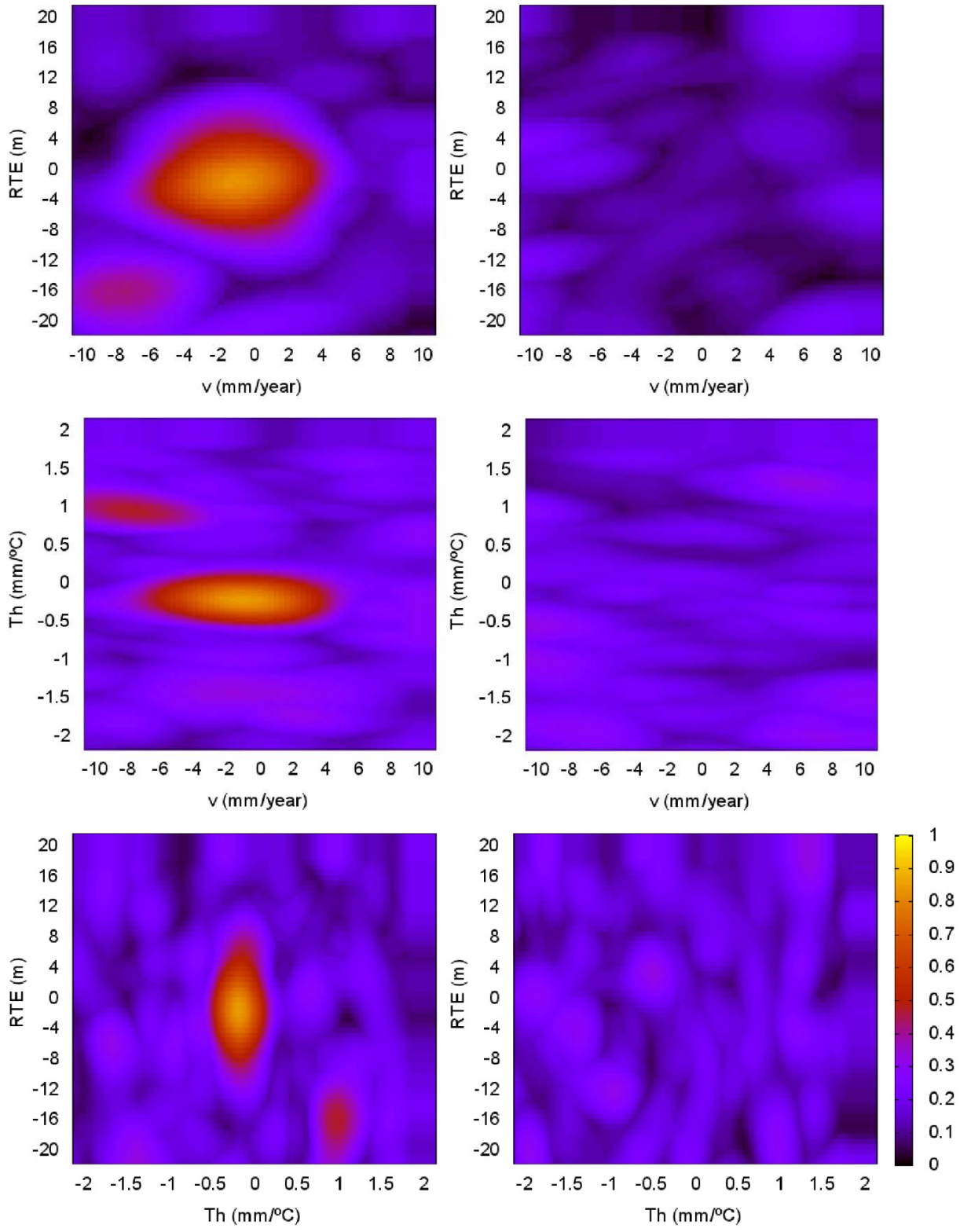

Figure 3.9. Function γ_e of two edges with maximum γ_e of 0.85 (left) and 0.35 (right), plotted as a function of the Residual Topographic Error (RTE), deformation velocity (v) and thermal dilation (Th). The upper row plots γ_e as a function of ΔRTE_e and Δv_e. The middle row represents γ_e as a function of ΔTh_e and Δv_e. Finally, the bottom row shows the plots for γ_e as a function of ΔRTE_e and ΔTh_e.

3.3.1. Example of thermal dilation maps

Thermal maps enable the interpretation of the thermal expansion signal of single objects such as buildings, bridges, etc. This leads to interesting applications related to the study of specific properties of the observed objects, such as their thermal expansion coefficient and their static structure. In this section, a thermal map of a viaduct derived with the extended model and high-resolution X-band is analysed. Figure 3.10 shows the velocity map (3.10a) and the thermal dilation map (3.10b) of a viaduct located in Montmeló (Barcelona, Spain) derived with 27 StripMap TerraSAR-X images covering the period from December 2007 to November 2009. The velocity map shows that the viaduct structure is stable. The thermal map, analysed in Crosetto et al. (2014), displays a periodic pattern of 96 m, with thermal effects that reach -0.35 mm/ºC away from the satellite and 0.3 mm/ºC towards the satellite in the LOS, respectively. Note that, in Barcelona, the air temperature variation from winter to summer is approximately 20ºC. This variation corresponds to a thermal displacement of -7 mm and 6 mm in the LOS, respectively. Assuming that the movement is caused by horizontal thermal dilation along the main direction of the bridge and for a length of 96 m, this corresponds to an estimated coefficient of linear thermal dilation of $11.7 \cdot 10^{-6}$/ºC, which is typical for reinforced concrete. In addition to this coefficient, it is possible to deduce directly the static structure of the bridge from the thermal expansion map, i.e. only using remote sensing data, as it is shown in Figure 3.11.

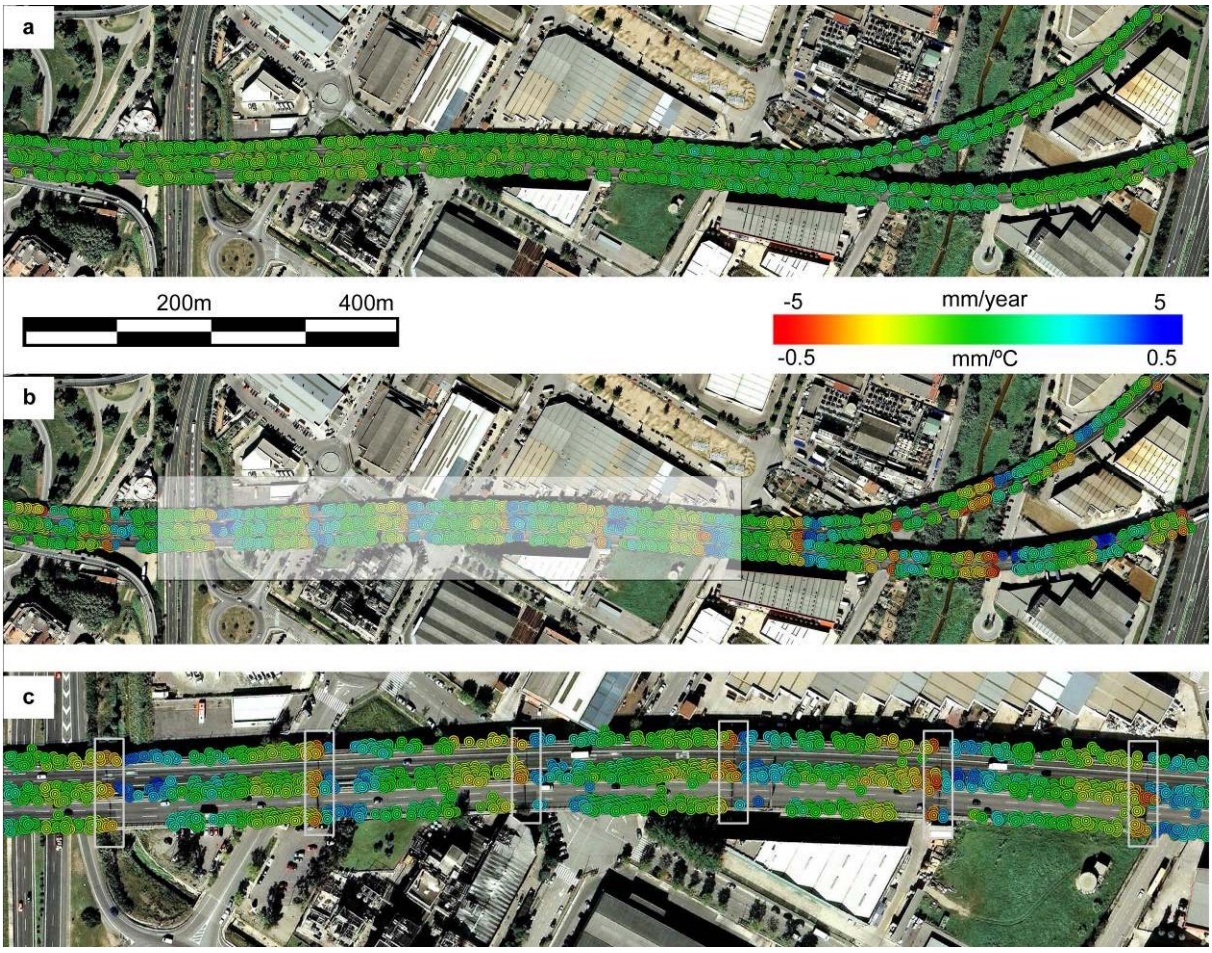

Figure 3.10. Geocoded velocity map (a) and thermal map (b) of a viaduct located in Montmeló (Barcelona, Spain); (c) shows a zoom over the rectangle shown in (b). The white squares shown in (c) indicate the positions of the viaduct expansion joints. The maps are superimposed over a Google Earth image.

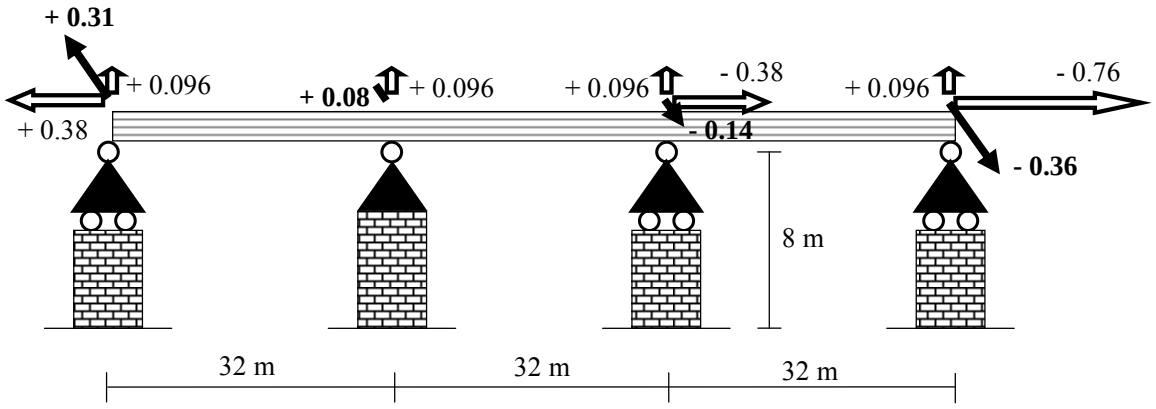

Figure 3.11. Scheme of a 96-m section of a viaduct limited by a pair of thermal joints. The scheme includes four supports: a pinned joint (2nd support from the left) and three slider joints. The white arrows indicate the vertical and horizontal components of the thermal dilation parameter, Th, while the black arrows represent their projection in the Line of Sight (LOS) direction. All the values, excluding those of the geometry that are expressed in [m], are in [mm/ºC].

3.3.2. Non-modelled thermal dilation effects

The thermal dilation component of PSI observations cannot be neglected, especially when X-band data is being used. In fact, thermal effects, if not properly handled, can lead to errors in the estimation of the velocity of deformation, i.e. there is a risk of obtaining deformation products that contain spurious patterns due to non-modelled thermal dilation effects. This risk increases if the PSI products are derived from PSI datasets that cover short periods, e.g. several months. In this section, a comparison of the outputs of the two-parameter model and the extended three-parameter model is presented to illustrate the importance of properly modelling thermal dilation (Crosetto et al., 2014).

Figure 3.12 shows the deformation velocity maps estimated using the two-parameter model and the extended one. These maps were derived using 13 StripMap TerraSAR-X images that cover the period December 2007 to September 2008. Figure 3.12a shows an orthoimage of the area of interest. Figure 3.12b shows the velocity map estimated with the classical two-parameter PSI model, where strong deformation patterns are visible displaying deformation velocities ranging from -20 to +20 mm/year. This result differs substantially from the velocity map estimated using the extended PSI model, see Figure 3.12d. The difference reflects the effect of thermal dilation, which is not modelled in Figure 3.12b and, as a consequence, generates distortions in the velocity map, thus creating a kind of "virtual displacement rates". By contrast, when the thermal dilation component is properly modelled using the extended model, it generates a much more accurate deformation velocity map and, in addition, the thermal map is obtained, see Figure 3.12c.

It is worth noting that the velocity map shown in Figure 3.12d still displays a residual thermal pattern caused by the limited PSI dataset used (13 images) that does not allow the velocity to be perfectly separated from the thermal parameter. The thermal map shown in Figure 3.12c displays values that range approximately between -0.6 and +0.5 mm/ºC. These values reflect the displacements of the roofs of the analysed buildings. Note that the pattern that is visible in the thermal map is directly related to the LOS direction of the SAR images, which is indicated in Figure 3.12a.

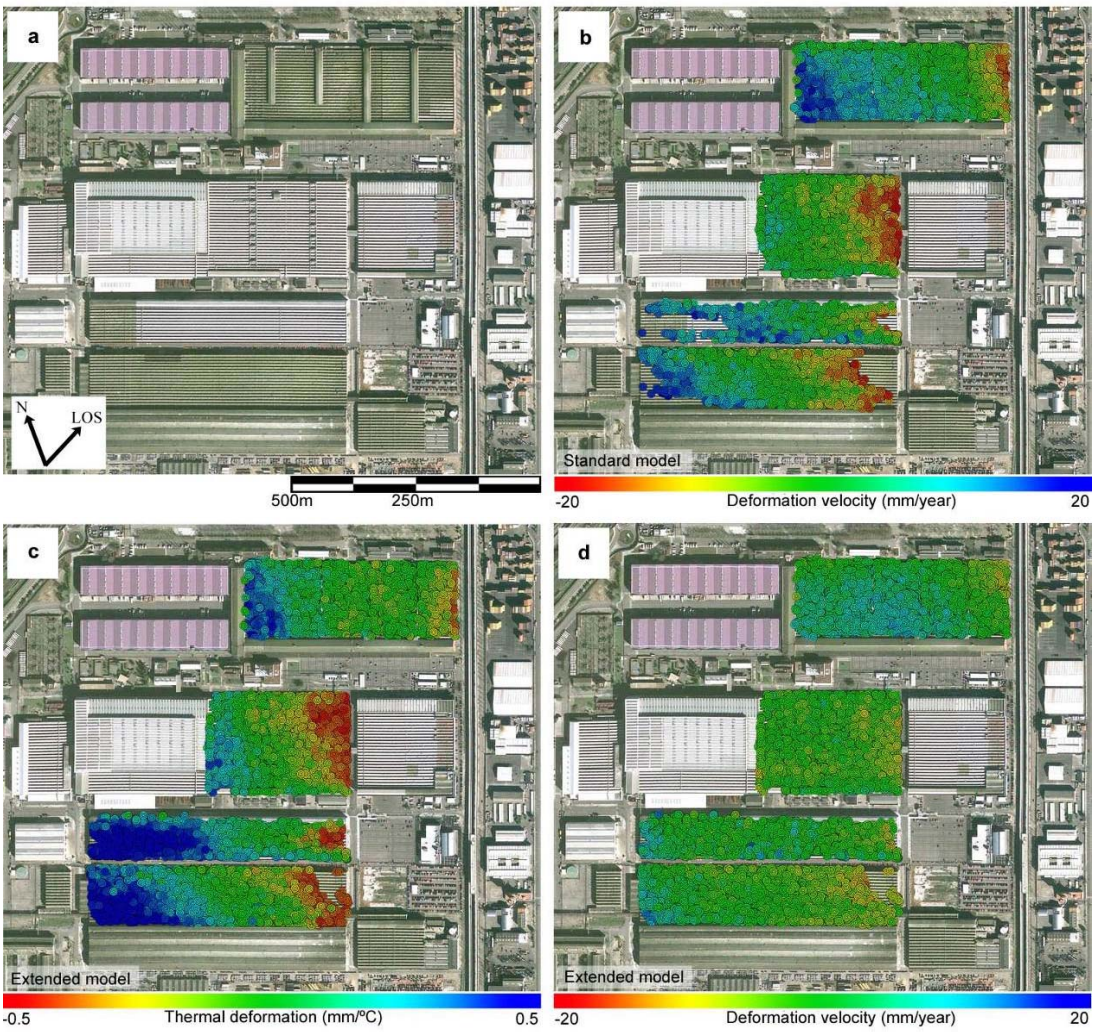

Figure 3.12. Orthoimage of the industrial park of interest (a). Geocoded deformation velocity map estimated using the standard PSI model (b). Thermal map (c) and velocity map estimated using the extended PSI model (d). The maps are superimposed over a Google Earth image.

Chapter 4

The PSIG procedure

This chapter describes the key features of the PSI chain developed at the Institute of Geomatics, now CTTC: the PSIG chain. This chain has been recently described in Devanthéry et al. (2014). As explained in Chapter 3, a complete PSI chain was already implemented and successfully used with C-band (ASAR-ENVISAT and ERS-1/2 from the European Space Agency) and X-band data (TERRASAR-X from the DLR and Astrium, and CosmoSkyMed from the Italian Space Agency) at the beginning of this work, see (Crosetto et al., 2010; Crosetto et al., 2011). However, most of the results derived with this initial processing chain concerned urban areas. The chain was mainly used to perform local PSI deformation studies, e.g. see Crosetto et al. (2005) and Biescas et al. (2007).

The main objective of the PSIG chain was to extend the interferometric processing to wider areas using a unique, redundant and connected network of points and any type of interferometric SAR data. This implied maintaining the PS density usually accomplished in urban areas using the local area PSI chain and to obtain a sufficient PS density outside the urban areas. The goal was to attain a unique set of deformation measurements covering the available full scenes, i.e. typically 30 by 50 km using StripMap TerraSAR-X, 40 by 40 km using StripMap CosmoSkyMed data, 100 by 100 km using ASAR-ENVISAT and ERS data and, in the near future, 250 by 250 km using the Interferometric Wide Swath of the Sentinel-1 data.

The PSIG procedure consists of three main processing blocks (see Figure 4.1). Its inputs include a stack of N co-registered SAR images, the DA and M wrapped interferograms, with M>>N; typically more than 10 interferograms per image are used. The goal of the first block is obtaining a set of correctly unwrapped and temporally ordered phases, which are computed on PSs that cover the area of interest with a homogeneous density. In the second processing block, the APS component is estimated using spatio-temporal filters and removed from the original interferometric phases. In the third block, the deformation map and time series are computed on a dense network of PSs. The main processing steps included in each block (see Figure 4.1) are briefly outlined below.

The first processing block is subdivided in three steps:

- Candidate Cousin PS (CPS) selection. A set of candidate CPSs characterized by a moderate spatial phase variation is selected. This key step is performed iteratively starting from at least one seed PS and searching for PSs with similar phase characteristics.
- 2D phase unwrapping. In this step, the phase unwrapping of the network of CPSs selected in the previous step is performed. An implementation of the Minimum Cost Flow method (Costantini, 1998; Costantini et al., 1999) is used.
- Phase unwrapping consistency check. This step ensures the good performance of the phase unwrapping. It is based on a temporal LS estimation and the analysis of the consistency between redundant observations. In this step the final set of CPSs is obtained.

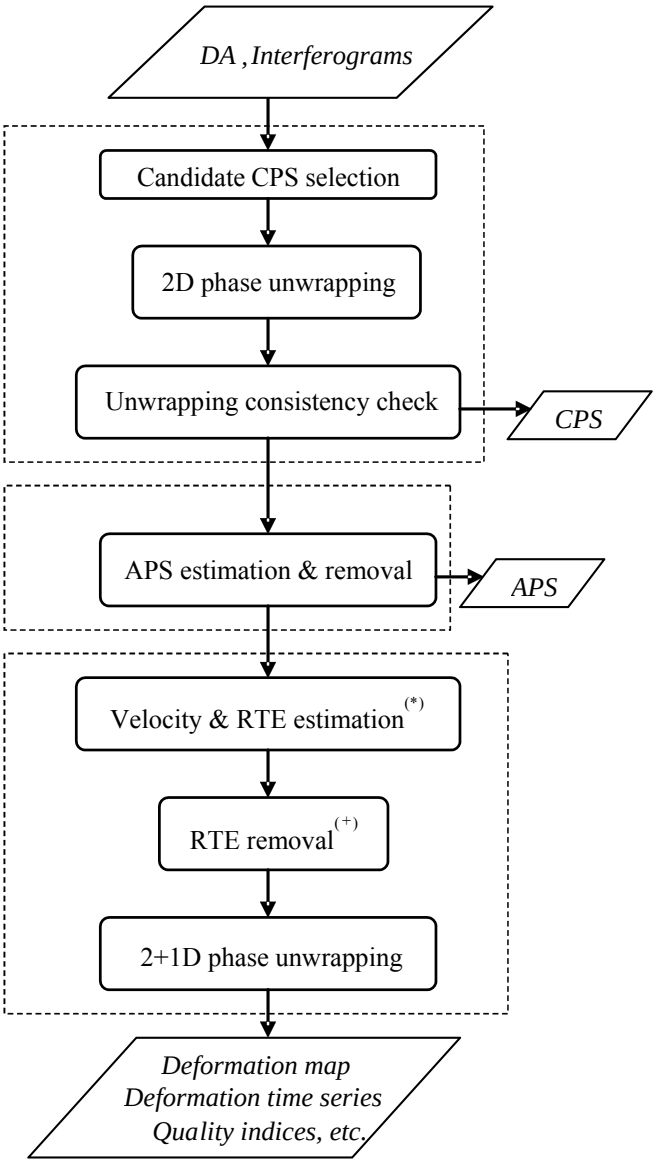

Figure 4.1. Flow chart showing the main processing steps of the PSIG chain. The dashed lines indicate the three main processing blocks. Notes: (*) The thermal dilation component can optionally be estimated. (+) The deformation velocity and the thermal dilation phase components can optionally be removed.

In the second processing block, the APS estimation and removal, which are important steps for any wide area product, are performed. This block is subdivided into two main steps:

- APS estimation. It is performed over the CPS network obtained in the first processing block using a set of spatio-temporal filters, e.g. see Ferretti et al. (2000) and (2001), Berardino et al. (2002), and Mora et al. (2003).
- APS removal. The estimated APS phase component is removed from the original differential interferograms.

The third block involves the densification of the CPS network and the computation of the deformation time series. This is accomplished through three main steps:

- Estimation of v and RTE over a dense network of points. The v and RTE (and, optionally, the thermal dilation, see Monserrat et al. (2011)) are obtained from the M wrapped APS-free interferograms, using the method of the periodogram.

- RTE removal. The RTE component is removed from the M wrapped APS-free interferograms. Optionally, the thermal dilation component can also be removed. This step is required in order to ensure a correct unwrapping over the dense network of points.
- 2+1D phase unwrapping. This last step consists in a spatial 2D phase unwrapping over the RTE- and APS-free differential interferograms, and a temporal 1D phase unwrapping used to compute the final deformation time series and a set of parameters that describe their quality.

4.1. First processing block: CPS selection

The goal of this processing block is obtaining correctly unwrapped and temporally ordered phases over a set of CPSs, which have to cover the area of interest as homogeneously as possible. As mentioned before, the three main steps of this block are the candidate CPS selection, the 2D phase unwrapping and the phase unwrapping consistency check. In the next two sections, the candidate CPS selection algorithm and the phase unwrapping consistency check are explained in detail.

4.1.1. Candidate CPS selection

A set of PSs, whose phases are characterized by moderate spatial variations, is sought in this step in order to correctly unwrap the interferometric phases. Note that the classical PS candidate selection based on the DA criterion (Ferretti et al., 2001) cannot be used in this context because the spatial phase unwrapping (the step that follows the candidate CPS selection) over the selected points would not be possible. In fact, the DA criterion does not guarantee a moderate spatial phase variation.

The CPS selection is carried out using an iterative search propagation criterion based on the k-d tree algorithm (Bentley, 1975; de Berg et al., 2008) and a condition of phase similarity. The procedure starts with the selection of at least one seed PS located on the ground, displaying no motion or thermal dilation and characterized by low noise: $\phi_{Defo\_SEED} = 0$, $\phi_{Thr\_SEED} = 0$, $\phi_{RTE\_SEED} = 0$, and ϕ_{Noise_SEED} as small as possible. The candidate CPSs are those PSs that satisfy the following condition:

$$\left|\Delta\phi^{unw}_{i,\,SEED}\right|_{90\%} < Thr \tag{4.1}$$

where $\left|\Delta\phi^{unw}_{i,\,SEED}\right|_{90\%}$ is the 90th percentile of $\left|\Delta\phi^{unw}_{i,\,SEED}\right|^{k}_{90\%}$, where k runs over the minimum set of N-1 independent interferograms, N is the number of images and Thr is the phase difference threshold. This percentile will be indicated as P_{90} hereafter. The use of the 90th percentile confers robustness to the filter as it can cope with up to 10% of outliers. Note that the phases differences values $\Delta\phi^{wrap}_{i,\,SEED}$ are unwrapped using this direct rule:

- if $\left|\Delta\phi^{wrap}_{i,\,SEED}\right| < \pi$ then $\Delta\phi^{unw}_{i,\,SEED} = \Delta\phi^{wrap}_{i,\,SEED}$
- if $\Delta\phi^{wrap}_{i,\,SEED} < -\pi$ then $\Delta\phi^{unw}_{i,\,SEED} = \Delta\phi^{wrap}_{i,\,SEED} + 2\pi$
- if $\Delta\phi^{wrap}_{i,\,SEED} > \pi$ then $\Delta\phi^{unw}_{i,\,SEED} = \Delta\phi^{wrap}_{i,\,SEED} - 2\pi$

This operation is repeated for all the PSs that fall within a given window, which is centred on the seed. The window size (Win) is set to minimize $\Delta\phi_{Atmo_{i,SEED}}$. It is worth noting that the above condition is more restrictive than those based on the classical two-parameter model (mean v and RTE), see Fornaro et al. (2009) and Costantini et al. (2008). However, the proposed procedure is computationally lighter than that based on the two-parameter model. In addition, and more importantly, it includes tools to check the consistency of the phase unwrapping, see next section.

The above operation is repeated recursively, using the new candidate CPSs as seeds, until the entire area of interest is sufficiently covered by CPSs. It is important to note that each point is tested only once, i.e. if it does not fulfil the phase similarity criterion at the first test, it is discarded. Additional seeds might be required in order to cover isolated areas or to increase the CPS density in certain areas.

The parameters used in the candidate CPS selection might change depending on the sensor and the area of interest. The most important parameter to be determined is Thr. As it is discussed in Section 4.1.3, Thr is defined as a function of the distance from the seed in order to take into account the APS effects. The choice of this value is a trade-off between low phase variation, which ensures a correct phase unwrapping, and the need to connect all parts of a given area of interest. The latter aspect is critical when the area of interest includes rural and vegetated areas where the PS density can be very low. By contrast, it is not very relevant in urban areas, where the choice of Thr can be very restrictive. The use of restrictive Thr values can have some interesting applications, e.g. selecting only PSs that are on the ground or the PSs located at a given height, which can be fixed through the seed PS. Note that the higher the perpendicular baselines distribution is, the more selective can this filter be. The size of the search window, Win, is the second parameter to be determined. The selection of the values of Win and Thr is discussed in Section 4.1.3.

4.1.2. Phase unwrapping consistency check

The candidate CPS selection, described in the previous section, is followed by the phase unwrapping, which is performed using an implementation of the Minimum Cost Flow (Costantini, 1998; Costantini et al., 1999). The unwrapping is performed spatially, interferogram by interferogram, over the M interferograms. Due to the phase similarity criterion used for the selection of the CPS candidates, it is expected that most of the phases are correctly unwrapped. However, errors can occur when the phase changes due to RTE are large or, similarly, where there are strong deformation gradients. Furthermore, a common source of unwrapping errors is given by phase variations due to the atmospheric component, particularly when the CPS density is low, e.g. in the case of isolated areas. Finally, the noise can also produce unwrapping inconsistencies over specific points. The phase unwrapping errors have to be detected in order to avoid errors in the estimated phases, and, consequently, in the deformation estimates.

A phase unwrapping consistency check is performed to determine if the unwrapping has been correctly performed over the selected candidate CPSs. The CPSs that satisfy this check constitute the final network of CPSs. As already mentioned, the check is based on a pixel wise LS estimation and an analysis of the residues. The observation equation is given by:

$$\Delta\phi_{MS} = \phi_S - \phi_M \tag{4.2}$$

where $\Delta\phi_{MS}$ is the unwrapped interferometric phase (the observation), S and M are the slave and master images and ϕ_S and ϕ_M are the corresponding unknown phases.

Each i^{th} image contains the following phase components:

$$\phi_i = \phi_{Defo\_i} + \phi_{Thr\_i} + \phi_{Atmo\_i} + \phi_{RTE\_i} + \phi_{Noise\_i} \tag{4.3}$$

where ϕ_{Defo_i} is the deformation component, ϕ_{Thr_i} is the thermal dilation component, ϕ_{Atmo_i} is the atmospheric component, ϕ_{RTE_i} is the RTE component and ϕ_{Noise_i} is the phase noise.

For each pixel, a system of M equations with N-1 unknowns can be written, where M is the number of interferograms and N is the number of images. The phase of the first image ϕ_0 is set to zero, due to the differential nature of the observations. The system of observation equations can be expressed as:

$$b = A \cdot x \tag{4.4}$$

where $b = (\Delta\phi_{0l}, \cdots, \Delta\phi_{ij}, \cdots, \Delta\phi_{mN-1})^T$ is the M-dimensional observation vector, A is the design matrix that expresses the set of scalar equations in matrix form and $x = (\phi_1, \cdot\cdot, \phi_i, \cdot\cdot, \phi_j, \cdot\cdot, \phi_{N-1})^T$ is the N-1-dimensional vector of unknowns. A stochastic model is associated with the functional model, which is represented by the weight matrix P. In this case, P is the identity matrix: it is assumed that the observations have equal precision and are independent. The LS solution is given by:

$$\hat{x} = -\left(A^T \cdot P \cdot A\right)^{-1} \cdot A^T \cdot P \cdot b \tag{4.5}$$

where $\hat{x}$ is the vector of estimated unknowns. The vector of the a posteriori estimated observations $\hat{b}$ can be re-estimated from $\hat{x}$, and the vector of residuals $\hat{\phi}_{res}$ is then derived:

$$\hat{b} = A \cdot \hat{x} \tag{4.6}$$

$$\hat{\phi}_{res} = b - \hat{b} \tag{4.7}$$

A candidate CPS is finally selected if the vector of residuals satisfies the following condition:

$$\hat{\phi}_{res} = \vec{0} \tag{4.8}$$

This condition ensures the spatial and temporal consistency of the phase unwrapping. Note that most of the discarded candidate CPSs usually correspond to isolated or bad connected areas prone to phase unwrapping errors, and to scattered points with high RTE. A check of the distribution of the CPSs needs to be carried out to ensure a homogeneous density over the entire area of interest. If this is not achieved, the procedure is resumed using new seeds to search for new candidate CPSs.

4.1.3. Choice of the parameters

The choice of the parameters used in the CPS selection, Thr and Win, is discussed in this section. These parameters are regulated by a criterion of moderate spatial phase variation to avoid phase unwrapping errors (see Section 4.1.1) and, implicitly, ensure low phase noise in order to maximize the likelihood of obtaining good CPS time series. The choice of these parameters highly depends on the type of processed SAR data. The following discussion refers to X-band data.

Let's consider the parameter Thr. Different components such as the phase noise, the RTE, the phase due to terrain movement and the APS term contribute to P_{90}. Considering the ideal case of points located on the ground ($\Delta\phi_{RTE} \sim 0$), with no motion ($\Delta\phi_{defo} \sim 0$), and located very close to the seed ($\Delta\phi_{APS} \sim 0$), P_{90} only depends on the noise of a given candidate CPS. This noise is directly reflected in the CPS time series. The maximum P_{90} allowed in terms of noise can be determined by fixing the maximum standard deviation accepted in the time series, σ_{TS}. A maximum σ_{TS} of 1.2 mm, i.e. 0.5 rad, was assumed in this work. Assuming that the noise follows a Gaussian distribution so that 90% of the population is located in the range $\pm 1.65\sigma_{TS}$, this corresponds to a Thr of 0.8 rad. This parameter is restrictive enough to ensure the low spatial

variation required to avoid unwrapping errors between the seed and the CPS. The corresponding ΔRTE and Δv are limited by Thr and basically depend on the perpendicular and temporal baseline distribution of the M interferograms.

Let's see the effects on ΔRTE and Δv considering a stack of 28 TerraSAR-X images covering the period December 2007 to November 2009, and with perpendicular baselines distributed between –170 and 150 m. Assuming negligible noise, no motion and no atmospheric effects, Figure 4.2a shows the RTE contribution to the interferometric phase as a function of the perpendicular baseline and its effect on P_{90} (red line). In this case, the maximum ΔRTE allowed between a seed and a CPS, using Thr equal to 0.8 rad, is 2 m. Assuming negligible noise, negligible atmosphere and ΔRTE~0, Figure 4.2b shows the effect of relative motion on the interferometric phase as a function of the temporal baseline and its effect on the P_{90} (red line). The maximum allowed motion in this case is approximately 1.25 mm/year. It is worth noting that that the above values correspond to the P_{90} between a seed and a given CPS: the distribution of RTE and motion of the final set of selected CPSs can be sensibly wider due to the CPS search algorithm used. In addition, it is important to take into account that the above values are only valid for the specific distribution of perpendicular and temporal baselines of the considered dataset.

Figure 4.3 shows the distribution of P_{90} over the Barcelona airport for the same interferogram configuration used in the previous analysis. There is only a limited number of CPSs with Thr below 0.8 rad (black crosses), which are located close to the seed (white circle). However, many more CPSs were expected in this area because RTE~0, there is no motion and a good response to the X-band SAR signal is usually obtained over the runways. The cause of this poor result is related to a clear dependency on the distance caused by the atmospheric effects. For this reason, there is the need to add a distance-related term to the Thr value discussed above. In order to do this, the behaviour of ϕ_{APS} as a function of the distance was studied by analyzing the autocorrelation of 27 TerraSAR-X APS images. The autocorrelation function was computed for each APS image, see Figure 4.4. The same figure shows the mean autocorrelation function μ(D) of the 27 APS images. The plot shows that for short distances, typically shorter than 100 m, the autocorrelation of the APS component is close to 1. This value decreases sharply for distances longer than 300-400 m.

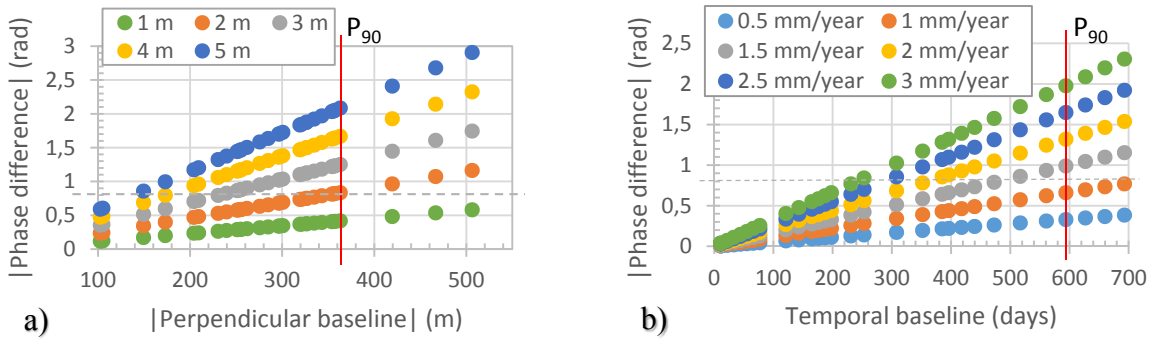

Figure 4.2. Influence of RTE on the interferometric phase difference between a seed and a candidate CPS, as a function of the perpendicular baseline (a). Influence of the relative motion on the interferometric phase difference between a seed and a candidate CPS, as a function of the interferogram temporal baseline (b). Both plots refer to a dataset of 28 TerraSAR-X images.

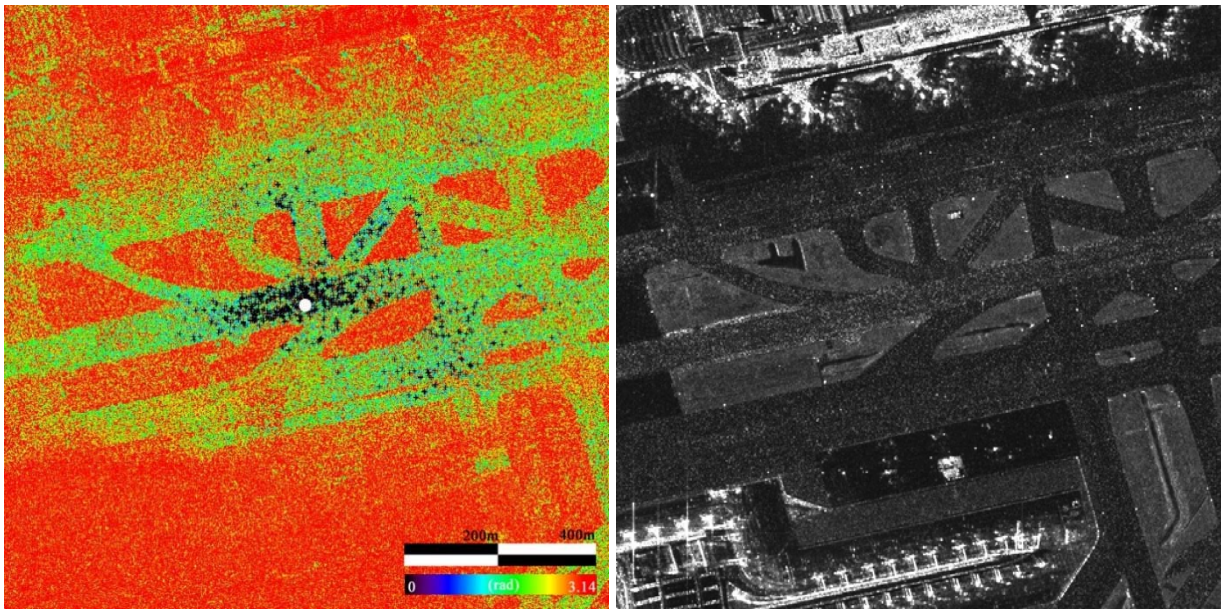

Figure 4.3. P_{90} distribution with respect to a seed (white point) located on a runway of the Barcelona airport, calculated using a stack of 28 TerraSAR-X StripMap images. The CPSs selected using Thr equal to 0.8 rad are shown by black crosses (a). Mean amplitude image (MA) of the same area (b).

The variance of the APS, $Var_{APS}(D)$, was computed as follows:

$$Var_{APS}(D)=[1-\mu(D)]\cdot Var_{image} \tag{4.9}$$

where Var_{image} is the mean variance of the 27 analysed APS images. The threshold of the phase difference Thr(D) due to the APS was defined as:

$$Thr(D)=2\sigma_{APS}(D)=2\sqrt{Var_{APS}(D)} \tag{4.10}$$

where $\sigma_{APS}(D)$ is the standard deviation of the APS as a function of the distance. The plot of Thr(D) is shown in Figure 4.5.

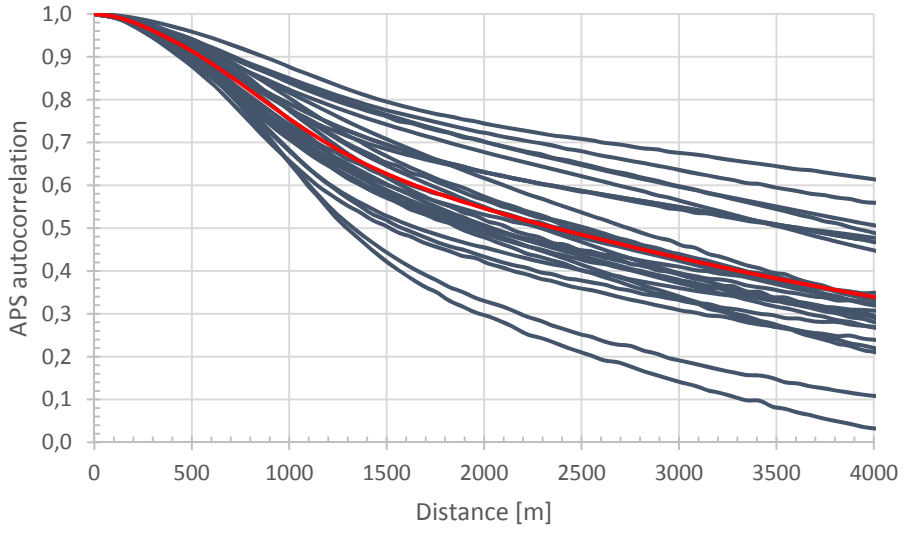

Figure 4.4. Autocorrelation functions of 27 TerraSAR-X Atmospheric Phase Screen (APS) images. The mean autocorrelation function is shown by a red line.

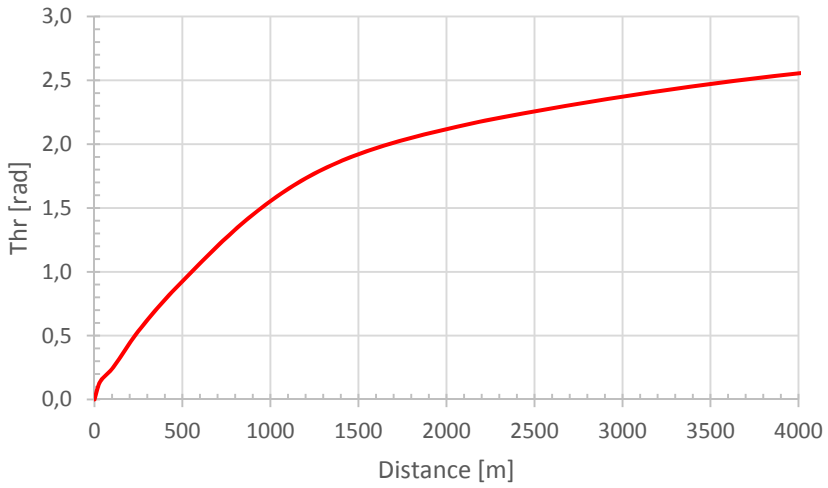

Figure 4.5. Plot of Thr(D) computed using 27 TerraSAR-X APS images.

Let's consider the second parameter, Win. A relatively large Win is needed to facilitate the CPS propagation. On the other hand, Win has to be small enough in order to reduce the influence of the ϕ_{APS} between the seed and the CPS candidates. Usually, the minimum window that allows CPS propagation to the entire area of interest is selected. This value strongly depends on the characteristics of the area and the PSI dataset at hand. Therefore, it has to be adjusted for each area of interest. In this work, Win was set to 400 pixels.

4.2. Second processing block: APS removal

The atmospheric phase component removal (second block of Figure 4.1) is a fundamental step in any wide-area PSI processing. Its goal is the correct separation of the APS from the deformation signal. The N APS images are estimated and the APS component is removed from the M interferograms to achieve this goal.

4.2.1. APS estimation and removal

In this work, a low pass filter (LPF) is applied to remove the low frequencies associated with large spatial correlation phenomena. A temporal filter is then applied to separate the APS signal from the temporally correlated components, usually related to terrain deformation.

A low pass Butterworth filter is executed over the N-1 unwrapped phase images to estimate the N-1 candidate APS images. The filter is performed in the frequency domain, i.e. over the Fast Fourier Transform of the phases. The APS images are finally obtained with the inverse Fast Fourier Transform:

$$APS_i = FFT^{-1}\left(FFT(\phi_i)\cdot H(\Omega)\right) \tag{4.11}$$

where APS_i is the candidate APS of the i^{th} image, ϕ_i is the i^{th} phase image and $H(\Omega)$ is the transfer function that, unlike the ideal LPF, presents a smooth discontinuity in order to filter correctly the high frequencies without changing the signal of concern. The transfer function is:

$$H(\Omega) = \frac{1}{\sqrt{1+\left(\Omega/\Omega_C\right)^{2N}}} \tag{4.12}$$

where Ω is the APS frequency, Ω_C is the cut-off frequency (CO), and N is the order of the filter. The slope of the transfer function is sharper for higher order values. N was set to 1 in this work.

The CO selection is a key step of the APS estimation as those frequencies that are lower than this value will be associated with the atmosphere. The obtained APS wavelength is directly related to the spatial extend of the image and inversely proportional to the CO. Figures 4.6a and 4.6b show the performance of the LPF using CO = 30, i.e. 1.7 km spatial wavelength, and CO = 6, i.e. 8 km spatial wavelength, respectively. Both candidate APS estimations show a similar APS pattern, although the candidate APS shown in Figure 4.6b displays a smoother phase pattern.

Those deformations displaying spatial correlation higher than the APS wavelength are included in the candidate APS component. A temporal high pass filter is required to separate these deformation phase components from the APS. The signal correlated in time is estimated and removed from the candidate APS with this second filter. Discriminating between the part of the signal that is APS from that that is deformation is often not straightforward. In this work, in case of doubt in discerning between the two components, the candidate APS are considered APS. It is worth noting that if the CPS selection is restrictive enough and the CPSs are located outside the deformation areas, the temporal high pass filter can be avoided, at least for relatively small areas surrounded by stable areas. By contrast, the temporal filter is required in wide-area deformation phenomena.

Once the N APS are estimated, the M synthetic APS are derived:

$$\phi_{APS_{MS}} = APS(S) - APS(M) \tag{4.13}$$

Finally, the APS removal from the M interferograms is performed using the following complex product:

$$\phi^{k}_{APS\_free} = \arg\left(\phi_k \cdot \phi^{*}_{APS_k}\right) \tag{4.14}$$

Where k refers to the k^{th} interferogram.

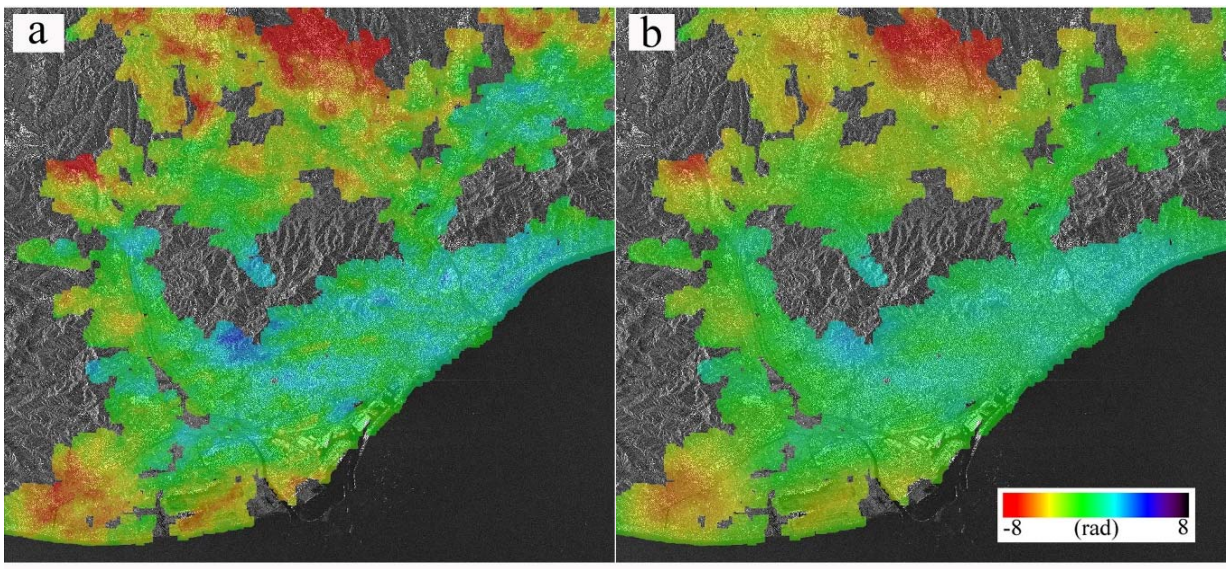

Figure 4.6. Example of estimated Atmosphere Phase Screen (APS) candidate map using low pass filter cut-off (CO) 30, i.e. about 1,7 km of spatial wavelength (a) and CO 6 , i.e. about 8 km of spatial wavelength (b). The APS analysed were derived from a stack of 28 StripMap TerraSAR-X images over Barcelona.

4.3. Third processing block: deformation estimation

In this step, the deformation maps and time series are derived. The procedure starts with a set of M APS-free interferograms and a set of selected CPSs. The procedure is explained in next two sections.

4.3.1. 2+1D phase unwrapping

In this final step, a 2+1D phase unwrapping is performed over a dense set of PSs on the M APS- and RTE-free interferograms. The RTE needs to be estimated and removed from the M APS-free interferograms to avoid errors in the 2D phase unwrapping. The RTE is estimated during the densification procedure explained in Section 3.2.3. In this step, the first order network is given by the selected CPSs, while the second order candidate PSs are selected using the DA criterion. When processing wide areas, the area of interest is usually subdivided in overlapping subsets. The different subsets are then combined during the integration step (see Section 3.2): the overlapping points of the i^{th} and $(i+1)^{th}$ subsets are used as reference points to the $(i+1)^{th}$ subset, so the estimations are relative to the same reference point. The parameters selected to derive the estimations, i.e. the DA threshold to select the candidate PSs and the γ_e threshold to select the edges of the second order network, could be different in each subset depending on the characteristics of the subset, e.g. urban or non-urban areas. It is important to take into account that no reliable APS estimations exist over areas where no CPSs were selected; thus, the densification in those areas must be checked thoroughly. Finally, it is worth noting that the linear model is only used to select the second order PS network and derive the RTE estimates: the 2+1D phase unwrapping does not make use of any a-priori defined deformation model.

The ϕ_{RTE}^{k} is computed from the estimated RTEs for each k^{th} interferogram over the second order PS network:

$$\phi_{RTE}^{k} = \frac{4\pi}{\lambda}\frac{B_{\perp}^{k}}{R^{k}\text{sen}\theta^{k}}\,RTE \tag{4.15}$$

Then, it is subtracted from the corresponding interferogram. Optionally, the thermal dilation and the velocity of deformation can also be removed.

A spatial 2D phase unwrapping is then performed separately on each interferogram using the Minimum Cost Flow method (Costantini, 1998; Costantini et al., 1999). The 2D phase unwrapping is an error-prone step, especially for isolated pixels, high phase gradient between pixels, and when the atmosphere or the noise components are high. A 1D phase unwrapping, whose goal is the detection and correction of the errors generated in the 2D phase unwrapping stage, is performed. For this purpose, it uses an iterative LS procedure (Baarda, 1968; Förstner, 1986; Björck, 1996), which fully exploits the integer nature of the unwrapping errors. As explained in Section 4.1.2, the 1D phase unwrapping involves a pixel wise procedure over the temporal dimension. It is based on the estimation of the following system of equations:

$$\Delta\phi_{MS} = \tilde{\phi}_{S} - \tilde{\phi}_{M} \tag{4.16}$$

$$\tilde{\phi}_{0} = 0 \tag{4.17}$$

The system is solved by means of an iterative LS driven by two key parameters: the residuals $\hat{\phi}_{res}$ and the redundancy of the network. It is important to consider the number of interferograms that are directly tied to each image, i.e. the number of interferograms where a given image appears either as master or slave. The main steps of the 1D phase unwrapping algorithm include:

1. Performing the first LS estimation and computing the residuals.

2. Temporally removing the highest absolute residual (outlier candidate) from the network, and performing a new LS estimation.
3. Checking the residual of the outlier candidate: if it is a multiple of 2π (within a given tolerance), the observation is corrected and reaccepted. In this way, it is possible to correct the unwrapping errors. Otherwise, the decision of re-entering or rejecting the outlier candidate is based on the comparison of its old and new residuals.
4. Performing a new LS estimation, computing the residuals and restarting the procedure from step (2). The procedure is executed iteratively from (2) to (4) until there are no remaining outlier candidates, i.e. there is no residual above a given threshold. Then, the correction of the unwrapping-related errors is extended to all the residuals that, within a given tolerance, are multiple of 2π.

The core of the proposed algorithm is given by the so-called redundancy matrix R. As the LS is not a robust estimation method, considering that a given error might be spread out through the network according to the characteristics of A and P, it is necessary to analyse how the errors are distributed in the network in order to identify correctly the residuals that are multiple of 2π. This information is contained in the redundancy matrix R (Förstner, 1986):

$$R = I - A \cdot (A^T \cdot P \cdot A)^{-1} \cdot A^T \cdot P \tag{4.18}$$

R is only related to A and P, i.e. it is not affected by the observation vector. This matrix is used to correct the LS residuals using the redundancy of the corresponding observations:

$$\hat{\phi}^*_{res\_i} = \frac{\hat{\phi}_{res\_i}}{r_{ii}} \tag{4.19}$$

where $\hat{\phi}^*_{res\_i}$ is the corrected i^{th} residual and r_{ii} is the i^{th} diagonal element of R, which is called the local redundancy. The procedure to correct the unwrapping errors explained above is performed on the corrected residuals. If the redundancy of the system is adequate, the unwrapping errors are properly identified. However, it is worth emphasising that this requires that the majority of the interferograms connected to a given image are correctly unwrapped. The algorithm checks the available local redundancy at each iteration and leaves a given outlier candidate untouched if its redundancy is too low. If this occurs, the corresponding parts of the network have to be checked off-line after the automatic analysis has concluded. That is, the 1D phase unwrapping only works over the redundant parts of the analysed network.

4.3.2. Description of the outputs

The main outputs of this step are the deformation TS of each PS and the accumulated deformation maps. Furthermore, additional outputs are used to check the quality of the final results, including the plot of the residuals at the 1st and last LS iterations.

The plot at the 1st iteration illustrates the distributions of phase unwrapping errors, both interferogram wise and PS wise. It is worth to note that this plot contains the same information used in the phase unwrapping consistency check to select the CPSs (see Section 4.1.2). The residuals at the last iteration allow the detection of problematic interferograms and noisy or bad unwrapped points when they differ from zero (i.e. when there are phase unwrapping errors that have not been corrected). Figure 4.7 illustrates an example of residual plots. The upper figure shows the residuals at the 1st iteration, where all PS residuals (rows) show a similar pattern with respect to the interferograms (columns). The middle plot shows the residuals at the last iteration. In this case, all the phase unwrapping errors have been resolved ($\hat{\phi}_{res} = \vec{0}$), except one (black line).

This interferogram was then discarded from the network and the 1D phase unwrapping was performed again. Moreover, the residuals can be analysed PS wise. The bottom plot of Figure 4.7 shows the residual profile of a PS in the 1st iteration (in blue) and in the final iteration (in purple), where all the phase unwrapping errors have been corrected ($\hat{\phi}_{res} = \vec{0}$), except for the problematic interferogram.

Another important output is a 3-class quality index associated with each deformation time series. Three classes are defined, "Good", "Fair" and "Warning", which are derived, per each image of a given time series, by computing the ratio (Cor_%) between the corrections and the interferograms connected with the image at hand. The following classes are used: "Good" indicates that Cor_% is less than 30% for all the images; "Fair" is when Cor_% is between 30 and 40%; and "Warning" is when the Cor_% of at least one image is above 40%.

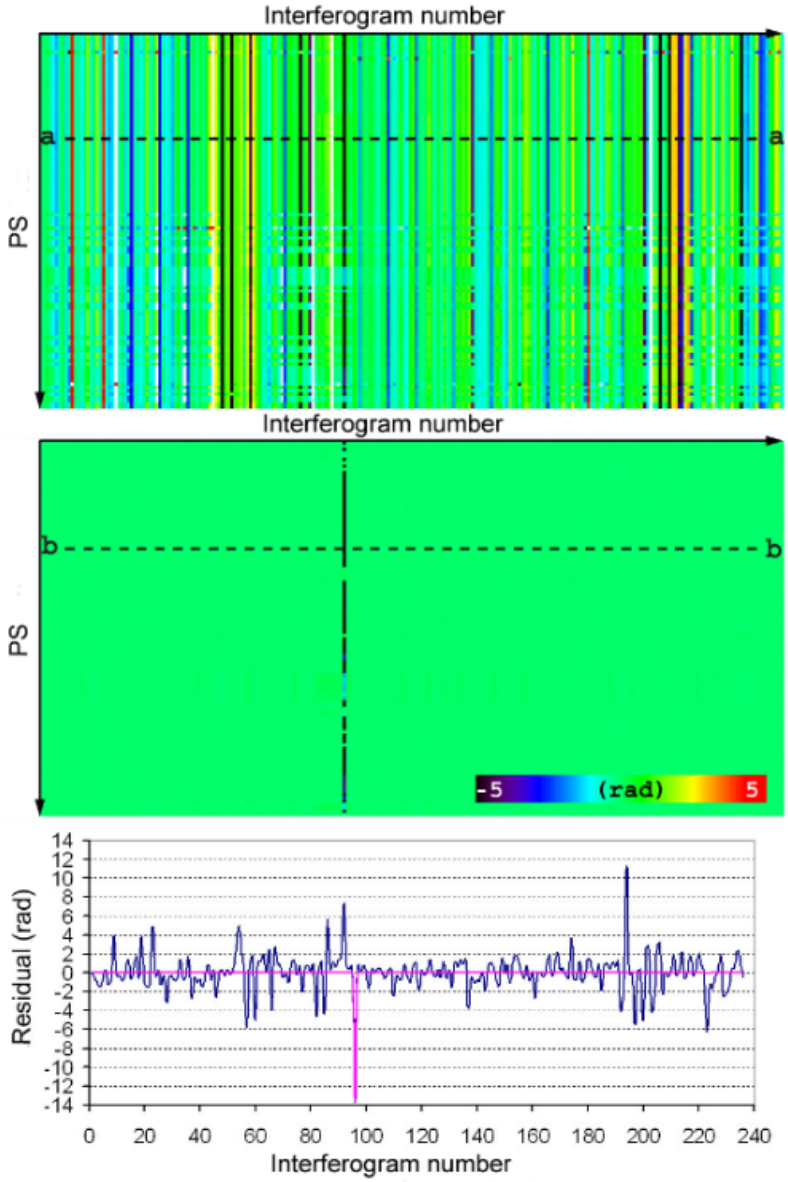

Figure 4.7. Example of plots of Least Square (LS) residuals at the 1st (top) and final (middle) iterations. The plot shown at the bottom is a profile along a-a (in blue) and b-b (in purple). This example was derived from a dataset of 236 interferograms.

In addition to the quality index, the corrections per image are obtained for each time series. This is the most complete information that can be used to assess the quality of each image of a given time series. Some examples are shown in Figure 4.8. In this case, the 1D phase unwrapping was performed using a network of 28 images and 27 interferograms per each image. Figure 4.8 (top) shows two examples of "Good" time series, where no corrections were applied during the 1D phase unwrapping. One time series shows a stable PS, while the other one displays a displacement away from the sensor. Figure 4.8 (middle) shows two "Fair" time series, while Figure 4.8 (bottom) shows two time series classified as "Warning". The last two time series show aliasing. On the left side, the aliasing occurs between the 15th and 16th images and affects half of the time series, while on the right side the corrections basically affect two images (the 16th and 17th) and the aliasing is only localized in one image. It is worth noting that the aliasing does not occur in every "Warning" time series. This last example illustrates how the corrections are useful to discriminate between the most reliable and problematic images within a given time series.

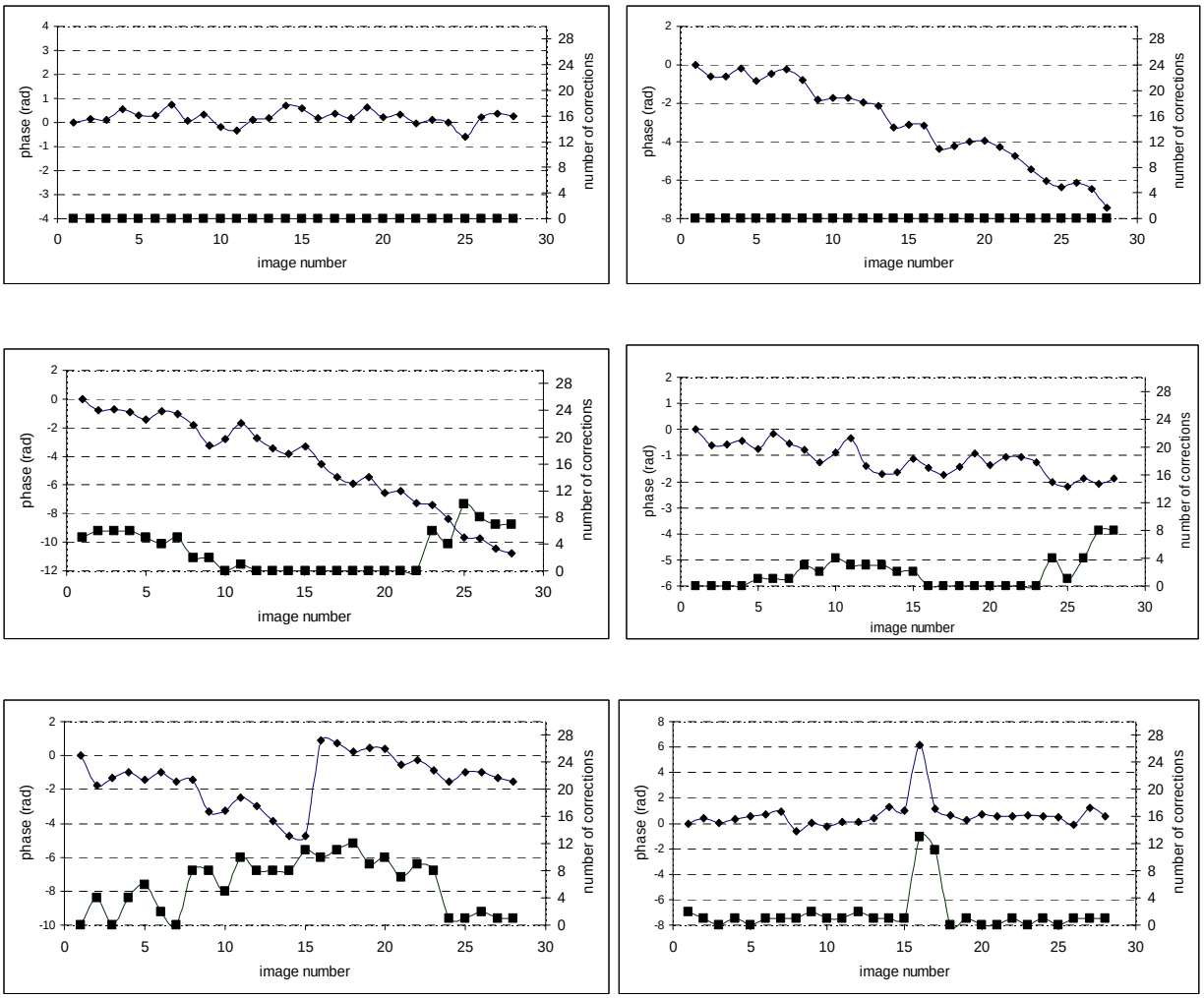

Figure 4.8. Examples of time series (diamonds) and the associated corrections per each image (squares). "Good" time series (top), "Fair" time series (middle) and "Warning" time series (bottom) are shown. These examples were derived from the Barcelona dataset with a redundant network of 28 images and 27 interferograms per image.

Chapter 5

PSIG results using X-band data

The results of the PSIG procedure proposed in Chapter 4 are illustrated and discussed in this chapter. The results are presented and analysed step by step. The CPS selections performed with different sensors and datasets are discussed and compared in the first section. In section 5.2, the strengths and limitations of the CPS selection procedure are discussed and compared with the alternative classical two-parameter method. The third section describes the 28 APS images generated from the 28 TerraSAR-X StripMap images over the Barcelona test site, analysing some examples of APS filtered interferograms. The dense network of PSs and the linear velocity and RTE maps are presented in section 5.4. The final outputs including the accumulated deformation map, the time series and the associated quality index are discussed in section 5.5.

5.1. CPS selection using two X-band datasets

This section presents the results in three sub-sections, beginning with the selection of the seeds, followed by the analysis of the obtained candidate CPSs and ending with the discussion of the selected CPSs.

5.1.1. Seed selection

The first step to obtain the CPS network is the selection of the seeds. This selection needs to be carefully performed; otherwise the candidate CPSs will not fulfil the phase unwrapping requirements. The MA and DA images are used to select points located on the ground and displaying low noise, typically DA values below 0.1 are chosen. The seeds are usually selected on roads or flat infrastructures, as in the example of the Barcelona airport (Figure 5.1a), which was based on a stack of 28 StripMap TerraSAR-X images, and another example over a road in Miami (Figure 5.1b), which was derived using a stack of 30 Spotlight TerraSAR-X images.

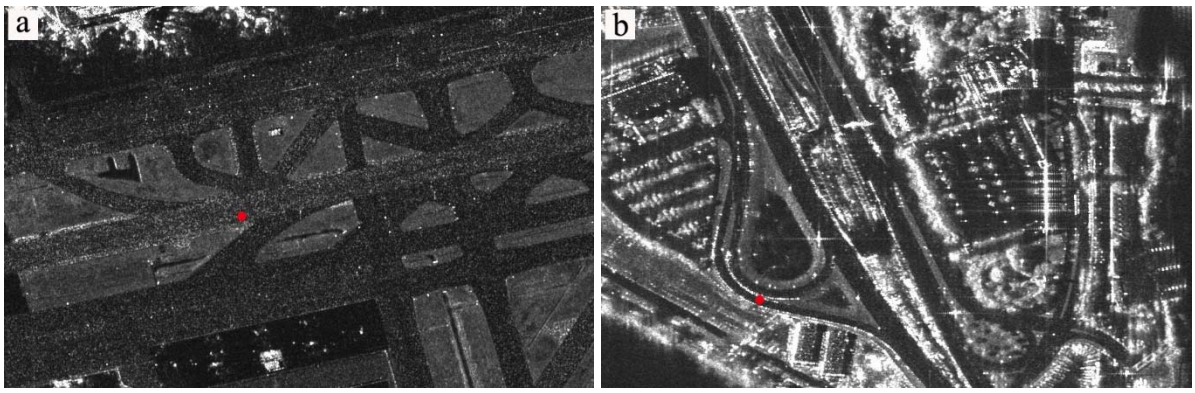

Figure 5.1. Example of CPS seed (in red) over selected in a runway of the Barcelona airport (a). Example of CPS seed (in red) located on a road in Miami (b). In both cases, the seeds have DA values below 0.1 and are located on the ground.

Note that it is more difficult to find appropriate seeds in urban areas, where the points with low DA are usually located on buildings or other structures with some height above the ground. However, once a seed is selected, the propagation is usually straightforward. Special care must be taken to avoid selecting seeds in deformation areas. This aspect might require an iterative approach because the deformation areas are usually not known prior to the PSI analysis. Some seeds may not propagate; in such cases the seeds are discarded and replaced. In the example of the Barcelona dataset, nine seeds distributed over the frame were used (red points in Figure 5.2a), with an approximate density of one seed per 100 km^2. Four seeds were needed to connect the entire basin of the Llobregat River, while the city of Barcelona was spatially covered with just one seed. Note that the urban areas are connected through highways and roads (see examples in Figure 5.3).

5.1.2. Candidate CPSs

In the Barcelona dataset, 611813 candidate CPSs were found in an area of 1019 km^2, with a mean density of 600 candidate CPS/km^2 (Figure 5.2a). Figure 5.2b displays the candidate CPSs selected in Seattle (USA), which were computed using a stack of 30 CosmoSkyMed images. In this case, five seeds (red points in Figure 5.2b) were required to cover an area of 365 km^2 and 34594 candidate CPSs were selected, corresponding to a density of 95 candidate CPS/km^2. The remarkably reduced density of the Seattle dataset is caused by the wide perpendicular baseline distribution, [-800; 600 m], with respect to the distribution of the Barcelona dataset: [-170, 150 m]. Note that large baseline distributions provide more sensitivity to topography and, as a consequence, the candidate CPSs have limited height values. In such cases, the candidate CPS selection can be used to select points with a given RTE. It is worth noting that the lower density of the Seattle dataset does not mean a poor performance of the method. In fact, the candidate CPSs are homogeneously distributed over the area of interest and the density is adequate for the purpose of the APS estimation.

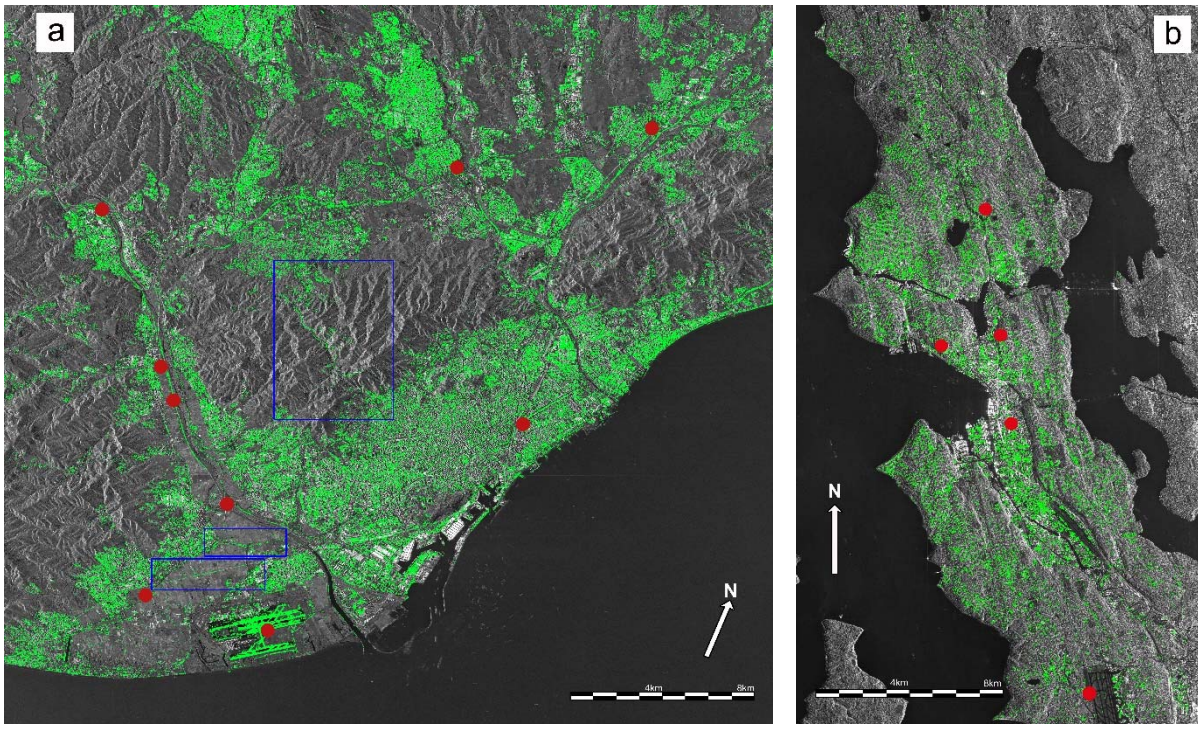

Figure 5.2. Candidate CPS coverage (green points) and seed locations (red points). 611813 candidate CPSs were selected from nine seeds in the Bacelona dataset (a). 34594 candidate CPSs were selected from five seeds in the Seattle dataset (b).

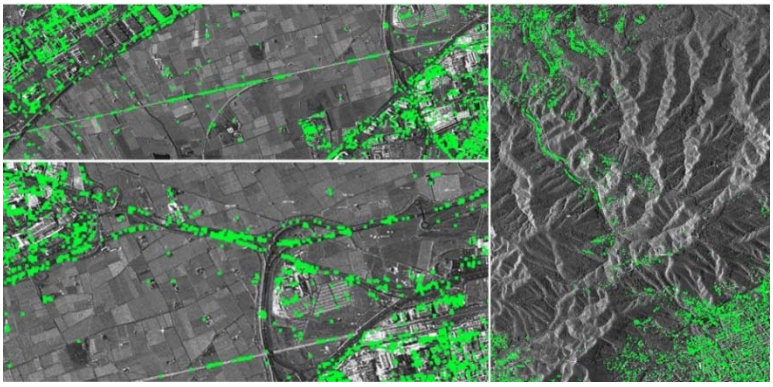

Figure 5.3. Distribution of candidate CPSs in three areas of the Barcelona datasets. The three subsets correspond to the blue squares shown in Figure 5.2a.

5.1.3. Selected CPSs

In the Barcelona dataset, 87% of the candidate CPSs satisfied the filter from Equation 4.8 and became selected CPSs, and in the Seattle dataset 82% of the candidate CPSs were selected. The distribution of the CPSs is displayed in Figure 5.4. The phase unwrapping errors, i.e. $\hat{\phi}_{res} \neq \vec{0}$, in the Barcelona dataset (see Figure 5.4a) generally occur in rather isolated and peripheral areas. In such areas, these errors are mainly caused by strong APS signals and can be usually reduced by increasing the candidate CPS density. In some cases, the rejected candidate CPSs are located in areas with strong deformation. This is illustrated in Figure 5.5a, where the rejected candidate CPSs mainly correspond to deformations close to the new terminal T1 displaying velocities higher than 10 mm/year (Figure 5.5b). Some unexpected clusters of rejected candidates (Figure 5.5c) were found in downtown Barcelona, which after an analysis, happened to be points with RTE above 10 m, as shown in Figure 5.5d. This effect is probably caused by an error in the CPS selection algorithm: in fact, CPSs with heights above 10 m should be automatically discharged, while in this specific case this did not occur.

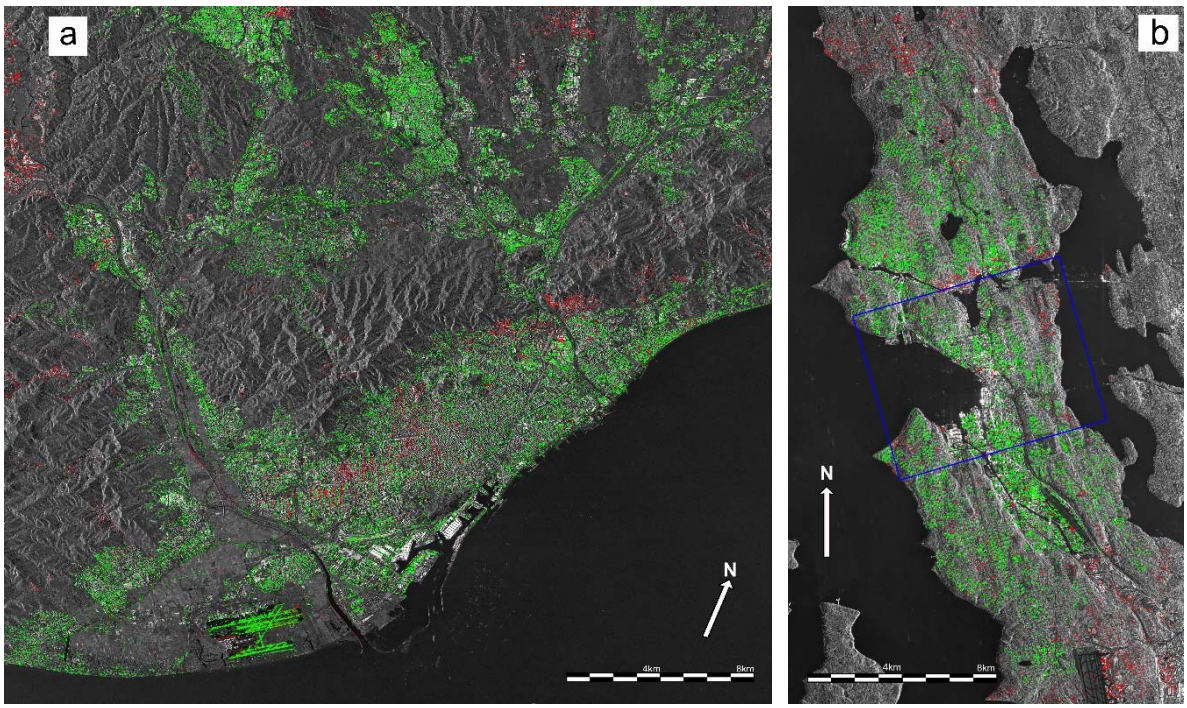

Figure 5.4. Distribution of the selected (green points) and rejected (red points) CPSs in the Barcelona (a) and Seattle (b) datasets.

Figure 5.4b illustrates the distribution of selected (in green) and rejected (in red) CPSs in the Seattle dataset. The rejected CPSs are mainly located in the upper and bottom peripheral areas and the cause of the rejection is probably the APS effects.

The maximum RTE of the selected CPSs of the Barcelona dataset is 13 m and all the candidate CPSs with higher RTE, being 25 m the maximum, were discarded with the $\hat{\phi}_{res} = \vec{0}$ criterion. The RTE distribution of the selected CPSs is as follows: 70% have RTE lower than 2 m, 25% have RTE between 2 and 4 m, and 4% between 4 and 6 m, while the remaining 1% corresponds to points with a RTE higher than 6 m. These numbers are in agreement with the 2 m of theoretical maximum ΔRTE allowed, for the Barcelona interferogram networks, between a seed and a candidate CPS (see Section 4.1.3 and Figure 4.2a). Finally, 98.2% of the CPSs have absolute deformation velocity smaller than 2 mm/year, 1.7% between 2 and 4 mm/year and the remaining 0.1% display velocities higher than 4 mm/year.

The RTE values of the candidate CPSs of the Seattle dataset are lower than those of the Barcelona dataset. The analysis of the CPS, which was only performed in the city of Seattle (blue square in Figure 5.4b), produced these values: 72% of the CPSs have RTE lower than 2 m, 15.5% have RTE between 2 m and 4 m, 11% between 4 m and 6 m, and 1.5% have RTE higher than 6 m. The maximum theoretical ΔRTE for this dataset is approximately 1 m. A test was performed on the studied subset to obtain points located on the ground: using Thr = 0.7 rad all candidate CPSs obtained were located on the ground, with heights below 2 m.

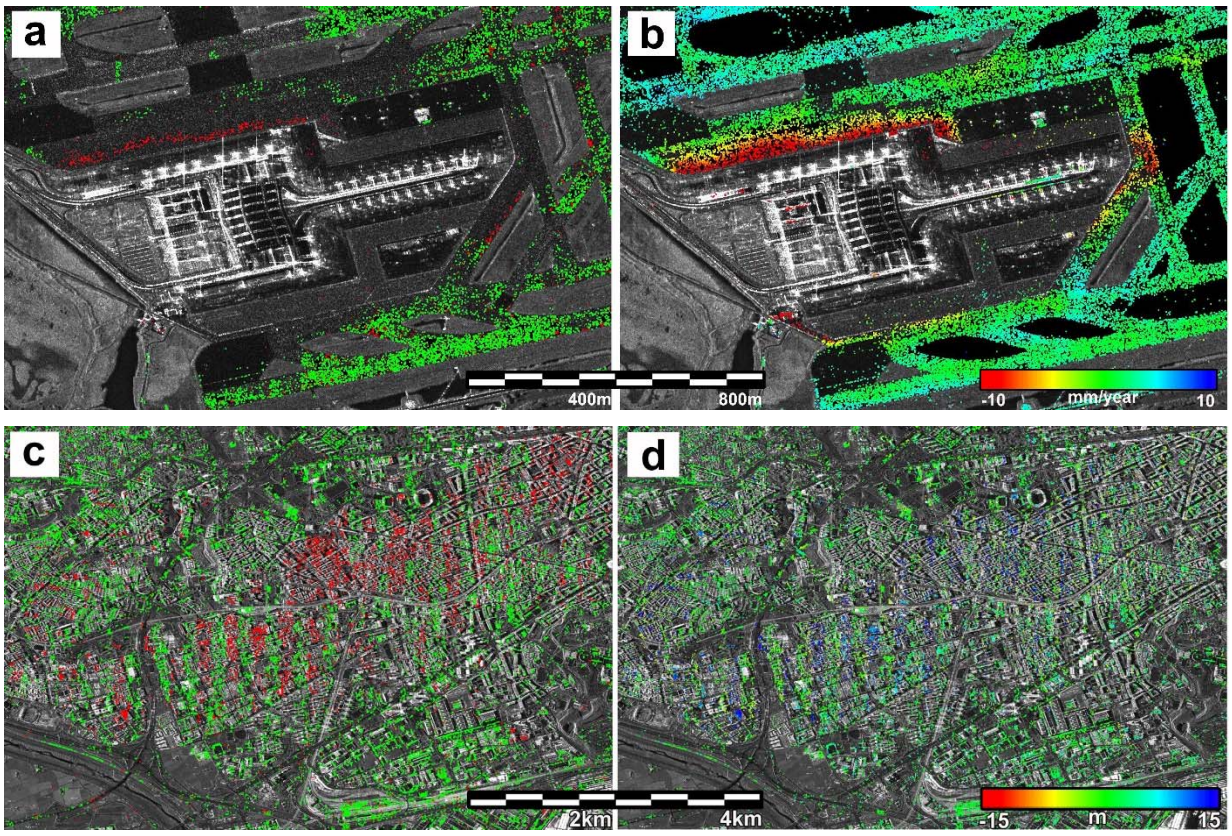

Figure 5.5. Distribution of the selected (green points) and rejected (red points) CPSs in the Barcelona airport (a), and corresponding deformation velocity map (b). Distribution of selected (green points) and rejected (red points) CPSs in the centre of Barcelona (c), and corresponding RTE map (d).

5.2. CPS selection versus the two-parameter model

An alternative method to the CPS selection consists in applying the two-parameter model described in Chapter 3. The two-parameter model produces the integrated linear velocity and RTE over the processed area. These two components are then removed from the M interferograms and the remaining components of the interferograms are caused by the APS, the remaining non-linear deformations and the noise. As a consequence, the phase unwrapping can be correctly performed because the high interferometric phase variations, which are caused by deformation and RTE, are removed.

This approach requires connecting all PSs with a unique network of edges, which is a critical step for wide area processing, where there can be big extensions of non-urban areas, i.e. large areas with very low PS density. The CPS selection is more straightforward and flexible compared to the two-parameter model because it makes use of a set of non-connected CPS networks (nine networks were generated from the same number of seeds in the Barcelona dataset). Moreover, the proposed procedure is computationally lighter than that based on the two-parameter model. In addition, and more importantly, it includes tools to check the consistency and hence the quality of the phase unwrapping.

An additional advantage of the CPS selection is that the v and RTE estimated with the two-parameter model can be severely affected by the atmospheric effects, which are particularly strong in the X-band data (see Figure 5.6). By contrast, this does not occur with the candidate CPS selection. Considering the number of selected points, the CPS selection is urban areas is more restrictive than the two-parameter model, thus yielding less dense CPS datasets. However, in the author's experience, a reduced CPS density does not prevent a correct phase unwrapping, which is the main goal of the CPS selection.

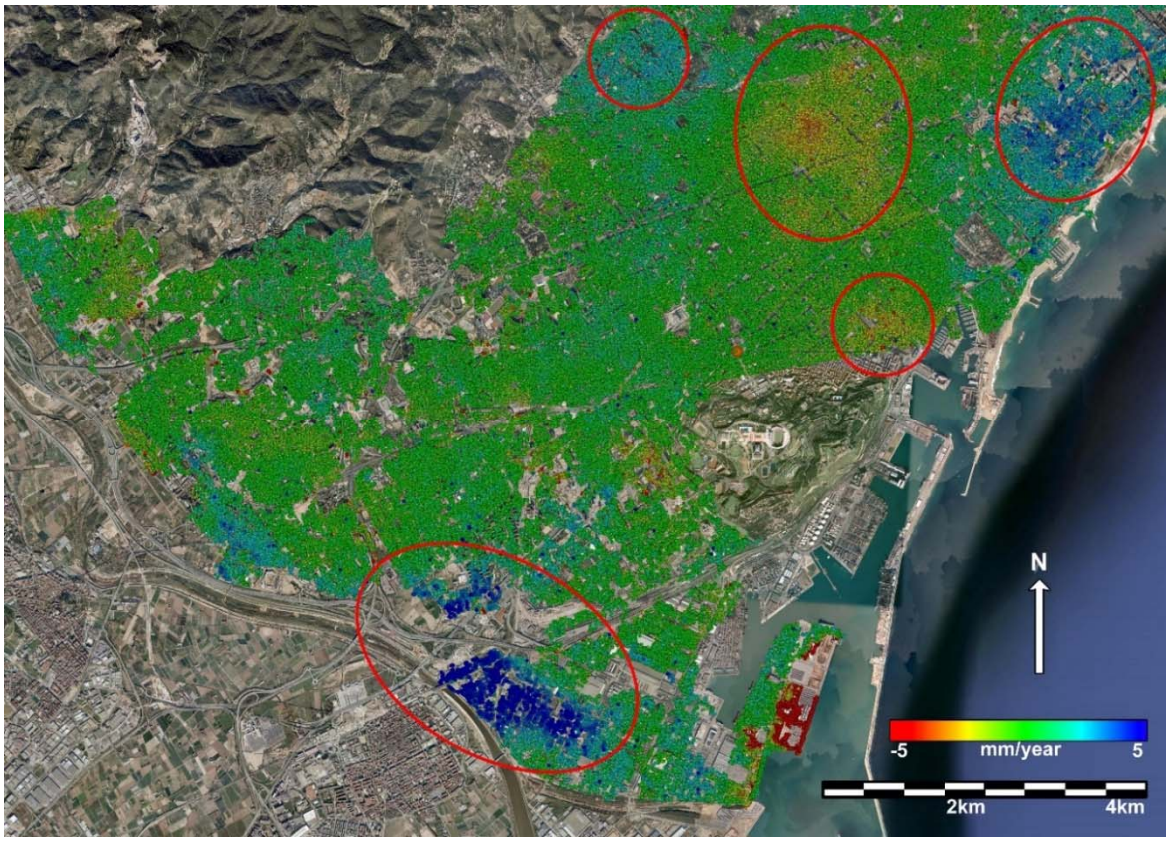

Figure 5.6. Deformation velocity map obtained with the two-parameter model using a set of 51 interferograms. The results are highly affected by residual atmospheric effects (highlighted in red).

5.3. APS estimation

This section describes the APS estimation for the Barcelona dataset, which is composed of 28 TerraSAR-X StripMap images. The APS was estimated using only a LPF. The subsequent temporal high pass filter was not required because the selected CPSs are basically stable points, displaying no deformation. Note that this is one of the key advantages of the CPS selection procedure proposed in this work and described in Chapter 4.2.1. The major components of the interferometric phase are therefore due to the RTE and the APS and these two components can be separated using a simple LPF. Moreover, the RTE generally displays small values, e.g. in the specific case of the Barcelona dataset, only the 5% of the CPSs have RTE higher than 4 m.

The 28 APSs of the Barcelona dataset were estimated using a Butterworth LPF, with a CO of 42. The filter was performed using a multi-look of 20 by 20 pixels in range and azimuth. The 28 estimated APSs are shown in Figure 5.7. Note that the APS corresponding to the first image equals zero because the estimations are relative to this first image, whose phase is set to zero. The APS values are estimated at the CPS locations, and interpolated over the areas that are not covered by CPSs. This aspect needs to be considered in the analysis of the APS results.

The APS patterns vary from one image to another. Some effects are concentrated in a few square kilometres, as the APS of the image acquired the 10/01/2008 (Figure 5.7), while other images display much more extended effects, up to hundreds of square kilometres, e.g. see the APS images acquired the 17/08/2008 and 22/11/2009. In general, the strongest APS effects are found in the acquisitions made in summer and, particularly in August when strong APS phase variations occur. An example can be seen at the bottom left corner of the image acquired the 17/08/2008. By contrast, the APS effects are usually smoother during the winter months, reaching a maximum variation of about 3 rad, e.g. see the images acquired the 21/01/2008 and 29/01/2009.

Note that some images show a strong linear term variation, e.g. the image acquired the 15/08/2009, with phase differences of up to 25 rad. These effects are usually caused by errors in the orbits used in the PSI processing. In such cases, the linear phase term is estimated and removed before the LPF is performed.

The 28 APSs images were used to simulate and remove the APS component from the original 373 differential interferograms. Figure 5.8 shows two examples of original and APS filtered interferograms. Figure 5.8a is an interferogram with master image of 23/02/2008 and slave image of 22/11/2009, with a perpendicular baseline of 6 m. Different APS effects are visible over the entire scene. These effects disappear in the corresponding APS-free interferogram (Figure 5.8b). However, local phase variations are noticeable at the right-upper corner of the APS-free interferogram. In this case, they are caused by some deformation phenomena.

The second example concerns an interferogram with master image acquired the 29/04/2008 and slave image of 21/05/2008, with perpendicular baseline of 228 m (Figure 5.8c). No significant deformations are expected due to the relatively small time interval between acquisitions. The atmospheric artefacts are in general lower than in the previous example. However, there are some artefacts, e.g. in the airport and the centre of Barcelona, that are correctly filtered and are not visible in the APS-free interferogram (Figure 5.8d).

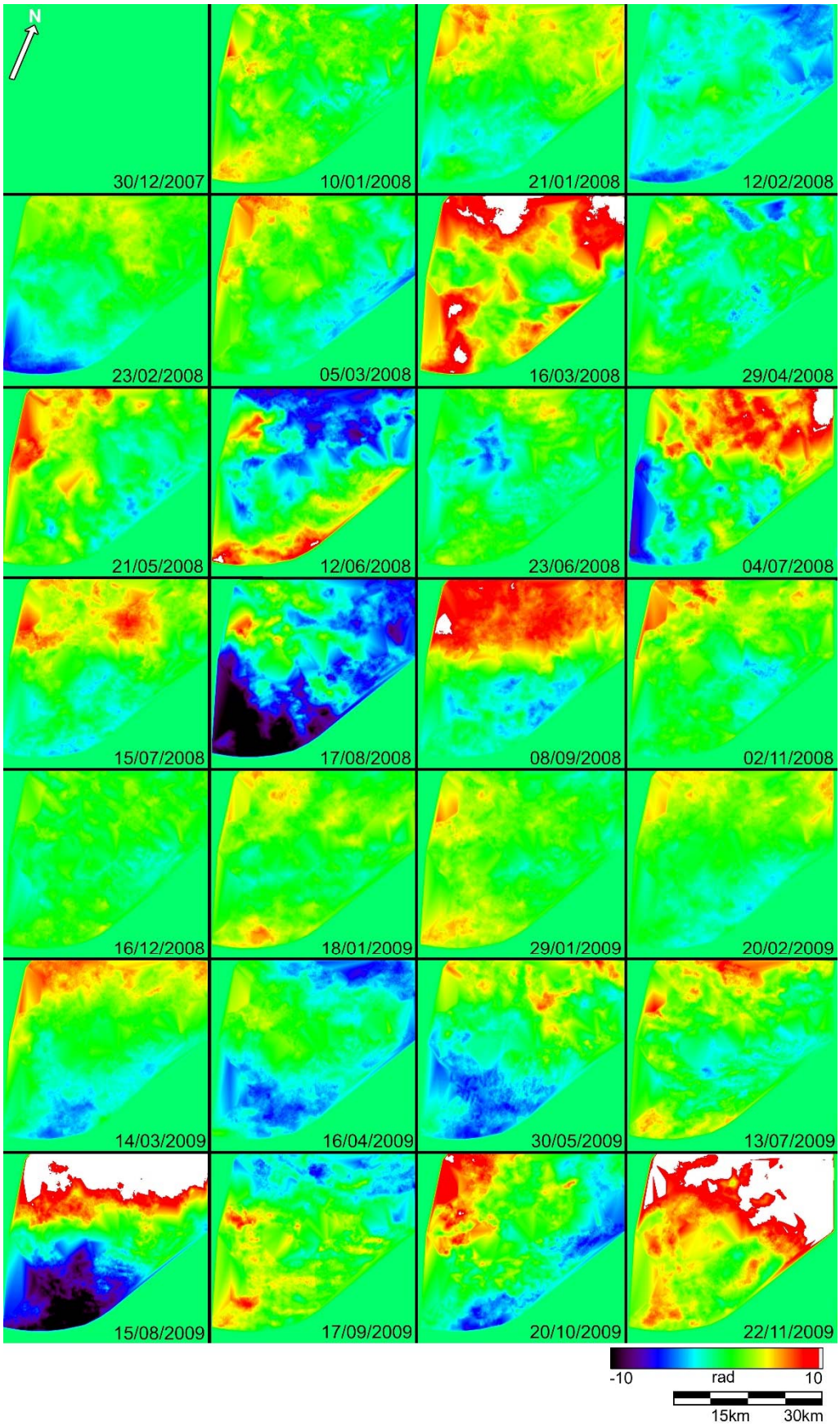

Figure 5.7. 28 APSs estimated from a stack of 28 TerraSAR-X StripMap images of the Barcelona test site. The date (dd/mm/yyyy) is indicated in each image. These APS were computed using a Butterworth low pass filter with cut-off frequency of 42.

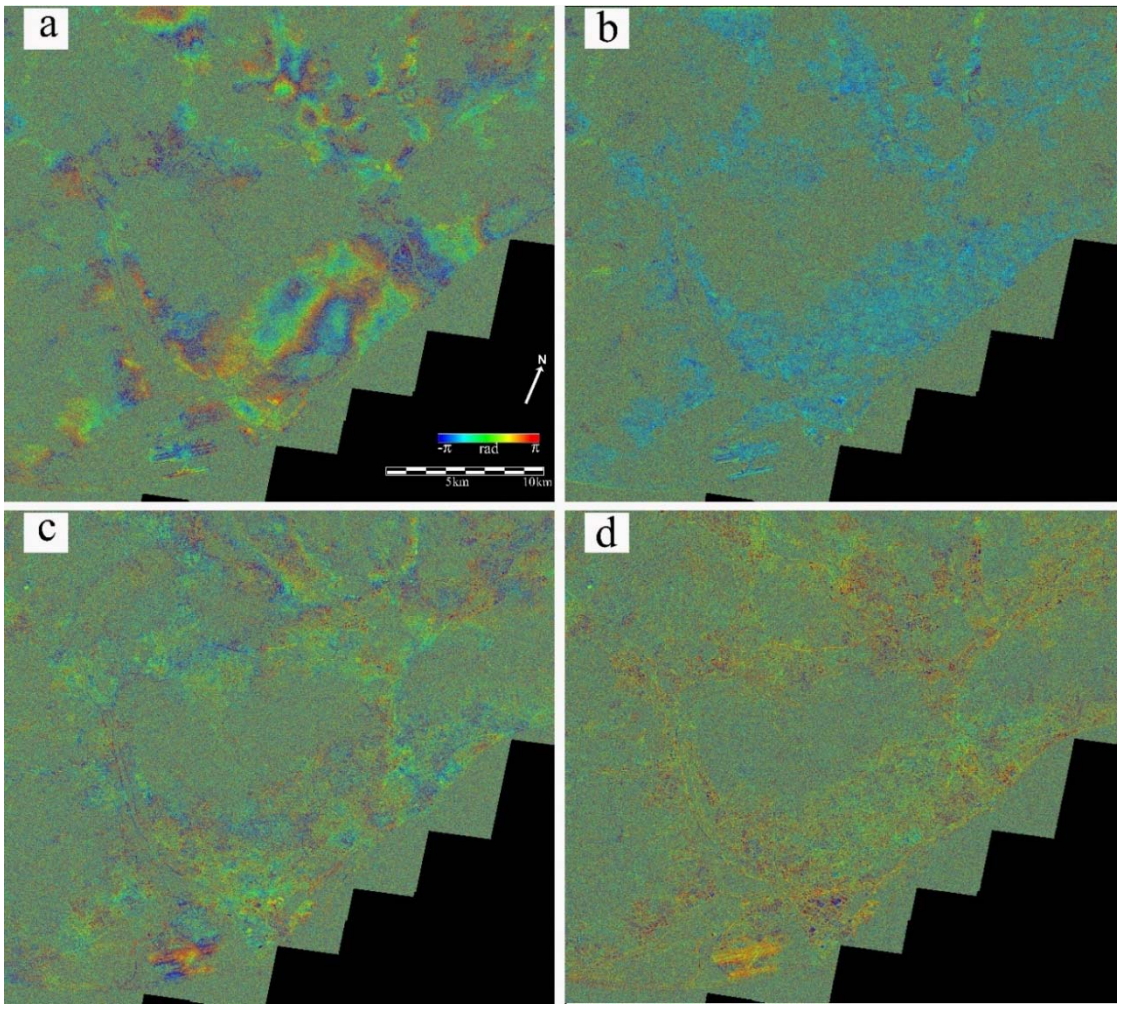

Figure 5.8. Interferogram composed by the images acquired the 23/02/2008 and 22/11/2009, with 6-m perpendicular baseline: original (a) and APS filtered (b). Interferogram composed by the images acquired the 29/04/2008 and 21/05/2008, with 228-m perpendicular baseline: original (c) and APS filtered (d).

5.4. Deformation velocity over the final set of PSs

In this section, the lineal velocity map created with the final set of PSs selected for the full scene of the Barcelona dataset is described. This map was generated using the classical two-parameter model (see Section 4.3). In order to process the big amount of data, the Barcelona full scene was divided in 17 subsets of approximately 5000 by 5000 pixels, with an overlapping area of 200 pixels used to integrate all the subsets in a unique solution. The reference area was located in the airport runways; the deformation and RTE values are relative to this point. The deformation velocity map, shown in Figure 5.9, comprises more than 5.4 million PSs and covers 1019 km^2. Only the major deformation phenomena, as those found in the airport and the port of Barcelona and other subsidence and uplift areas located at the upper right part of the image, are clearly visible in this image. However, more than thirty major deformation phenomena were found over the entire scene; some examples of deformation maps are shown in the Appendix. Although not all of them have been analysed yet, there are several examples of deformation caused by soil compaction, water abstraction, landslides, underground construction works (underground lines and stations), etc. These results represent a valuable source of information for the public and private entities in charge of the maintenance of indispensable assets of the Barcelona metropolitan area. Note that this map was obtained using the linear model of the deformation. The model-free deformation map is presented later in this chapter.

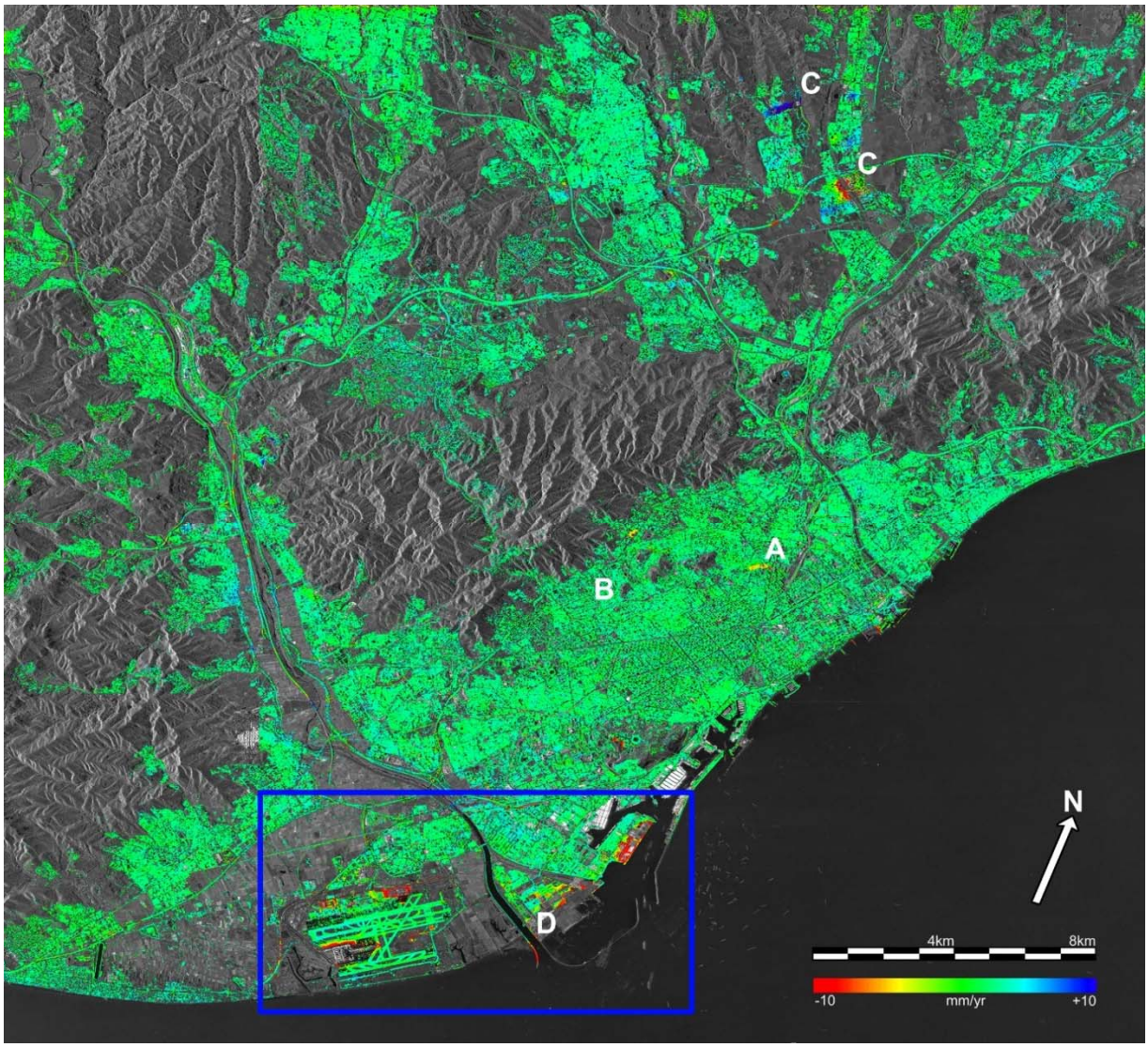

Figure 5.9. Deformation velocity map of the Barcelona dataset, which comprises more than 5.4 million PSs and encompasses 1019 km^2.

5.5. 2+1D phase unwrapping and final outputs

The results of the last step of the procedure over the full scene of the Barcelona dataset are presented in this section. The 2+1D phase unwrapping was performed over 373 interferograms generated from a stack of 28 images spanning the period 2007-2009. The 373 interferograms, RTE- and APS-free, were spatially unwrapped using the Minimum Cost Flow method. The model-free accumulated deformation, the PS time series and a quality index of the estimations were derived with the temporal 1D phase unwrapping. The 5.4 million PSs selected in the densification were analysed point by point.

Over 2014 million observations were analysed in the 1D phase unwrapping, i.e. 373 observations per each PS multiplied by the total number of analysed PSs (5.4 millions). 81.6% of the observation residuals were approximately equal to zero in the first iteration, while the remaining 18.4% of the observations were affected, to some extent, by phase unwrapping errors. This includes both the observations directly and indirectly affected by outliers (multiple of 2π).

98.4% of the analysed PSs have a “Good” quality index, 1.2% have a “Fair” quality index, and 0.38% have a “Warning” quality index at the last iteration of the 1D phase unwrapping.

Figure 5.10 shows four examples of TSs, all of them classified as "Good", related to different types of deformations (see the location A-D in Figure 5.9). Specifically, the TS (A) is related to an area affected by the construction of a new underground line. During the first six months the displacements are small (2 mm), with the majority of the displacement (14 mm) occurring within one year, and the area is stable during the last 5 months. This type of data is useful to obtain a synoptic view of the temporal evolution of the deformation in the area affected by underground works. The TS (B) displays the deformation induced by the construction of two buildings in the vicinity. This is an interesting application, especially for city municipalities. The third example (C) concerns two case studies: a subsidence caused by water abstraction and an uplift probably related to the cease of water pumping. Again, this represents a valuable source of information for the agencies in charge of water resource management. Finally, the fourth example (D) shows the thermal dilation of a PS located at the top of an industrial building. In this case, a very high correlation between displacement and temperature is perceptible.

Figure 5.11 shows a zoom of Figure 5.9 over the airport and port of Barcelona, where several structures and infrastructures affected by deformation phenomena are visible. The quality index map of the same area, which is useful to obtain a preliminary and concise overview of the quality of the estimated PSs, is displayed in the same figure. Most of the area is green, i.e., most of the PSs are classified as "Good". The PSs in yellow (labelled as "Fair") and red (labelled as "Warning") are in some cases clustered over deformation and isolated (i.e., not well connected) areas, where the phase unwrapping is more error-prone. The rest of yellow and red points are scattered over the stable area, e.g. airport runways, and are probably local, noisy PSs.

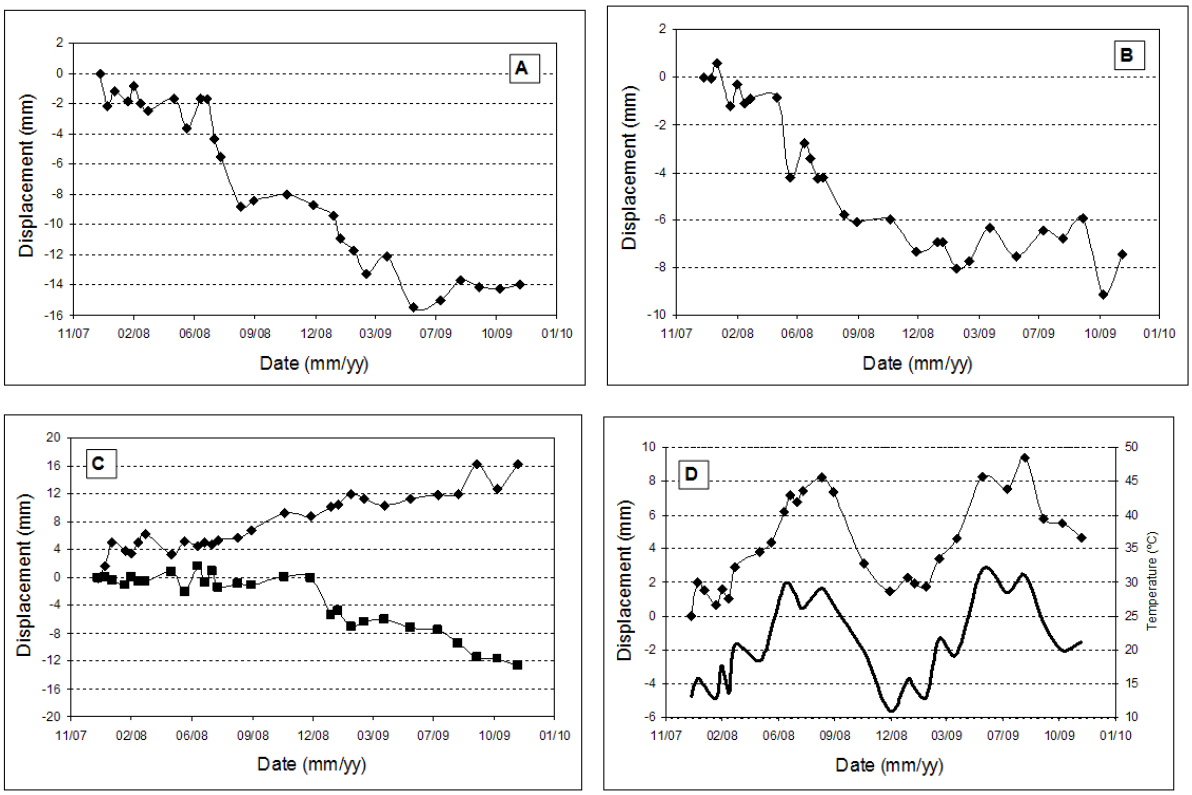

Figure 5.10. Examples of deformation time series from the Barcelona dataset. The location of the corresponding Persistent Scatterers (A-D) is shown in Figure 5.9. The black line in bold shown in (D) displays the temperature.

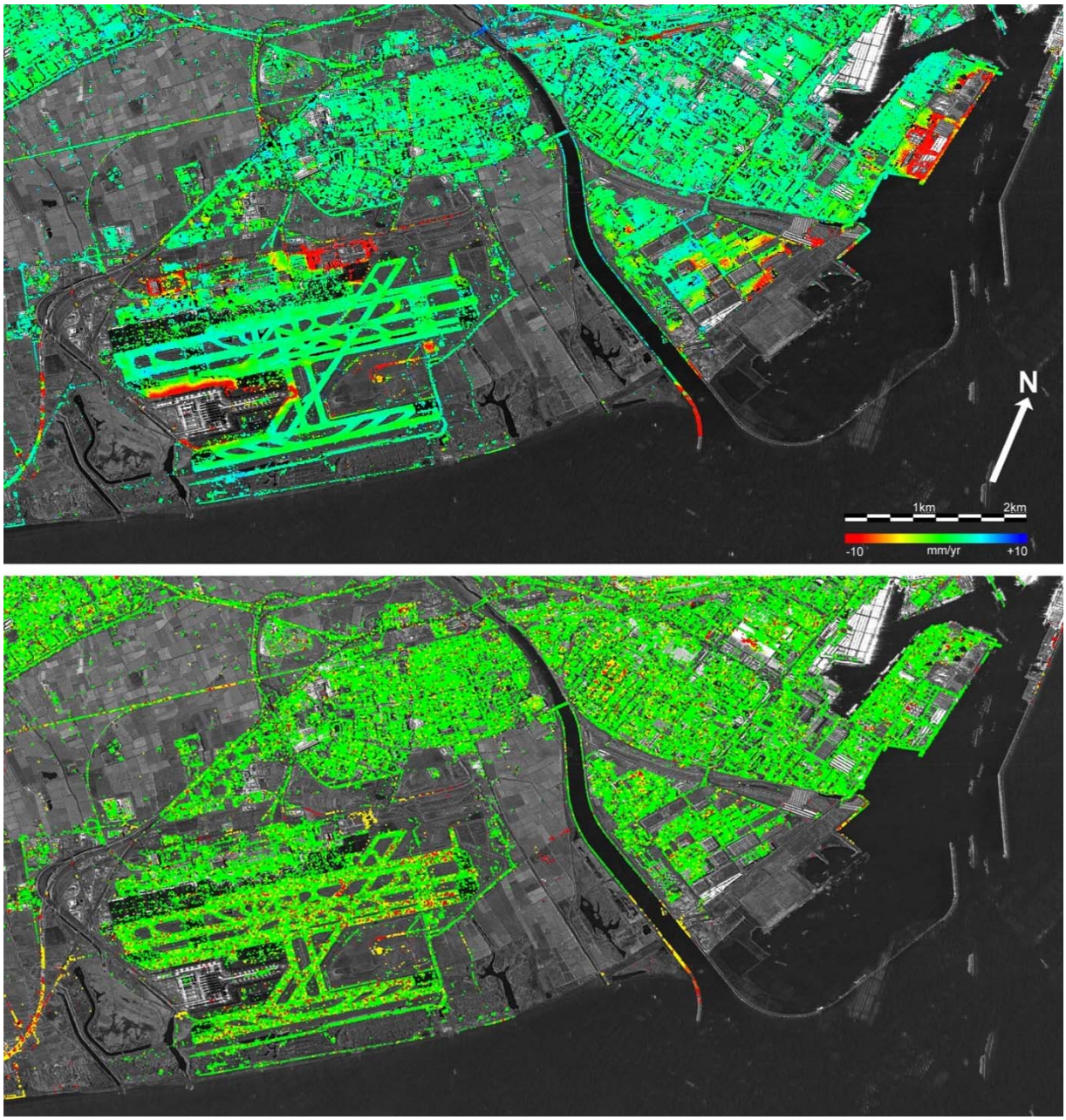

Figure 5.11. Deformation velocity map of the airport and port of Barcelona (upper image), which corresponds to the blue frame shown in Figure 5.9. Quality index map of the same area (bottom image), which displays the classes “Good” (green), “Fair” (yellow) and “Warning” (red).

It is worth comparing the proposed 2+1D phase unwrapping method with the classical LS solution, i.e. the LS solution without outlier rejection. The classical LS solution yielded the following results: all residuals are zero for 85% of the PSs, i.e. both solutions coincide; while the rest of PSs have at least one aliasing that affects the TS estimation. By contrast, this does not occur in the 2+1D phase unwrapping solution, which properly detects and corrects the unwrapping errors. This is highly important in certain areas, such as the area displayed in Figure 5.12, which shows the accumulated phase displacement (in radians) of an area of 5000 by 5000 pixels. Both solutions only coincide in the 29% of the PSs as can be seen in the accumulated phase displacement map of the classical LS solution (Figure 5.12a), and the map computed at the last iteration of the 2+1D phase unwrapping (Figure 5.12b). Both results are equivalent in most of the airport area, while the solutions differ in the rest of PSs, reaching in some cases a difference of more than 5 rad.

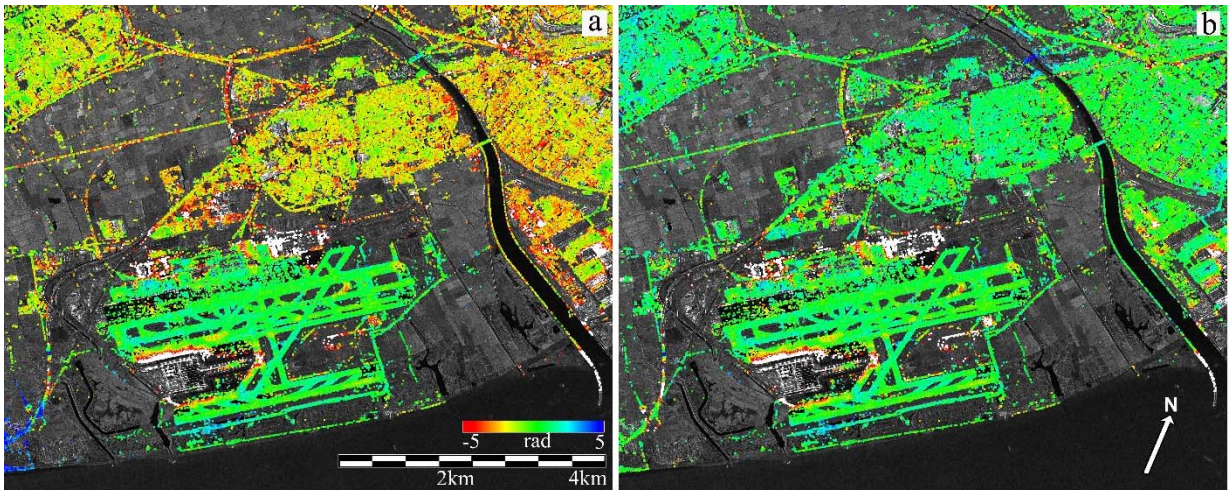

Figure 5.12. Accumulated phase displacement map of the airport using the classical LS solution (a) and map estimated at the last iteration of the 2+1D phase unwrapping procedure (b).

Figure 5.13 shows four examples of corrected TSs, where the classical LS solution is represented with triangles and the 2+1D phase unwrapping solution is displayed with circles. The number of corrected observations per image is represented by squares. The first example corresponds to a "Good" PS and the other examples are "Fair" PSs. The examples shown at the top correspond to stable PSs, while the examples at the bottom show PSs displaying displacements away from the satellite. The TSs were properly corrected in the last iteration in every case.

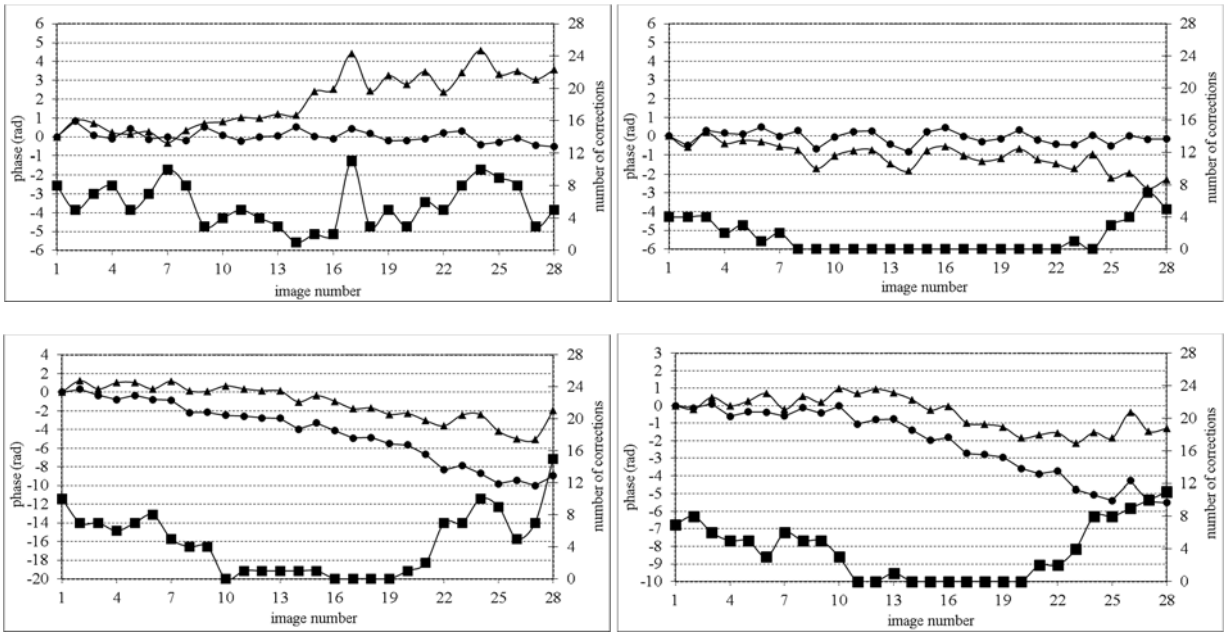

Figure 5.13. Examples of time series produced at the first iteration (triangles), last iteration (circles) and the associated corrections per image (squares). These examples were derived from a network of 28 TerraSAR-X StripMap images over the metropolitan area of Barcelona.

Chapter 6

Conclusions

The two PSI chains implemented and used at the former IG, now Geomatics Division of the CTTC, have been described and the results derived with different sensors and datasets analysed. The local area PSI chain has been described and the results derived with high-resolution X-band data have been discussed in Chapter 3. The PSIG chain has been described in Chapter 4 and a comprehensive discussion of PSIG results has been provided in Chapter 5. The conclusions are organized in two main blocks: the conclusions related to the standard PSI chain over small areas and those of the PSIG chain.

The local area PSI chain consists in a standard PSI procedure, which does not estimate the APS contribution, simplifying the procedure and making the computational process lighter. The procedure uses a linear model for the deformation in order to work with wrapped phases. The main conclusions of this block are summarized as follows:

- The chain has been successfully used with different types of spaceborne SAR data, such as ERS-1, ERS-2, ASAR, TerraSAR-X and CosmoSkyMed.
- The X-band has shown remarkable improvements with respect to C-band. In particular, it provides a denser PS sampling which allows the measurement of deformations that were not observable using the C-band. The higher quality of the phase results in an improved quality of the PSI products: RTE, velocity of deformation and time series. The X-band data have higher sensibility to subtle deformations, including those attributable the thermal effects.
- An extension of the classical two-parameter model has been proposed to account for the thermal dilation of the imaged objects.
- The extended model generates a new type of PSI product, the thermal dilation maps. These maps provide information related to the physical properties of the observed objects (i.e. the coefficient of thermal expansion) and their static structure.
- If the thermal dilation is not properly modelled, the PSI deformation products can be affected by remarkable errors, which can be particularly severe in the case of PSI datasets covering short periods.
- The estimability of the parameters of the extended model strongly depends on the number of available SAR images and the correlation between these three vectors: $[\Delta T]$, $[B_{\perp}]$ and $[\Delta Temp]$.

The PSIG chain represents a new approach to PSI data processing and analysis, whose main aim is to cover extended areas. The procedure includes a first block in which a set of correctly unwrapped and temporally ordered phases are computed over a set of evenly distributed PSs over the entire area of interest. The key element of this block is the so-called Cousin PSs (CPSs), which are PSs characterized by a moderate spatial phase variation that ensures a correct phase unwrapping. The first processing block uses flexible tools to check the consistency of phase

unwrapping and to guarantee a uniform CPS coverage. After a second block devoted to APS estimation and removal, the PS deformation velocity and time series are derived in the third block. The key tool of this last block is a 2+1D phase unwrapping procedure. The main outputs of each block have been discussed step by step. The conclusions related to the PSIG chain are listed below:

- A full new PSI chain has been implemented and tested to cover wide areas. Its performance has been illustrated with a stack of 28 TerraSAR-X images covering the metropolitan area of Barcelona.
- A new procedure to select PSs based on a phase similarity criterion that ensures a correct phase unwrapping has been proposed. This approach (i) is appropriate to cover full scenes, (ii) includes a consistency check of the phase unwrapping, and (iii) is computationally lighter than the classical two-parameter model.
- The PSIG chain includes an advanced phase unwrapping algorithm, named 2+1D phase unwrapping, which consists in a 2D phase unwrapping followed by a temporal phase unwrapping. This last step is used to detect and correct the phase unwrapping errors created in the 2D stage. This algorithm provides good results if sufficient data redundancy is available.
- The 2+1D phase unwrapping provides a set of outputs that can be used to control the quality of the results. They include: (i) the plot of residuals at the first LS iteration, which is useful to check the phase unwrapping errors, both interferogram wise and PS wise; (ii) a quality index for each PS time series; and (iii) the number of corrections per image of a time series, which provides detailed information to discriminate between reliable and problematic images within a given time series.
- The PSIG chain has been successfully tested using two datasets: a stack of 28 TerraSAR-X images over Barcelona, and a stack of 30 CosmoSkyMed images over the metropolitan area of Seattle. The TerraSAR-X dataset, where more than 30 major deformation phenomena have been found over the entire frame, has been used to illustrate the procedure step by step.

Even though good results have been achieved using the new PSIG chain, further research needs to be carried out to improve some weak points of the procedure. An improved CPS selection is needed to avoid selecting PSs affected by thermal dilation in those cases where the parameter estimability is problematic. The APS filtering algorithm requires further development, especially to obtain a robust temporal filtering that works with limited sets of SAR images. More research needs be done to increase the PS density in non-urban and peripheral areas. Finally, the chain needs to be adapted to process the forthcoming Sentinel-1 data, mainly focusing in the computational improvement of the algorithms that need to process big volumes of PSI data.

Bibliography

Adam, N., Kampes, B., Eineder, M., Worawattanamateekul, J., Kircher, M., 2003. "*The development of a scientific permanent scatterer system*". Proc. of ISPRS Workshop High Resolution Mapping from Space, Hannover (Germany).

Adam, N., Rodriguez-Gonzalez, F., Parizzi, A., Liebhart, W., 2011. "*Wide area persistent scatterer interferometry*". Proc. of International Geoscience and Remote Sensing Symposium (IGARSS), Vancouver (Canada).

Baarda, W., 1968. "*A testing procedure for use in geodetic networks*". Rijkscommissie voor Geodesie, Delft, The Netherlands.

Bamler, R., and Hartl, P., 1998. "*Synthetic aperture radar interferometry*". Inverse problems, 14(4), R1-54.

Bentley, J.L., 1975. "*Multidimensional binary search trees used for associative searching*". Communications of the ACM, 18(9), 509-517.

Berardino, P., Fornaro, G., Lanari, R., Sansosti, E., 2002. "*A new algorithm for surface deformation monitoring based on small baseline differential SAR interferograms*". IEEE Transactions on Geoscience and Remote Sensing, 40(11), 2375–2383.

De Berg, M., Cheong, O., van Kreveld, M., Overmars, M., 2008. "*Computational Geometry: Algorithms and Applications"*. Springer-Verlag.

Björck, Å., 1996. "*Numerical methods for least square problems*". Siam: Philadelphia, PA, USA.

Biescas, E., Crosetto, M., Agudo, M., Monserrat, O., Crippa, B., 2007. "*Two Radar Interferometric approaches to monitor slow and fast land deformation*". Journal of Surveying Engineering, 133(2), 66-71.

Costantini, M. 1998. "*A novel phase unwrapping method based on network programming*". IEEE Transactions on Geoscience and Remote Sensing, 36(3), 813–821.

Costantini, M., Farina, A., Zirilli, F., 1999. "*A fast phase unwrapping algorithm for SAR interferometry*". IEEE Transactions on Geoscience and Remote Sensing, 37(1), 452– 460.

Costantini, M., Malvarosa, F., Minati, F., Pietranera, L., Milillo, G., 2002. "*A three-dimensional phase unwrapping algorithm for processing of multitemporal SAR interferometric measurements"*. Proc. of International Geoscience and Remote Sensing Symposium (IGARSS), Toronto (Canada).

Costantini, M., Falco, S., Malvarosa, F., Minati, F., 2008. "*A New Method for Identification and Analysis of Persistent Scatterers in Series of SAR Images*". Proc. of International Geoscience and Remote Sensing Symposium (IGARSS), Boston (USA).

Costantini, M., Malvarosa, F., Minati, F., Vecchioli, F., 2012. "*Multi-scale and block decomposition methods for finite difference integration and phase unwrapping of very large datasets in high resolution SAR interferometry*". Proc. of International Geoscience and Remote Sensing Symposium (IGARSS), Munich (Germany).

Crosetto, M., Crippa, B., Biescas, E., 2005. "*Early detection and in-depth analysis of deformation phenomena by radar interferometry*". Engineering Geology, 79(1), 81–91.

Crosetto, M., Biescas, E., Duro, J., Closa, J., Arnaud, A., 2008. "*Generation of Advanced ERS and Envisat Interferometric SAR Products Using the Stable Point Network Technique*". Photogrammetric Engineering and Remote Sensing, 74(4), 443–450.

Crosetto, M., Monserrat, O., Iglesias, R., Crippa, B., 2010. "*Persistent scatterer interferometry: Potential, limits and initial C- and X-band comparison*". Photogrammetric Engineering and Remote Sensing, 76(9), 1061–1069.

Crosetto, M., Monserrat, O., Cuevas, M., Crippa, B., 2011. "*Spaceborne Differential SAR Interferometry: Data Analysis Tools for Deformation Measurement*". Remote Sensing, 3(2), 305-318.

Crosetto, M., Monserrat, O., Cuevas-González, M., Devanthéry, N., Luzi, G., Crippa, B., 2014. "*Measuring thermal expansion using X-band persistent scatterer interferometry*". ISPRS Journal of Photogrammetry and Remote Sensing (accepted for publication).

Cuevas, M., Monserrat, O., Crosetto, M., Crippa, B., 2011. "*A new product from persistent scatterer interferometry: the thermal dilation maps*". Proc. of Joint Urban Remote Sensing Event, Munich (Germany).

Curlander, J., and McDonough, R., 1991. "*Synthetic aperture radar: systems and signal processing"*. John Wiley & Sons, Inc, New York.

Devanthéry, N., Crosetto, M., Monserrat, O., Cuevas-González, M., Crippa, B., 2014. *An Approach to Persistent Scatterer Interferometry*. Remote Sensing, 6(7), 6662-6679.

Duro, J., Mora, O., Agudo, M., Arnaud, A., 2010. "*First results of Stable Point Network software using TerraSAR-X data*". Proc. of EUSAR, Aachen (Germany).

Elachi, C., 1988. "*Spaceborne radar remote sensing: Applications and techniques*". Institute of Electrical and Electronics Engineers, New York.

Ferretti, A., Prati, C., Rocca, F., 1999. "*Permanent scatterers in SAR interferometry*". Proc. of Remote Sensing, International Society for Optics and Photonics, Florence (Italy).

Ferretti, A., Prati, C., Rocca, F., 2000. "*Nonlinear subsidence rate estimation using permanent scatterers in differential SAR interferometry*". IEEE Transactions on Geoscience and Remote Sensing, 38(5), 2202-2212.

Ferretti, A., Prati, C., Rocca, F., 2001. "*Permanent scatterers in SAR interferometry*". IEEE Transactions on Geoscience and Remote Sensing, 39(1), 8-20.

Ferretti, A., Perissin, D., Prati, C., Rocca, F., 2005. "*On the physical nature of SAR permanent scatterers*". Proc. of URSI Commission Symposium Microwave Remote Sensing Earth, Oceans, Ice, Atmosphere, Ispra (Italy).

Ferretti, A., Fumagalli, A., Novali, F., Prati, C., Rocca, F., Rucci, A., 2011. "*A new algorithm for processing interferometric data-stacks: SqueeSAR*". IEEE Transactions on Geoscience and Remote Sensing, 49(9), 3460-3470.

Fornaro, G., Franceschetti, G., Lanari, R., 1996. "*Interferometric SAR phase unwrapping using Green's formulation*". IEEE Transactions on Geoscience and Remote Sensing, 34(3), 720-727.

Fornaro, G., Serafino, F., Reale, D., 2009. "*4D SAR imaging for height estimation and monitoring of single and double scatterers*". IEEE Transactions on Geoscience and Remote Sensing, 47(1), 224-237.

Fornaro, G., Pauciullo, A., Reale, D., 2011. "*A null-space method for the phase unwrapping of multitemporal SAR interferometric stacks*". IEEE Transactions on Geoscience and Remote Sensing, 49(6), 2323-2334.

Fornaro, G., Reale, D., Verde, S., 2013. "*Bridge thermal dilation monitoring with millimeter sensitivity via multidimensional SAR imaging*". IEEE Geoscience and Remote Sensing Letters, 10(4), 677–681.

Förstner, W., 1986. "*Reliability, gross error detection and self-calibration*". ISPRS Commission III Tutorial on Statistical Concepts for Quality Control, International Archives of Photogrammetry and Remote Sensing, 26(3/4), 1-34.

Gabriel A.K., Goldstein, R.M., Zebker, H.A., 1989. "*Mapping small elevation changes over large areas: differential radar interferometry*". Journal of Geophysical Research, 94(B7), 9183-9191.

Gernhardt, S., Adam, N., Eineder, M., Bamler, R., 2010. "*Potential of very high resolution SAR for persistent scatterer interferometry in urban areas*". Annals of GIS, 16(2), 103–111.

Ghiglia, D., and Romero, L., 1994. "*Robust two-dimensional weighted and unweighted phase unwrapping that uses fast transforms and iterative methods*". Journal of the Optical Society of America A, 11(1), 107–117.

Ghiglia, D., and Pritt, M., 1998. "*Two-dimensional phase unwrapping: theory, algorithms, and software*". John Wiley & Sons, Inc, New York.

Goldstein, R.M., Zebker, H.A., Werner, C., 1988. "*Satellite radar interferometry: Two-dimensional phase unwrapping*". Radio Science, 23(4), 713-720.

Hanssen, R.F., 1998. "*Atmospheric heterogeneities in ERS tandem SAR interferometry*". The Netherlands: Delft University Press.

Hanssen, R.F., 2001. "*Radar interferometry: data interpretation and error analysis*". Kluwer Academic Publishers, Dordrecht, The Netherlands.

Hooper, A., Zebker, H.A., Segall, P., Kampes, B.M., 2004. "*A new method for measuring deformation on volcanoes and other natural terrains using InSAR persistent scatterers*". Geophysical Research Letters, 31(23), doi: 10.1029/2004GL021737.

Hooper, A., Segall, P., Zebker, H.A., 2007. "*Persistent scatterer interferometric synthetic aperture radar for crustal deformation analysis, with application to Volcán Alcedo, Galápagos*". Journal of Geophysical Research: Solid Earth (1978–2012), 112(B7), doi: 10.1029/2006JB004763.

Hooper, A., and Zebker, H.A., 2007. "*Phase unwrapping in three dimensions with application to InSAR time series*". Journal of the Optical Society of America A, 24(9), 2737-2747.

Hooper, A., 2008. "*A multi-temporal InSAR method incorporating both persistent scatterer and small baseline approaches*". Geophysical Research Letters, 35(16), doi: 10.1029/2008GL034654.

Kampes, B.M., and Hanssen, R.F., 2004. "*Ambiguity resolution for permanent scatterer interferometry*". IEEE Transactions on Geoscience and Remote Sensing, 42(11), 2446–2453.

Kampes, B.M., 2006. "*Radar interferometry: persistent scatterer technique*". Springer, Dordrecht, The Netherlands.

Lanari, R., Mora, O., Manunta, M., Mallorqui, J.J., Berardino, P., Sansosti, E., 2004. "*A small-baseline approach for investigating deformations on full-resolution differential SAR interferograms*". IEEE Transactions on Geoscience and Remote Sensing, 42(7), 1377-1386.

Van Leijen, F.J., and Hanssen, R.F., 2007. "*Persistent scatterer density improvement using adaptive deformation models*". Proc. of International Geoscience and Remote Sensing Symposium (IGARSS), Barcelona (Spain).

Van Leijen, F.J., 2014. "*Persistent scatterer interferometry based on geodetic estimation theory*". PhD thesis, Delft University of Technology.

Liebhart, W., Adam, N., Parizzi, A., 2010. "*Least squares estimation of PSI networks for large scenes with multithreaded singular value decomposition*". Proc. of EUSAR, Aachen (Germany).

Liebhart, W., Bricic, R., Parizzi, A., Rodriguez-Gonzalez, F., Adam, N., 2012. "*Persistent Scatter Interferometry Wide Area Product Methodology and Final Characteristics*". Remote Sensing Technology Institute, DLR, Oberpfaffenhofen, Germany.

Lombardini, F., 2005. "*Differential tomography: A new framework for SAR interferometry*". IEEE Transactions on Geoscience and Remote Sensing, 43(1), 37-44.

Lundgren, P., Usai, S., Sansosti, E., Lanari, R., Tesauro, M., Fornaro, G., Berardino, P., 2001. "*Modeling surface deformation observed with synthetic aperture radar interferometry at Campi Flegrei caldera"*. Journal of Geophysical Research: Solid Earth (1978–2012), 106(B9), 19355-19366.

Massonnet, D., Rossi, M., Carmona, C., Adragna, F., Peltzer, G., Feigl, K., Rabaute, T., 1993. "*The displacement field of the Landers earthquake mapped by radar interferometry*". Nature, 364(6433), 138-142.

Massonnet, D., Briole, P., Arnaud, A., 1995. "*Deflation of Mount Etna monitored by spaceborne radar interferometry*". Nature, 375(6532), 567-570.

Monserrat, O., Crosetto, M., Cuevas M., Crippa B., 2011. "*The thermal expansion component of Persistent Scatterer Interferometry observations"*. IEEE Geoscience and Remote Sensing Letters, 8, 864-868.

Mora, O., Mallorquí, J.J., Broquetas, A., 2003. "*Linear and nonlinear terrain deformation maps from a reduced set of interferometric SAR images*". IEEE Transactions on Geoscience and Remote Sensing, 41(10), 2243-2253.

Nagler, T., Rott, H., Kamelger, A., 2002. "*Analysis of landslides in Alpine areas by means of SAR interferometry*". Proc. of International Geoscience and Remote Sensing Symposium (IGARSS), Toronto (Canada).

Navarro-Sanchez, V.D., Lopez-Sanchez, J.M., 2014. "*Spatial adaptive speckle filtering driven by temporal polarimetric statistics and its application to PSI*". IEEE Transactions on Geoscience and Remote Sensing, 52(8), 4548-4557.

Pedersen, R., Sigmundsson, F., Feigl, K.L., Árnadóttir, T., 2001. "*Coseismic interferograms of two Ms=6.6 earthquakes in the South Iceland Seismic Zone, June 2000*". Geophysical Research Letters, 28(17), 3341-3344.

Peltzer, G., and Rosen, P.A., 1995. "*Surface displacement of the 17 May 1993 Eureka valley, California, earthquake observed by SAR Interferometry*". Science, 268(5215), 1333-1336.

Pepe, A., Sansosti, E., Berardino, P., Lanari, R., 2005. "*On the generation of ERS/ENVISAT DInSAR time-series via the SBAS technique*". IEEE Geoscience and Remote Sensing Letters, 2(3), 265-269.

Pepe, A., Lanari, R., 2006. "*On the extension of the minimum cost flow algorithm for phase unwrapping of multitemporal differential SAR interferograms*". IEEE Transactions on Geoscience and Remote Sensing, 44(9), 2374-2383.

Pepe, A., Manunta, M., Mazzarella, G., Lanari, R., 2007. "*A space-time minimum cost flow phase unwrapping algorithm for the generation of persistent scatterers deformation time-series*". Proc. of International Geoscience and Remote Sensing Symposium (IGARSS), Barcelona (Spain).

Pepe, A., Berardino, P., Bonano, M., Euillades, L.D., Lanari, R., Sansosti, E., 2011. "*SBAS-based satellite orbit correction for the generation of DInSAR time-series: Application to RADARSAT-1 data*". IEEE Transactions on Geoscience and Remote Sensing, 49(12), 5150-5165.

Perissin, D., and Rocca, F., 2006. "*High-accuracy urban DEM using permanent scatterers*". IEEE Transactions on Geoscience and Remote Sensing, 44(11), 3338-3347.

Perissin, D., and Ferretti, A., 2007. "*Urban-target recognition by means of repeated spaceborne SAR images*". IEEE Transactions on Geoscience and Remote Sensing, 45(12), 4043-4058.

Reale, D., Fornaro, G., Pauciullo, A., 2013. "*Extension of 4-D SAR Imaging to the Monitoring of Thermally Dilating Scatterers*". IEEE Transactions on Geoscience and Remote Sensing, 51(12), 5296-5306.

Reilinger, R.E., Ergintav, S., Bürgmann, R., McClusky, S., Lenk, O., Barka, A, Gurkan, O., Hearn, L., Feigl, K.L., Cakmak, R., Aktug, B., Ozener, H., Töksoz, M.N., 2000. "*Coseismic and postseismic fault slip for the 17 August 1999, M= 7.5, Izmit, Turkey earthquake*". Science, 289(5484), 1519-1524.

Rodriguez Gonzalez, F., Bhutani, A., Adam, N., 2011. "*L1 network inversion for robust outlier rejection in persistent scatterer interferometry*". Proc. of International Geoscience and Remote Sensing Symposium (IGARSS), Vancouver (Canada).

Rosen, P.A., Hensley, S., Joughin, I.R., Li, F.K., Madsen, S.N., Rodriguez, E., Goldstein, R.M., 2000. "*Synthetic aperture radar interferometry*". Proceedings of the IEEE, 88(3), 333-382.

Ulaby, F.T., Moore, R.K., Fung, A.K., 1986. "Microwave Remote Sensing. Active and Passive - Volume III: From Theory to Applications". Artech House, Inc.

Usai, S., 2001. "*A New Approach for Long term Monitoring of Deformations by Differential SAR Interferometry*". PhD thesis, Delft University of Technology.

Werner, C., Wegmüller, U., Strozzi, T., Wiesmann, A., 2003. "*Interferometric point target analysis for deformation mapping*". Proc. of International Geoscience and Remote Sensing Symposium (IGARSS), Toulouse (France).

Zebker, H.A., and Villasenor, J., 1992. "*Decorrelation in interferometric radar echoes"*. IEEE Transactions on Geoscience and Remote Sensing, 30(5), 950-959.

Zebker, H.A., Rosen, P.A., Hensley, S., 1997. "*Atmospheric effects in interferometric synthetic aperture radar surface deformation and topographic maps*". Journal of Geophysical Research: Solid Earth (1978–2012), 102(B4), 7547-7563.

Appendix: examples of deformation maps

The examples of deformation maps were derived from 28 StripMap TerraSAR-X images covering the metropolitan area of Barcelona and spanning from December 2007 to November 2009.

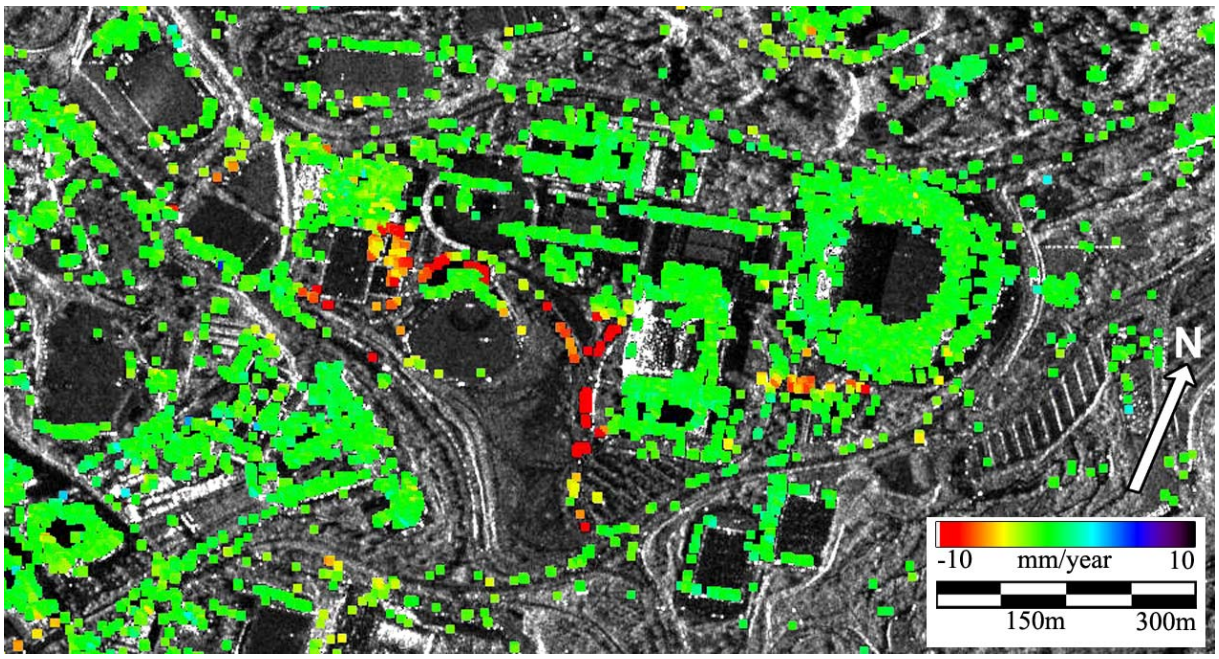

Figure A1. Deformation velocity map of the area of Montjuïc (Barcelona) displaying a subsidence of up to 10 mm/year in the LOS near the Palau Sant Jordi, over an area built on a sandstone quarry that was active in the past century. This movement is probably related to a vertical settlement caused by a continuous compaction of the underground landfill.

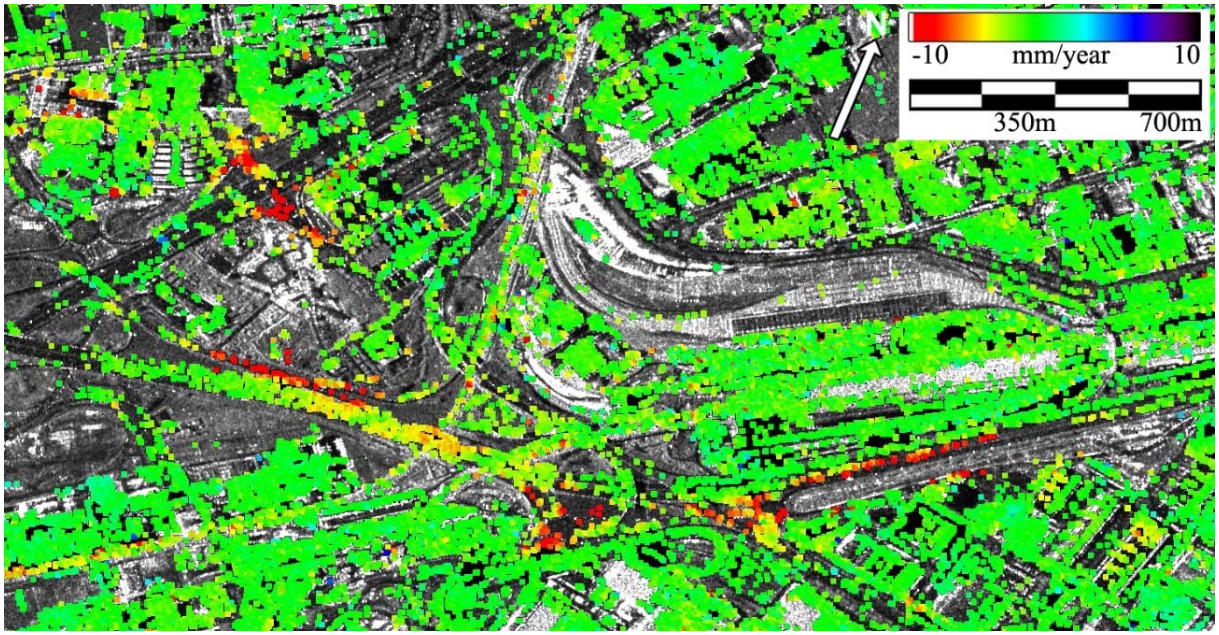

Figure A2. Deformation velocity map of an industrial park (Parc Logistic) located in the metropolitan area of Barcelona. In the left part of the figure, the map shows settlement movements of up to 10 mm/year the bridge and road. The right hand side of the figure shows a subsidence movement related to underground works of the new underground line L9.

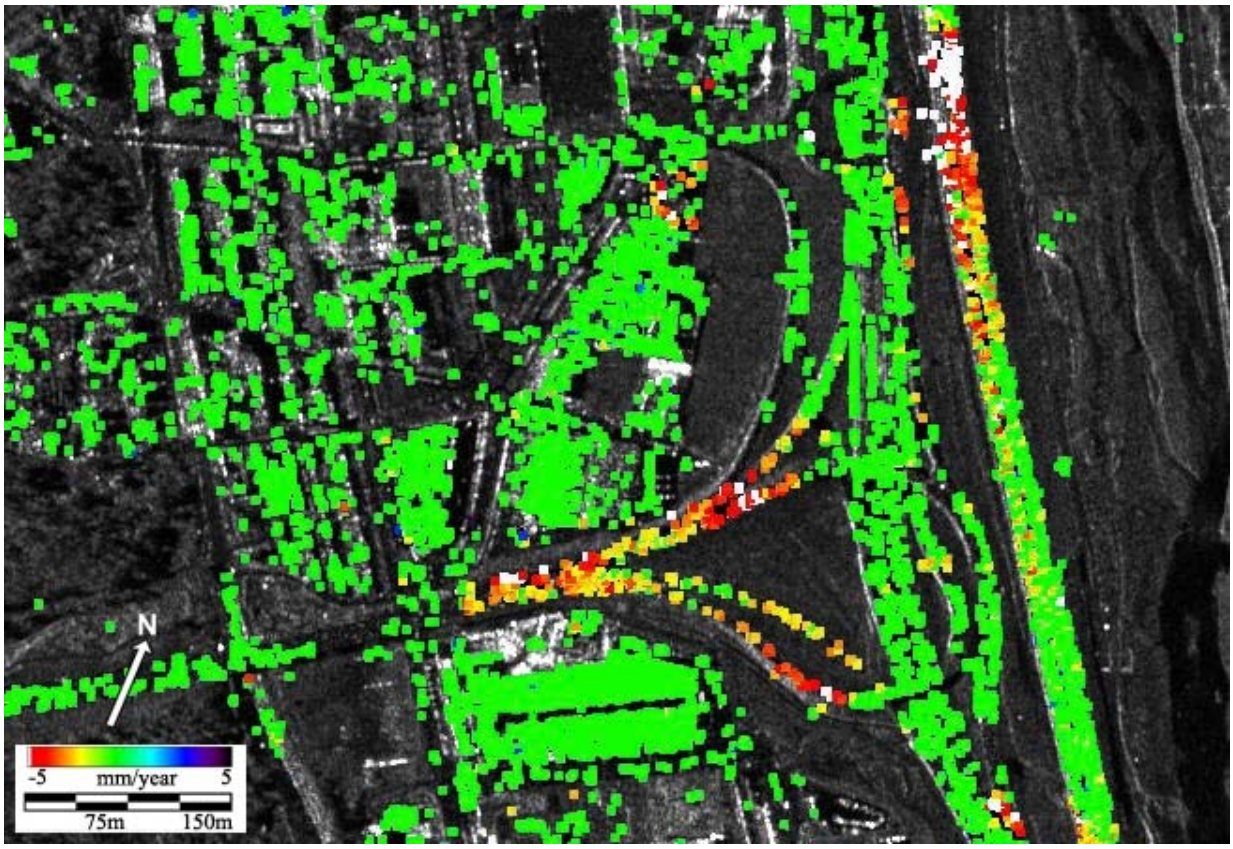

Figure A3. Deformation velocity map of an area located near Pallejà (Barcelona). The subsidence affects the access roads of a highway and a portion of the high-speed railway (AVE) embankment.

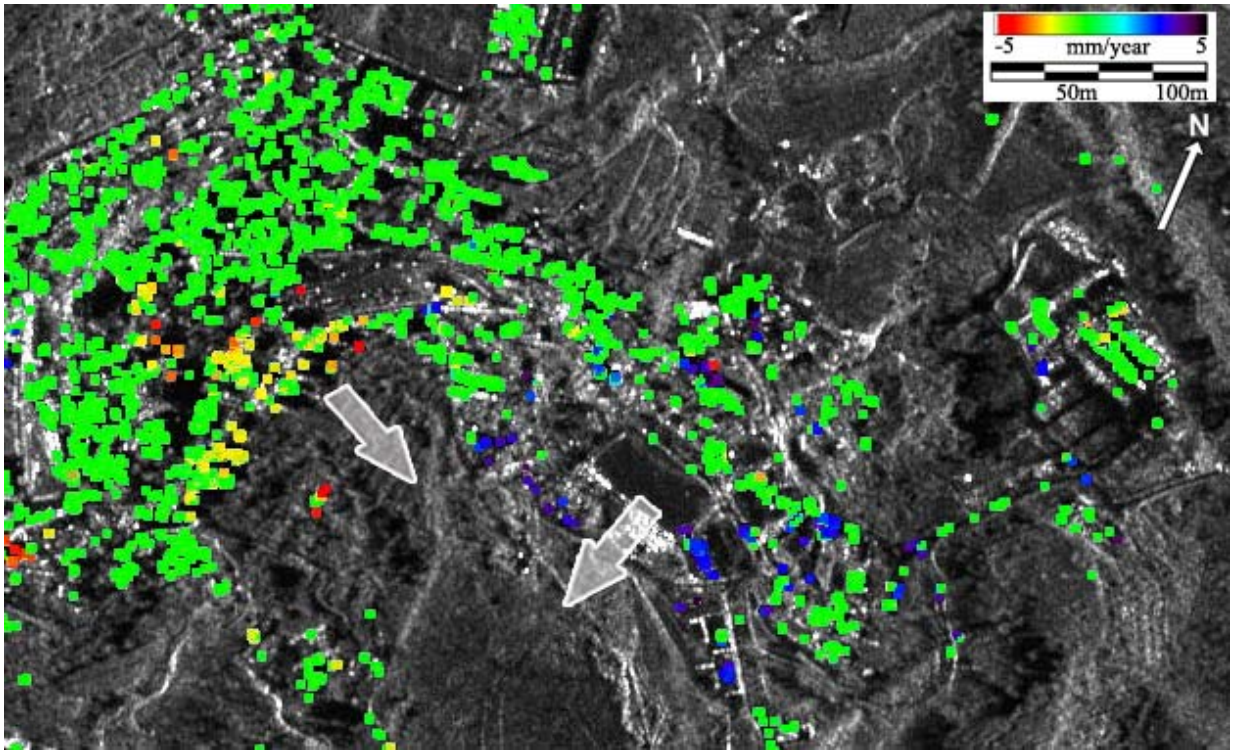

Figure A4. Deformation velocity map of El Papiol (Barcelona). Two different slopes of a landslide are observed (see white arrows). The different observation geometry causes that the displacements appear as a subsidence (yellow and reddish PSs) in one slope and as an uplift (blue to purple PSs) in the other one.

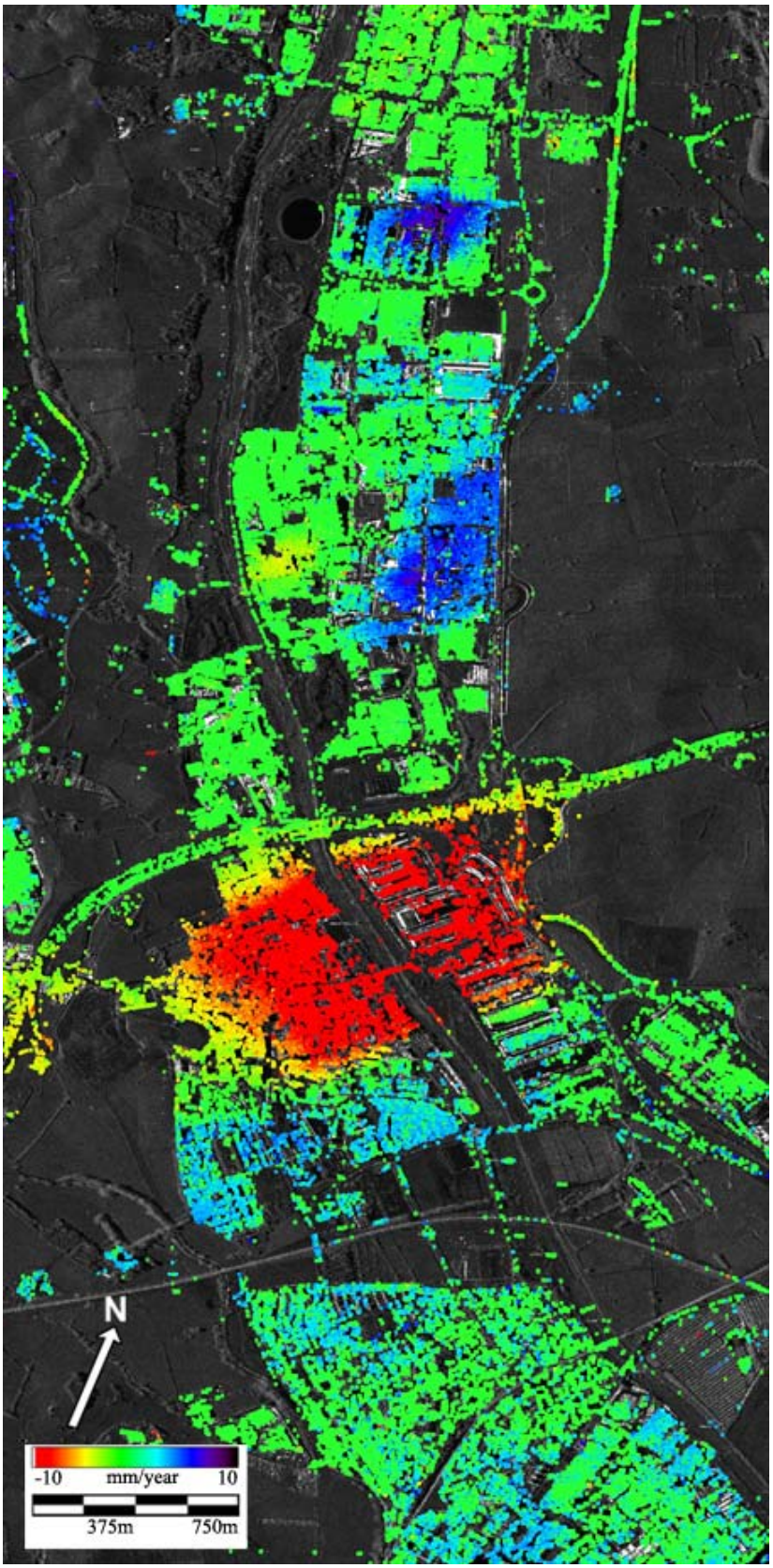

Figure A5. Deformation velocity map of Santa Perpètua de Mogoda (Barcelona). The central subsidence, with a LOS maximum of more than 10 mm/year, is probably caused by water abstraction. The two uplifts in the upper part of the figure reach 8 mm/year in the LOS and are probably caused by the cease of water pumping.

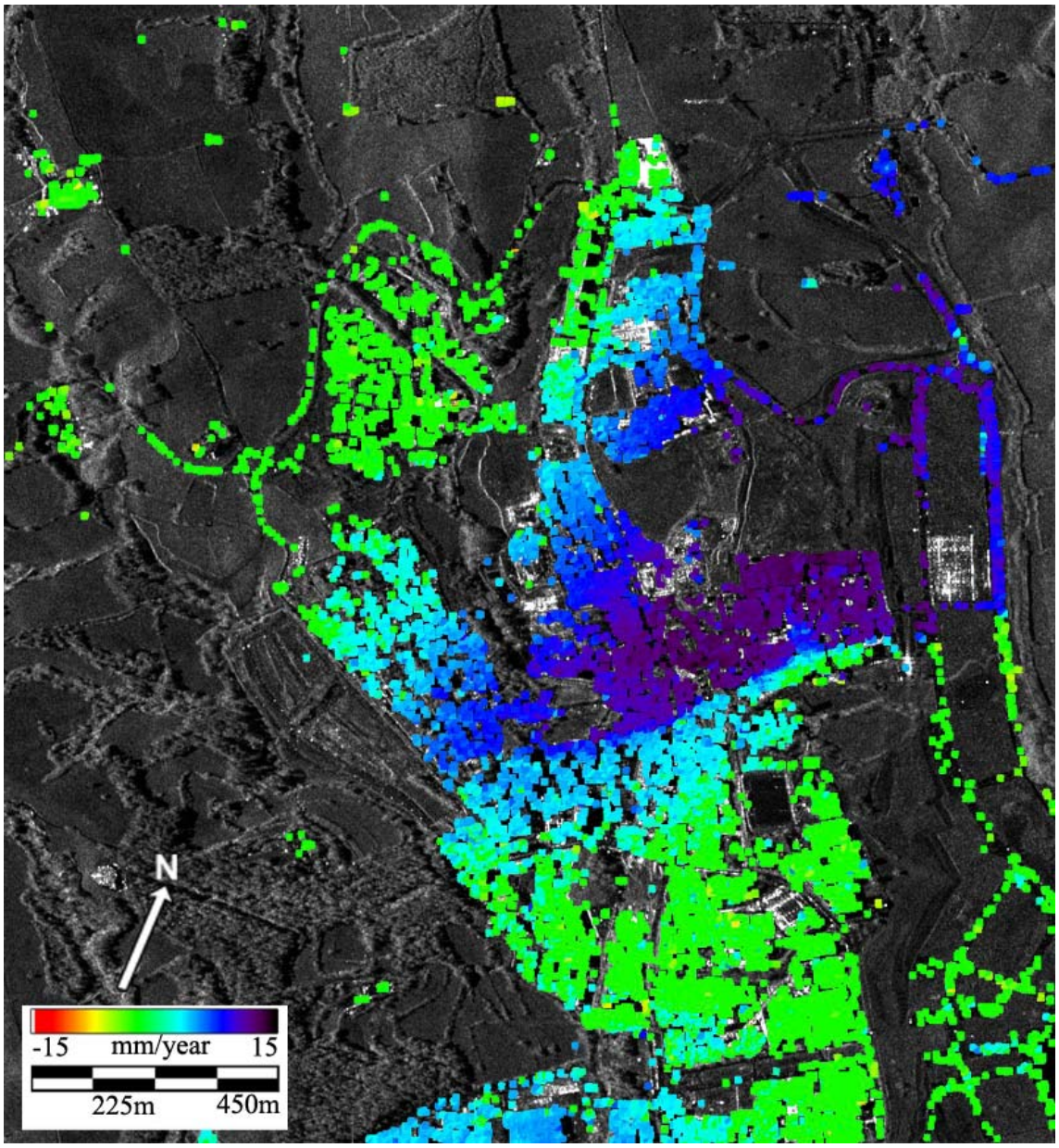

Figure A6. Deformation velocity map of an area located in Polinyà (Barcelona). The uplift, up to 15 mm/year in the LOS, is probably caused by the cease of water pumping.